A COMPARATIVE STUDY ON THE SEVERE PLASTIC DEFORMATION OF METALS BY CONSTRAINED GROOVE PRESSING

A Thesis

by

Zeynel Güler

Submitted to the
Graduate School of Sciences and Engineering
In Partial Fulfillment of the Requirements for
the Degree of

Master of Science

in the
Department of Mechanical Engineering

Özyeğin University
June 2018

A COMPARATIVE STUDY ON THE SEVERE PLASTIC DEFORMATION OF METALS BY CONSTRAINED GROOVE PRESSING

Approved by:

Assoc. Prof. Dr. Güney Güven Yapıcı,
Advisor, Department of Mechanical Engineering
Özyeğin University

Assist. Prof. Dr. Mehmet İpekoğlu
Department of Mechatronic Systems
Turkish-German University

Assist. Prof. Dr. Polat Şendur
Department of Mechanical Engineering
Özyeğin University

To My Family

For their endless love.

ABSTRACT

The main purpose of the present thesis is to reveal the microstructural refinement and mechanical behavior improvement of metallic materials, some of which are difficult to work, through severe plastic deformation. Constrained Groove Pressing is implemented in this study as a Severe Plastic Deformation method. Five different routes of Constrained Groove Pressing are planned to analyze the route effect on the materials. In this research, three different materials, namely AISI 304 stainless steel, Ti-15V-3Cr-3Sn-3Al and commercially pure zinc, are studied at room temperature. After microstructure and mechanical behavior of the samples are examined through optical microscopy, tension and erichsen tests and microhardness measurements, the underlying mechanisms are analyzed.

CGP process of AISI 304 and Ti-15V-3Cr-3Sn-3Al results in a slight grain refinement while a comparatively high refinement has been observed for commercially pure zinc. Also, CGP routes have been significantly effective for only pure zinc samples in dictating grain sizes. After deformation, mechanical twinning activation has taken place for stainless steel and pure zinc samples. Twins recorded in AISI 304 with FCC lattice structure are thinner and sharper than that of commercially pure zinc with HCP lattice structure. Strain path is not considerably effective for AISI 304 samples. For pure zinc samples, twins are thinner for the routes A, C and D, compared to the other routes after the final pass. They are also rather thick and few in number after the first pass. Moreover, intensity of twins is relatively low for route E.

It has been observed that CGP causes comparatively high strength increase in AISI 304 which has an FCC crystal structure, but lower increase in both Ti-15V-3Cr-3Sn-3Al and commercially pure zinc having BCC and HCP crystal structures, respectively. For

AISI 304, the best strength improvement is nearly 41% occuring in TD for route C. For Ti alloy, the highest strength increase is about 16%, occurring in LD for routes D and E. For pure zinc, the best strength improvement is nearly 28% in TD belonging to route D.

This study mainly aims to demonstrate the effect of several novel CGP routes on the metals having different crystal structures by analyzing the relationship between resulting microstructures and mechanical properties.

ÖZET

Bu tez çalışmasının temel amacı, aşırı plastik deformasyon yoluyla, bazılarının işlenmesi zor olan metalik malzemelerin mikro yapısal inceltimi ve mekanik davranış gelişimini ortaya koymaktır. Sınırlı Kanallı Presleme (SKP), bu çalışmada bir Aşırı Plastik Deformasyon (APD) yöntemi olarak uygulanmaktadır. Malzemeler üzerindeki rota etkisinin analiz edilmesi için beş farklı Sınırlı Kanallı Presleme rotası planlanmıştır. Bu araştırmada, AISI 304 paslanmaz çelik, Ti-15V-3Cr-3Sn-3Al ve saf çinko olmak üzere üç farklı malzeme oda sıcaklığında çalışılmıştır. Numunelerin mikro yapı ve mekanik davranışları optik mikroskopi, gerilim ve eriksen testleri ve mikro sertlik ölçümleri ile incelendikten sonra altta yatan mekanizmalar incelenmiştir.

AISI 304 ve Ti-15V-3Cr-3Sn-3Al'nin SKP prosesi, zayıf bir inceltme ile sonuçlanırken, saf çinko için nispeten yüksek bir inceltme gözlemlenmiştir. Ayrıca, SKP rotaları, tane boyutlarının belirlenmesinde sadece saf çinko numuneleri için önemli ölçüde etkili olmuştur. Deformasyondan sonra, paslanmaz çelik ve saf çinko numuneleri için mekanik ikizlenme aktivasyonu gerçekleşmiştir. YMK kafes yapısına sahip olan AISI 304'te kaydedilen ikizler, HCP kafes yapısına sahip saf çinkodan daha ince ve daha keskindir. Gerinim rotası, AISI 304 numuneleri için fazla etkili değildir. Saf çinko numuneleri için, son pasodan sonra ikizler A, C ve D rotaları için diğer rotalara kıyasla daha incedir. İlk pasodan sonra da oldukça kalın ve az sayıdadır. Ayrıca, ikizlerin yoğunluğu, rota E için nispeten düşüktür.

SKP'nin, YMK kristal yapısına sahip olan AISI 304'te nispeten yüksek mukavemet artışına neden olmasına karşın hem HMK kristal yapısına sahip olan Ti-15V-3Cr-3Sn-3Al'de hem de ASD kristal yapısına sahip olan saf çinkoda daha düşük bir artışa neden olduğu gözlenmiştir. AISI 304 için, TD'de en iyi mukavemet iyileştirmesi % 41'dir. Ti alaşımı için, en yüksek mukavemet artışı, D ve E rotaları için LD'de meydana gelmiştir

ve yaklaşık %16'dır. Saf çinko için, en iyi mukavemet iyileştirmesi D rotasına ait TD'de yaklaşık %28'dir.

Bu çalışmanın amacı, birçok yeni SKP rotasının, ortaya çıkan mikroyapılar ve mekanik özellikler arasındaki ilişkiyi analiz ederek farklı kristal yapılarına sahip metaller üzerindeki etkisini ortaya koymaktır.

ACKNOWLEDGEMENTS

Praise be to Allah, who gave me the strength along with a great supervisor, helpful professors, valuable colleagues, and a lovely family that were all necessary to complete this thesis.

First of all, I would like to sincerely thank my supervisor, Dr. Güney Güven Yapıcı, for supporting me through his guidance and feedback. He was the one who was willing to take me on as a master's student in the first place. Had he not believed in me and agreed to accept me, my journey might have stopped right there and then. His belief in my capabilites has provided me with the opportunity to complete this thesis, and pursue my doctoral studies at a prominent university of the United States, which was my long-held dream. Besides, I would like to mention that our road trips to the university has contributed to me abundantly in terms of both academic and life experience.

Secondly, my thesis committee members, Assist. Prof. Dr. Mehmet İpekoğlu and Assist. Prof. Dr. Polat Şendur are specially thanked for their guidance and attention to this study.

Further, many thanks go to Mr. Ulaş Yıldırım, and my colleagues in the MEMFIS group, Seyyedvahid Sajjadifar, Salar Salahi, Ali Hosseinzadeh Ghobadlou, Görkem M. Şimşek and Onur Bilgin, who never denied their help. Special thanks go to my best friends, Hüseyin Atahan İnan, Enver Kapan, Ali Enes Öztürk along with my hackerspace workshop friends, Mahmut Demir, Alp Burak Pehlivan, and Çağlayan Şerbetçi, who have inspired me to continue my postgraduate studies.

I highly appreciate my father, Naci Güler, to whom I owe my great imagination, and my mother, Zeynep Güler, to whom I owe my working discipline, and deeply thank my dear brother, Seyda Güler for his support and kindness.

Last but not least, is the continuous support and courage received from my wife, Gülay Güler, who shared this huge burden with me. I would also like to acknowledge her as the second reader of this thesis. I should also mention my two-and-a-half-year-old sweetie son, Ali Güler, who has been my source of mirth throughout this work.

TABLE OF CONTENTS

LIST OF TABLES

LIST OF FIGURES

CHAPTER I

INTRODUCTION

1.1. Background

Enhancing mechanical properties of metals and alloys is essential as they are widely utilized in industries ranging from automobile to aerospace [1]. One way to produce materials with superior mechanical properties is reducing their average grain size to ultra-fine grain (UFG) range. UFG materials can be synthesized by two ways, viz., bottom-up approach and top-down approach. The nano-structure is produced through atom-by-atom and layer-by-layer arrangements in the bottom-up approach, which is unsuitable for industrial manufacturing since porous structure is often observed in this approach [2-4]. Among the methods of the top-down approach, which is free from this disadvantage, Severe Plastic Deformation (SPD) is an efficient way [5-7].

The principle of SPD methods entails increasing dislocation density by heavy uniform deformation, forming intense dislocation walls, and obtaining ultra fine or nano-scale microstructure [8]. The advantages of materials produced by SPD are superior properties like high strength and hardness, non-porous structure and proper dimensions for mechanical and physical testing [9, 10]. However, these materials have limited ductility [11, 12].

Grain size of materials is generally decreased to nano-scale after the SPD processes, thus X-ray diffraction (XRD) and transmission electron microscopy (TEM) are utilized for microstructural evaluation [13]. However, grain size after proccessing of some materials is in the micro-scale [14, 15]. Therefore, optical microscopy can be sufficient in these kind of cases.

The basic principles underlying SPD techniques go back to the work by P.W. Bridgeman at Harvard University in the 1930s. This study examined the effects of combining large hydrostatic pressures with concurrent shear deformation on solids leading the researcher to receive the Nobel Prize in Physics in 1946 [16]. First successful implementations of these principles were introduced in 1980s [17, 18]. Since then, many SPD methods, e.g., equal-channel angular pressing (ECAP) [19-23], high pressure torsion (HPT) [24-30], severe torsional straining (STS) [31-34], accumulated roll-bonding (ARB) [35-40], multi-directional forging (MDF) [41, 42], cyclic extrusion compression (CEC) [43-46], repetitive corrugation and straightening (RCS) [47-50], twist extrusion (TE) [51-53], constrained groove rolling (CGR) [54], constrained groove pressing (CGP) [55] and so on, have been developed. Among them, CGR, RCS, ARB, CGP are utilized to process sheet metals. Of these, CGP is one of the most convenient methods for fabricating plate shaped materials with attractive properties.

1.2. Principles of Constrained Groove Pressing

1.2.1. CGP Process

The CGP technique was initially introduced by Shin et al. [55]. The deformation principle of CGP method can be seen in Figure 1.2.1.1(a), which shows the top view of the sample sheet pressed between a pair of grooved dies and a pair of flat dies alternately. Large amounts of strain can be accumulated in the sheet metals without changing their dimensions via this method.

The groove angle (θ) of the die is mostly designed as 45°. If a full stroke pressing is implemented for the sample, it yields a shear strain of 1 in the deformed region. This is equivalent to an effective strain of 0.58. After the sample is corrugated, it is straightened by means of flat dies. This operation causes a reverse shear deformation for the already

deformed region while the undeformed region remains unaffected. The effective strain of the deformed region after this flattening gets the value of 1.16 (the darkest blue areas in Figure 1.2.1.1). Afterwards, the sample is rotated 180° about the axis perpendicular to plane of the sample allowing the deformation of the undeformed area because of asymmetry of the grooved die (can be seen in Figure 1.2.1.1(b)). The same corrugating and flattening processes are applied for the undeformed region resulting in a homogeneous effective strain of 1.16 throughout the sample. These four pressings are called one pass [56].

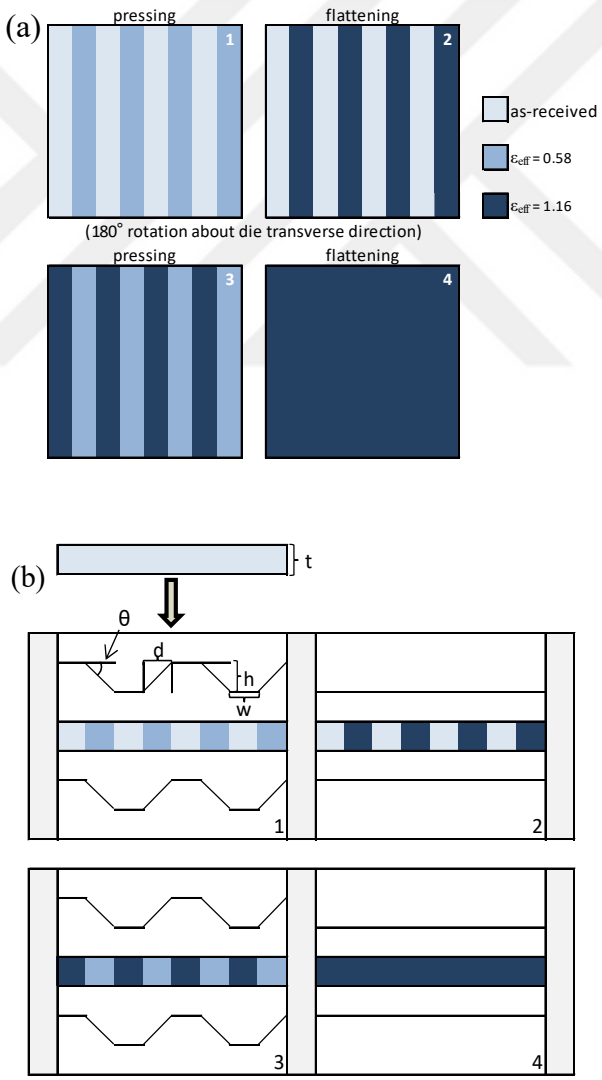

Figure 1.2.1.1: Schematic representation of a single pass of a CGP Route: (a) top view of the sample and the accumulated strain amounts; (b) side view and the parameters of the process

Accumulated strain amounts on the indicated regions of the sample after each pressings and some basic parameters are simply depicted in Figure 1.2.1.1. CGP process can be altered by changing the parameters such as groove angle (θ), thickness of the sheet (t) and groove depth (h) (Figure 1.2.1.1(b)). Pass number and route of the passes can also be changed in order to see the effect of accumulated strain and different routes.

From the many possibilities, two basic routes which are shown schematically in Figure 1.2.1.2 are utilized in the literature. Route A is the conventional route, while route B is called as the cross route [61]. Pass numbers can be different according to the study.

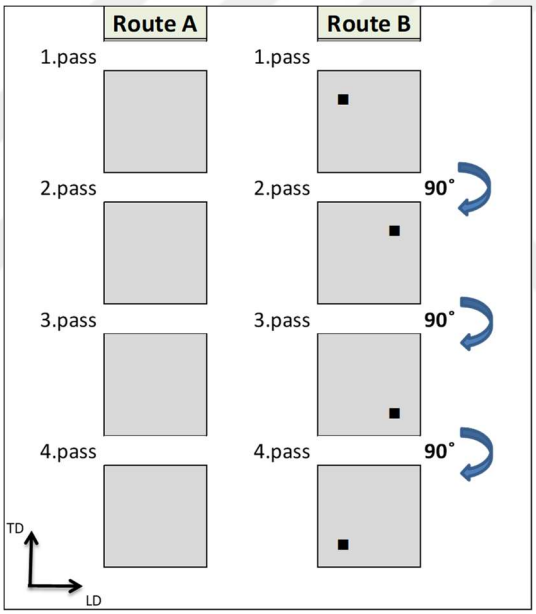

Figure 1.2.1.2: Description of general CGP Routes

The normal direction, transverse direction and the longitudinal direction is as indicated in Figure 1.2.1.3. Considering the normal direction as the normal direction of the sample, the longitudinal direction is defined to be perpendicular to the edges of the grooves, and the transverse direction to be parallel to the grooves.

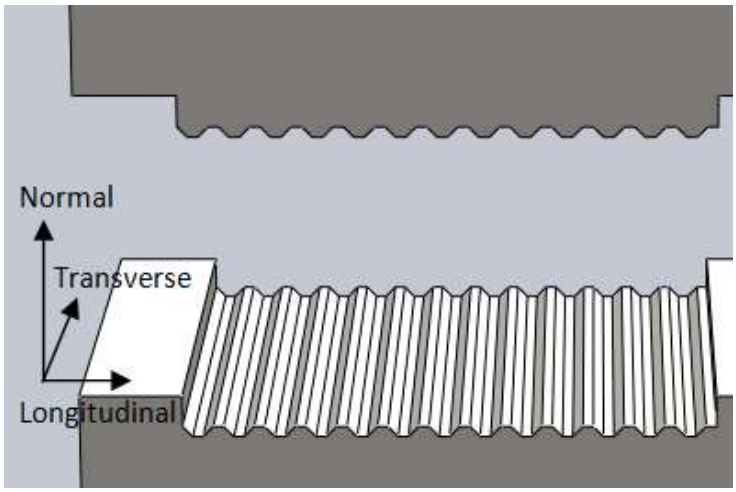

Figure 1.2.1.3: Definition of the directions on the die

1.2.2. Definition of Strain Imposed and Various Die Structures

In the previous section, it is stated that a pass of CGP induces an effective strain (ε_{eff}) of 1.16 throughout the sample. The ε_{eff} is calculated in this section.

Initially, the geometric parameters of the die and the sheet specimen are specified as given in Figure 1.2.1.1.(b).

Thickness of the sample = t

Groove angle = θ

Groove width = w

Groove height = h

Interface distance between the grooves = d

The sample is subjected to orthogonal shear deformation when pressed between the grooved dies [57]. The schematic of shear straining of the sample can be seen in Figure 1.2.2.1. Dies with groove angle of 45° are utilized for most of the studies. For these dies, if a full-stroke pressing is conducted, shear angle (γ) will be equal to 45°, which causes an engineering shear strain, γ=1 (see Eq. (1)).

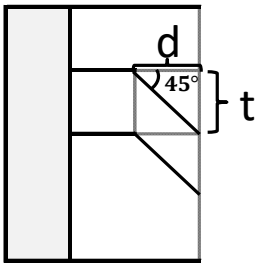

Figure 1.2.2.1: Schematic of shear straining of the sample

$$\gamma_{xy} = \frac{t}{d} = \tan 45° = 1 \quad (1)$$

The effective strain, which is simply the total true strain minus the recoverable strain, for this engineering shear strain value is 0.58, as shown in Eqs. (2) and (3) [57].

$$\varepsilon_{eff} = \sqrt{\frac{2}{9}\left[(\varepsilon_x - \varepsilon_y)^2 + (\varepsilon_y - \varepsilon_z)^2 + (\varepsilon_z - \varepsilon_x)^2\right] + \frac{4}{3}\left[\varepsilon^2{}_{xy} + \varepsilon^2{}_{yz} + \varepsilon^2{}_{zx}\right]} \quad (2)$$

In this formula $\varepsilon_{xy} = \gamma_{xy}/2$ and assuming the deformation as simple shear with no transverse and longitudinal expansion [58] (i.e., $\varepsilon_x = \varepsilon_y = \varepsilon_z = \varepsilon_{yz} = \varepsilon_{zx} = 0$), Eq. (2) would be as follows for an angle of 45°:

$$\varepsilon_{eff} = \sqrt{\frac{1}{3}} = 0.577 \approx 0.58 \quad (3)$$

However, shear angle can vary due to the groove angle, the amount of stroke or springback. Therefore, the following equation can be used as a general expression for any angle [59]:

$$\varepsilon_{eff} = \frac{\tan\theta}{\sqrt{3}} \quad (4)$$

According to this formula, the total effective strain accumulated in a sheet specimen pressed by n passes is presented as [59]:

$$\varepsilon_{total} = n\frac{2\tan}{\sqrt{3}} \quad (5)$$

If the shear angle of the material after one press is 20°, for example, the imposed strain on the inclined region of this material will be around 0.21 due to Eq.(4). If four CGP passes are applied to this material, the total accumulated effective strain on it becomes 1.68 according to Eq.(5).

Shear angle formed on the sample may be different from the die angle because of the the factors such as amount of stroke, and springback rate of the material. Finite element simulations of the influence of half die stroke is depicted for commercially pure Ni sheet in Figure 1.2.2.2 [59]. The effective strain amounts of this pressing for one pass are lower than those of the full stroke pressing. However, there are some adventages of altering the stroke. As the imposed strain would be lower after one pass, the number of passes can be increased to reach a significant strain value without cracking. Thus, the maximum strain amount that can be accumulated to a material without failure can be determined much more sensitively. Moreover, severe plastic deformation of difficult-to-work metals can be successfully accomplished without increasing the temperature. Also, the surface of the material would be smoother since the traces of the groove edges on the material become less noticeable. Springback of the sample also diminishes the expected strain amount. For example, on condition that the groove angle is 45°, and the inclined regions of the material have an angle of 40° due to the springback effect after one pressing, only the value of 40° is taken into consideration for strain calculations.

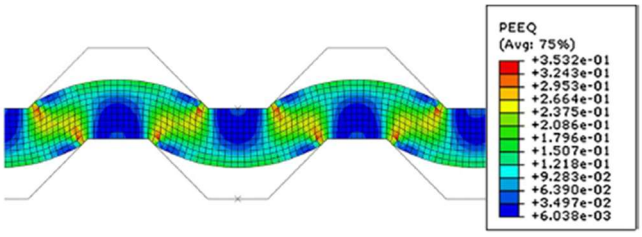

Figure 1.2.2.2: Effect of half die stroke on effective strain [59]

The parameters of the die such as groove width or groove angle can be altered for the CGP process. Numerical analysis results of one CGP pressing of a sample are seen in Figure 1.2.2.3 for different groove widths [59]. The effect of the groove width-to-sample thickness ratio on the amount and distribution of the effective strain seems to be quite different. For the small values of this ratio, the effective strain on the inclined region is higher and more regularly distributed.

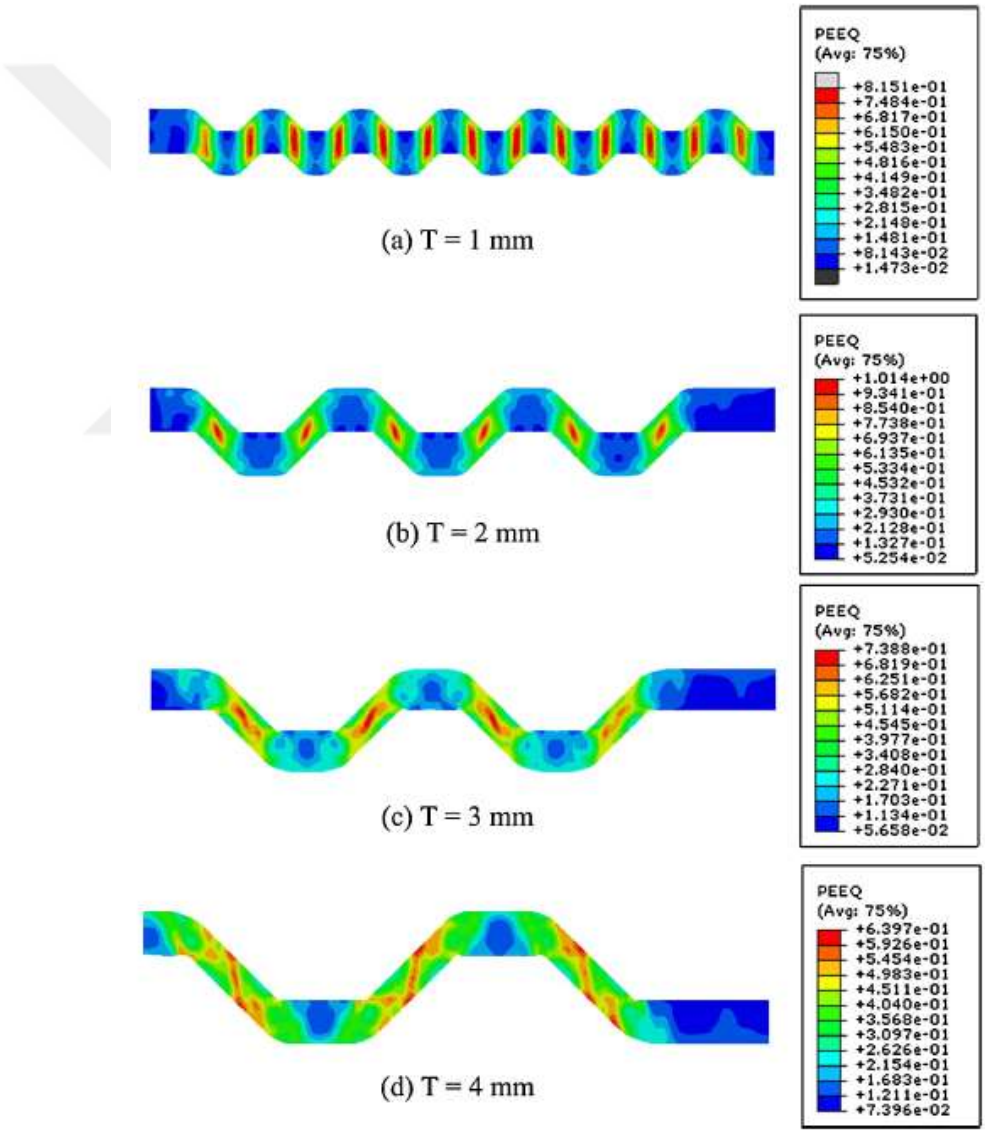

Figure 1.2.2.3: Effective strain distributions of first groove pressed samples for different groove widths [59].

Groove angle can also be changed for the CGP operation. Figure 1.2.2.4 shows the effects of different groove angles on effective strain while the groove widths are the same [59]. In this case, the effective strain amount and distribution on the same sample change again with the alteration of the groove angle.

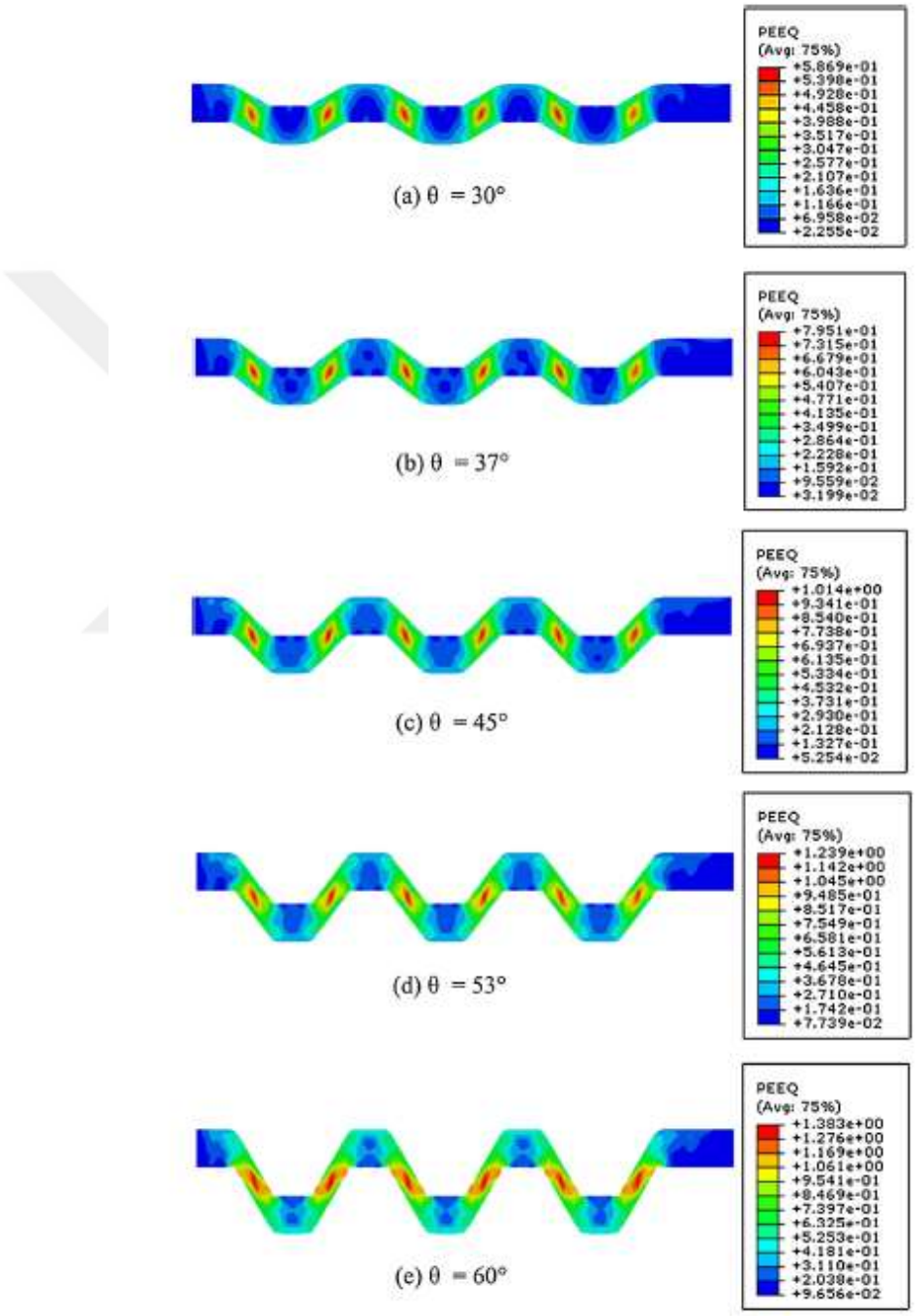

Figure 1.2.2.4: Effective strain distributions of first groove pressed samples for different groove angles [59]

1.2.3. Stress-Strain State Analysis of CGPed sample

The strain and deformation modes in the sample are not totally uniform. The deformed region has pure shear, while bending and streching take place at the corners (Figure 1.2.3.2). These different regions can produce different grain sizes, thus, different properties [60].

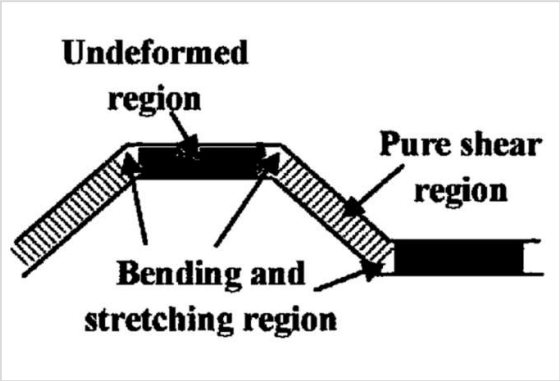

Figure 1.2.3.1: Regions of different deformation modes in the workpiece [60]

The dimensions of these regions may be different when the pressing is not full stroke. Bending and stretching regions may be broader in this case resulting in a higher nonuniformity, but the surface quality might be better because of the smoother edges.

Another subdivision is proposed based on the stress-strain state. Treating the deformation of interface location as the bending operation of wide sample, each half of a groove cycle is segmented into Regions I, II and III. The cubic stress and plane strain (ε_2=0) states on the regions of the grooved sample are described in Figure 1.2.3.2 [14].

During CGP, the outer region of the sample is in tension, and the inner region is in compression. In Region I, a tensile tangential stress (σ_1) is observed as the maximum principle stress, and a tensile tangential strain (ε_1) as the maximum principle strain. On the contrary, a compressive σ_1 and a compressive ε_1 is seen in Region II. Pure shear deformation occurs for Region III under plane strain condition. For the flattening process,

Region I replaces Region II, and vice versa. Region III is subjected to reverse shear deformation in this case [14].

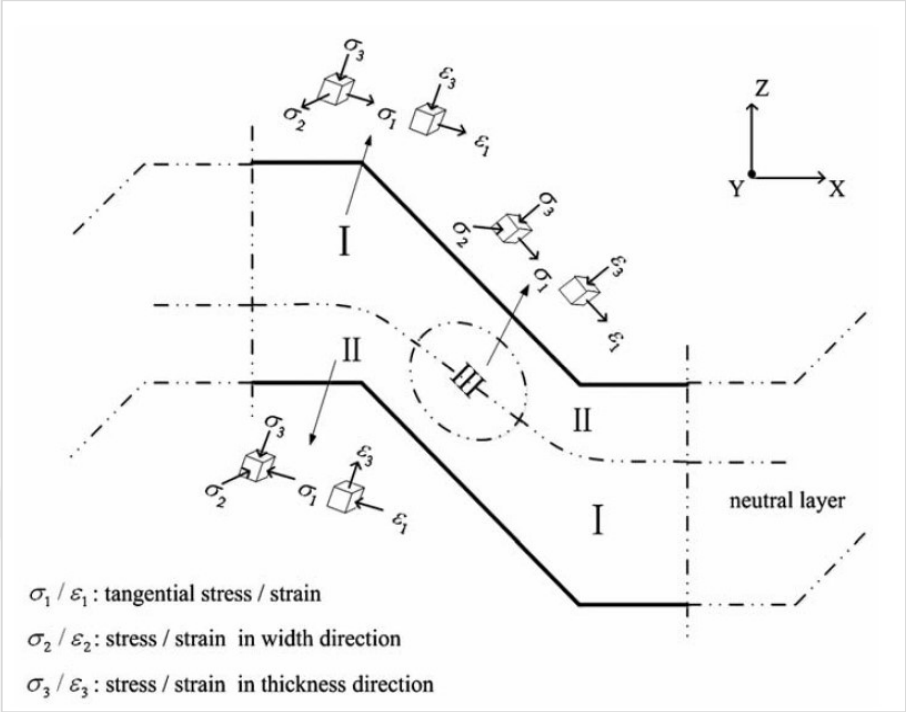

Figure 1.2.3.2: Stress-strain state analysis of grooved sample [14]

1.3. Deformation Mechanisms

There are two common plastic deformation mechanisms in crystals: slip and twinning. These mechanisms should be thoroughly understood to comment on the resultant mechanical behaviour [65].

1.3.1. Slip Mechanism

Plastic deformation is generated by dislocation motion in a process called *slip*, which includes sliding one plane of atoms over other planes (slip planes) in crystallographic directions (slip directions) (see Figure 1.3.1.1).

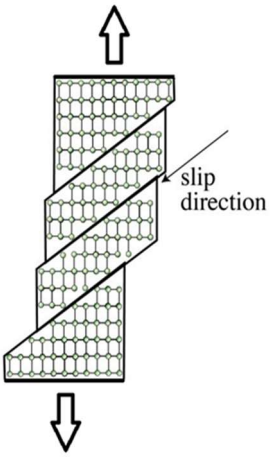

Figure 1.3.1.1: Motion of atoms during dislocation slip

In Figure 1.3.1.2, the unit vector d stands for the slip direction of the plane, and the unit vector n represents the normal of the slip plane. The material can be considered to be continuous if the slip direction is on the slip plane [62].

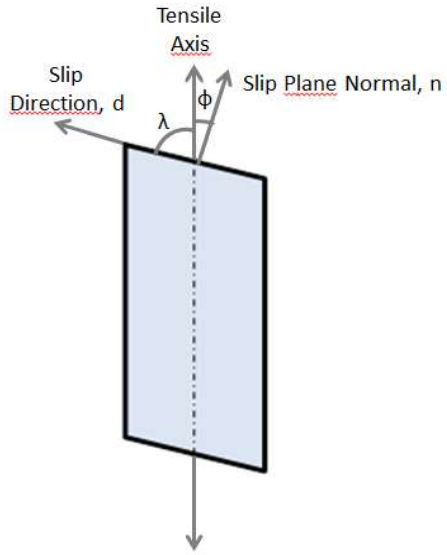

Figure 1.3.1.2: Demonstration of slip elements of a cyrstal under uniaxial tension

Sliding of a slip is triggered with a particular value of stress τ_r. This particular stress value is called critical resolved shear stress, which can be calculated by Schmid's Law [63]:

$$\tau_r = \sigma.\cos\lambda.\cos\phi \quad (6)$$

λ is the angle between the tensile axis and the slip direction, and ϕ is the angle between the tensile axis and the slip plane normal as shown in Figure 1.3.1.2. In the Eq.(6), $\cos\lambda.\cos\phi$ is termed as the Schmid factor. According to this law, slip process begins when the greatest Schmid factor is reached [65].

Slip systems are comprised of slip planes and slip directions. Both the slip directions and the slip planes have significant crystallographic structures. Density of atoms in a slip plane is the highest comparing to the other planes. The slip direction is the direction that corresponds to one of the smallest lattice translation vectors in the slip plane [64].

Three types of slip systems exist:

- Face-centered cubic (FCC) slip – it is seen on the close-packed plane. There are 12 slip systems in FCC crystals. Some examples are Cu, Al, Ni, Stainless Steel 304, etc.
- Body-centered cubic (BCC) slip – are on the plane of the shortest Burgers vector. It has 12 slip systems, and includes materials such as very low carbon steel and β-Ti.
- Hexagonal close packed (HCP) slip – more restricted than the other crystal structures. Slip occurs mostly on the densely packed basal planes. The total number of the slip systems is 3. Mg and Zn are the two examples that have the HCP structure [64].

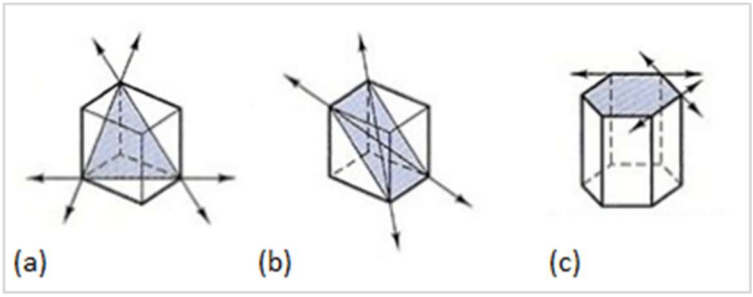

Figure 1.3.1.3: Unit-cell geometries and the main slip planes of (a) FCC, (b) BCC and (c) HCP crystals

The slip planes and slip directions of these different crystal structures are tabulated below. The occurence of slip is also stated for the specific slip planes here. In Figure 1.3.1.3, these slip planes are schematically shown in the related unit-cell structures.

Table 1.3.1.1: Slip elements in different crystal structures.

crystal	occurence	slip planes	slip directions
FCC		{111}	<110>
BCC	more common less common	{110} {112},{123}	<111>
HCP	more common less common	basal plane prismatic& pyramidal planes	close packed directions

Slip is observed along the <110>{111} system, which is composed of 12 discrete systems, for fcc metals. For bcc geometry, slip occurs along the <111> direction. The slip planes containing this slip direction are {110}, {112} and {123}. In hcp crystals, slip takes place on the close packed basal plane (0001). It can also be observed on the $\{1\bar{1}01\}$ or $\{1\bar{1}00\}$ plane families. Also, the slip direction is $<11\bar{2}0>$ for all these planes [65].

It is a fact that the structure reorients itself during deformation. An fcc crystal exposed to uniaxial compression and tension is taken into consideration [63, 67]. In Figure 1.3.1.4, the tensile axis is shown in the stereographic triangle having the corners [100], [110] and [111]. The primary slip system in the triangle is [101]$(11\bar{1})$ system since it has the greatest Schmid factor among all the orientations. If the axis of tensile force applied is on a boundary of the basic triangle, two systems are considered as equally favored. The most favored second system of the mating triangle is defined as the conjugate system [65].

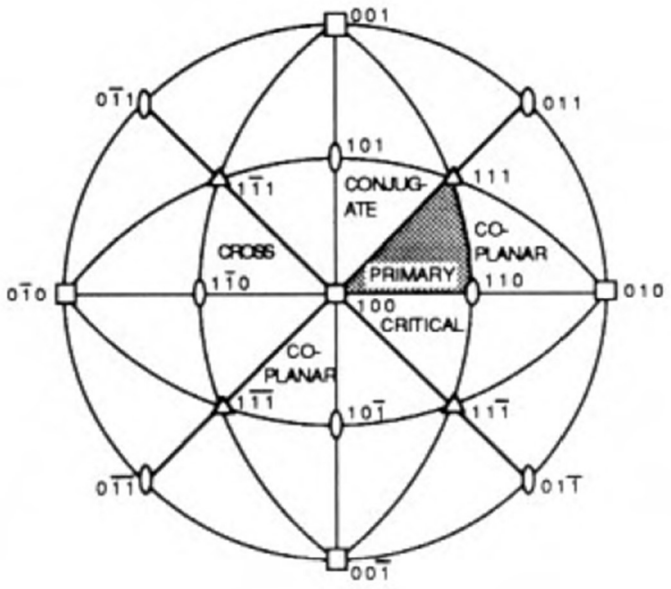

Figure 1.3.1.4: Schematic of slip systems for fcc cyrstals [65]

There are three other systems, which are the cross slip system, the coplanar system and the critical slip system [63, 67]. The cross-slip system, namely [101] $(1\bar{1}\bar{1})$, can be triggered if a screw dislocation activating along the primary system comes across an obstacle and passes through the cross slip plane [65]. Cross slip process in an fcc material is shown in Figure 1.3.1.5.

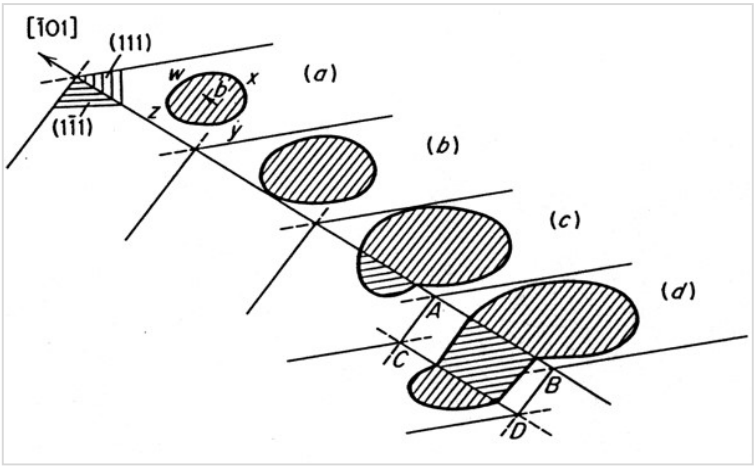

Figure 1.3.1.5: Cross slip in an fcc crystal [66]

Coplanar slip systems share the primary slip system with distinctive slip directions. If a tensile force is exerted into a crystal, the tensile axis orientation alters, and follows the primary slip direction. On the other hand, because of limitations, the tensile axis does not change, and the crystal rotates. As a result, a primary slip on [101] (111) leads to a rotation for the tensile axis toward [101] direction. When it approaches the boundary [100]-[111], the conjugate and primary systems can be equally favored. Therefore, the synchronous influence of [100] and [110] slips induce a rotation toward [211] on the boundary line. This is a characteristic behavior for fcc crystals, but there may be some exceptions for the materials which possess fcc crystals due to their stacking fault energy. For the materials having high stacking fault energy, conjugate slip occurs before arriving the [100]-[111] boundary. On the other hand, an overshoot may be observed on the conjugate triangle for low stacking fault energy materials before reaching the stable [211] orientation. These kinds of abnormalities occur because there may be hardening differences caused by slip between the conjugate and primary systems. In Figure 1.3.1.6, the crystal rotation during tension and compression is depicted schematically [65].

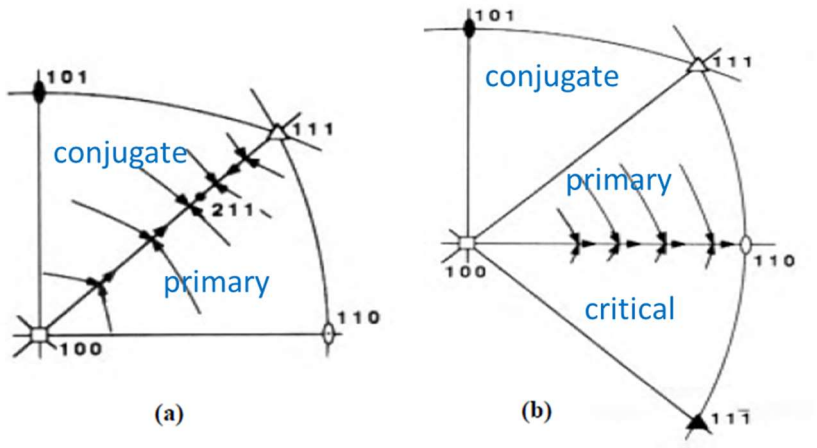

Figure 1.3.1.6: Single crystals loading. (a) rotation of the axis to [211] in tension, (b) rotation of the axis to [110] in compression [63].

Rotation of axis toward the normal of the primary plane is observed during compression. The axis of compression rotates to [111] until it approaches the [100]-[110] line. The critical and primary slip systems are favored equally at this point. A rotation toward [110] stable end orientation occurs progressively because of the simultaneous effect of these systems. Slip can occur on different systems when the stresses on them are the same and reach the critical value. Two slip systems are activated on the basic triangle boundary lines, while several other systems are operated for corners. Eight systems are activated with a uniaxial stress along [001], six systems are activated with a stress along [111], and four systems are activated with a stress along [011] [62, 67]. There is a difference between the slip in polycrystalline materials and the slip in single crystals. For polycrystalline materials, more constraints are imposed on different crystals. Displacements through grain boundaries should be matched to satisfy compatibility. It can be inferred that grain boundaries limit the flow so that higher hardening and yield stress values are determined in polycrystals [63, 67, 68].

1.3.2. Twinning Mechanism

Twinning is a plastic deformation mechanism observed basically at high deformation rates and low temperatures [63, 67-69]. Twin regions are like mirrors for the lattice orientation at one side as seen in Figure 1.3.2.1.

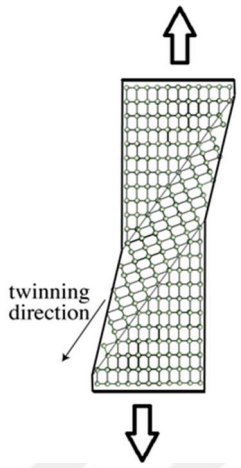

Figure 1.3.2.1: Motion of atoms during deformation twinning

The non-twinned region is defined as the matrix. Shear deformation occurs on crystallographic planes for both twinning and slip, but there are a few differences. Shear displacement in twinning is a ratio of the distance between atoms, whereas slip displacement is a total multiple of the burgers vector's length. Contrary to slip, there is directionality for twinning. For example, twinning is observed along the direction of $[11\bar{2}]$ on the (111) plane in fcc structures, but it does not occur along the $[\bar{1}\bar{1}2]$ direction. On the other hand, slips on the same plane along opposite directions are equivalent. In addition, the lattice is suddenly reoriented in twinning unlike slip, which has gradual rotation [63, 70].

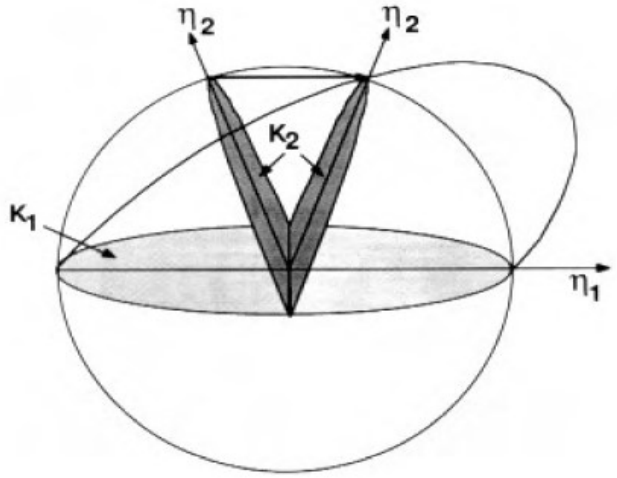

Figure 1.3.2.2: Formal twinning notation, depicting a homogeneously sheared hemisphere [63]

The hemispherical crystal exposed to twinning shear and the ellipsoidal shape which is the distorted appearance of this crystal is described in Figure 1.3.2.2. K_1, K_2, η_1, η_2 are the elements of twinning here. The plane including η_1 and η_2 and the normals of K_1 and K_2 is the shear plane. K_1 is the mirror plane (twinning plane) which remains undistorted like the plane K_2. Twinning occurs on K_1 and along shear direction η_1. The other direction, η_1 is on the K_2 plane and perpendicular to the intersection line of K_1 and K_2. Before and after twinning, only η_2 direction on K_2 plane makes the same angle with any direction on K_1 plane [71]. Different crystal structures have different twinning planes and directions as seen in Table 1.3.2.1.

Table 1.3.2.1: Twinning elements in different crystal structures.

crystal	**K_1**	**K_2**	**η_1**	**η_2**
FCC	{111}	{11$\bar{1}$}	<11$\bar{2}$>	<112>
BCC	{112}	{11$\bar{2}$}	<11$\bar{1}$>	<111>
HCP	{10$\bar{1}$2}	{$\bar{1}$012}	<10$\bar{1}$1>	<$\bar{1}$011>

The form of twins are usually sharply pointed and lenticular because of two main factors. One of them is the strain energy produced at the twin-matrix interface and the other is the introduction of a novel surface and the resultant surface energy. The energy required is minimized when the twin is long and narrow. It is asserted that the twins in fcc and bcc crystals are thin, while hcp twins are thicker [70, 71].

Twinning behavior is affected by various factors. These are strain rate; grain size; temperature; crystal orientation; alloy composition and texture. All these parameters influence the way the metal deforms. From this perspective, stacking fault energy is an essential factor for twinning deformation. In low SFE metals, linear dislocation arrays and stacking faults are observed in contrast to high SFE metals, in which cross-slip is observed and random dislocation networks are shaped [69].

Twinning activity is usually increased at low temperatures because of less increase in the stress necessary for twinning compared to the increase in the stress necessary for slip. Planar dislocations, which decline the cross-slip ability of a material leading to early onset of twinning, may also be formed due to the decrease of deformation temperature. Local fine twins are formed in fcc metals having low SFE at low temperatures but thicker twins with localized flow may be seen at higher temperatures [69, 71].

An fcc metal having high SFE does not twin under normal conditions. However, in shock loaded Al-Mg alloys, twinning has been observed due to the solid solution strengthening and the increase in flow stress at low temperatures under dynamic loading [72]. As seen in slip, twinning is obstructed at grain boundaries, too. Moreover, the twin size is restricted by the size of the grains, and in refined structures, shorter twins are observed. Twinning acts like the grain boundaries which hinders growing twins and slip. As a result, it causes strengthening and high work hardening [65].

1.4. Deformation Texture in Metals

Crystallographic texture of a material is formed during deformation, phase transformation, solidification, recrystallization and grain growth. After thermomechanical treatments, deformation textures are formed and gain importance because of their influence on the mechanical properties. Textured metals generally show anisotropic behaviors. The factors affecting deformation texture are chemical composition, crystal structure, the rate, nature and quantity of the temperature and deformation [63].

Rather than rolling textures, torsion textures may give insight about texture formation after CGP, since it includes simple shear. In the following section, effects of CGP on the evolution of texture are discussed.

1.5. Effects of CGP on Texture and Formability

CGP alters the material texture. The sheet metal properties vary due to the testing direction of the material as stated by Park et al. [73]. This anisotropy is associated with the main crystallographic texture of the sample. The formation of the texture after CGP process is not only based on the amount of deformation on the material under the various passes, but also on the structure of the dies [56].

Resistance to thinning is denoted by r, which is defined as the ratio of strain of the width to the thickness of a sample under uniaxial tension [77]. If this value is high, formability of the material will be better. Several methods including groove pressing can increase this r value [56, 57]. Some studies on the correlation between the texture and the formability are conducted by Singh et al. [74, 75]. In addition, one of the most prominent works on drawability after groove pressing is carried out by Niranjan et al. [57].

Controlling the texture of the metal is the most substantial development in drawability, a formability technique [76]. A proper texture can increase the strength of the sample along the thickness direction so that higher r values are obtained. The advantages of the materials with high r values are both providing less thinning of wall and reducing the load of drawing. Increasing r value is difficult for the metals of fcc crystal structure like aluminum and copper, since the cube texture {100} <001> is formed strongly during annealing after cold rolling. Especially for fcc metals, numerous methods have been proposed to improve the r value. These are conshearing, unidirectional shear rolling, continuous confined strip shearing process (C2S2), differential frictional rolling, asymmetric rolling and dissimilar channel angular pressing (DCAP) [78-83]. r value improvements of these methods are shown in Table 1.5.1.

Table 1.5.1: Maximum r values attained by various processes [57]

process	material	r value at initial condition	maximum r value attained	orientation
conshearing	AA1100	0.64	0.98	0° to RD
C2S2 process	AA1050	0.7	1.1	0° to RD
unidirectional shear rolling	AA5052	-	1.1	45° to RD
differential frictional rolling	AA1050	-	0.98	0° to RD
DCAP process	AA1050	0.84	1.7	0° to RD
groove pressing	AA1100	0.83	1.14	45° to RD

1.6. Previous studies on AISI 304 and other FCC materials

Austenitic stainless steels include 0.03-0.25 wt% C, 8-20 wt% Ni and 18-25 wt% Cr. Amount of Ni and Cr provides oxidation resistance and high temperature strength. Although, some delta ferrite may be observed in the structure due to the composition and

thermomechanical processes applied, they are mainly austenitic at any temperature. These steels are non-magnetic and can be hardened via cold/warm working [84-87].

Among austenitic steels, AISI 304 is a most broadly used in industry. It composes about 50% of steel manufacturing and is utilized in almost all industrial applications, particularly in the form of sheet. Enhancing the mechanical properties of this material without altering the chemical composition would affect a broad area of production in terms of high strength to weight ratio and low cost. This can be succeeded via a severe plastic deformation method. Several studies have conducted to investigate some properties of austenitic stainless steels after severe plastic deformation [88-90], but the effects of CGP on AISI 304 stainless steel have not been analyzed yet. On the other hand, CGP method has been implemented for many fcc structured materials like Cu, Al and Ni [91-93]. As mentioned in the previous sections of this work, AISI 304 stainless steel has fcc crystal structure, so the studies on fcc materials may give an insight about the behavior and properties of it.

Krishnaiah et al. [91] used commercial purity copper to test the influence of groove pressing passes. After each pass, the vickers hardness values along the longitudinal direction were measured as demonstrated in Fig 1.6.1.(a). The average hardness value for the starting material was improved about two folds after the last pass. In Fig 1.6.1.(b), tensile property profiles with respect to pass number is seen. Yield strength of the annealed material increased quite a lot after the initial pass, while the ultimate tensile strength showed less increase. There are small decreases in the following passes for these parameters. On the other hand, ductility of the annealed sample continuously decreased. Finally, microstructures were investigated using optical and transmission electron microscopy (TEM) methods and it was observed that the grain size was diminished to about 0.5 μm from the initial 78 μm.

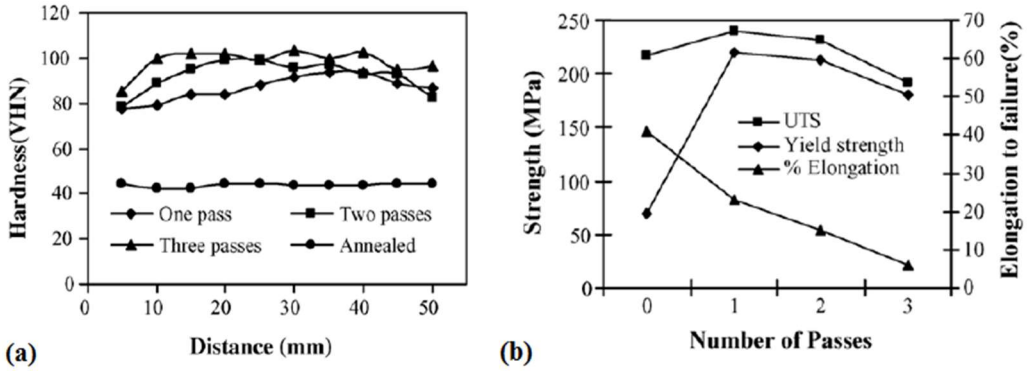

Figure 1.6.1: After room temperature testing: (a) the vickers hardness distribution along the longitudinal direction of the sample (b) tensile property change with pass number [91]

Morattab et al. [92] studied the mechanical property improvement and grain refinement of commercially pure Al. At the end of the experiments, engineering stress-strain curves at different passes were plotted as seen in Fig 1.6.2.(a). The alteration of mechanical properties was also depicted in Fig 1.6.2.(b). A noticeable increase in yield stress and tensile strength was determined after the process. These parameters reached their maximum value after the third pass and then decreased slightly.

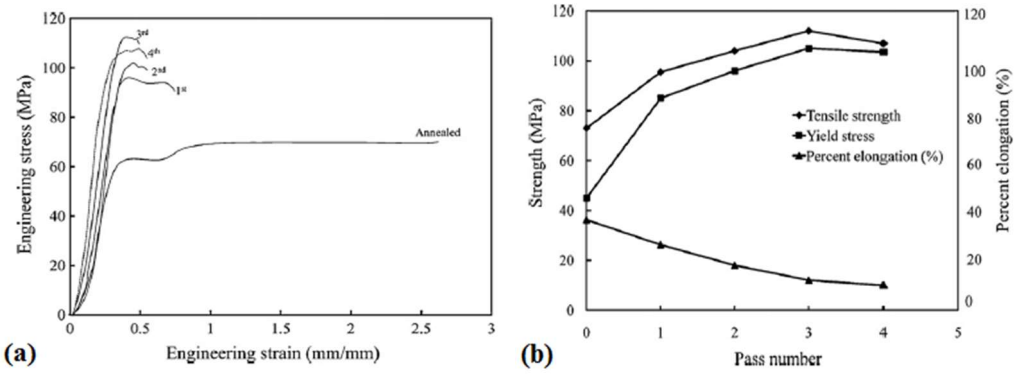

Figure 1.6.2: (a) Engineering stress-strain diagram of Al specimens for all conditions (b) variation in tensile properties with pass number [92]

It was discussed that the reduction of tensile properties after the third pass occurs due to the reversal straining, which is a type of Bauschinger effect [94, 95]. It was also proposed that the reason might be dynamic recovery [96].

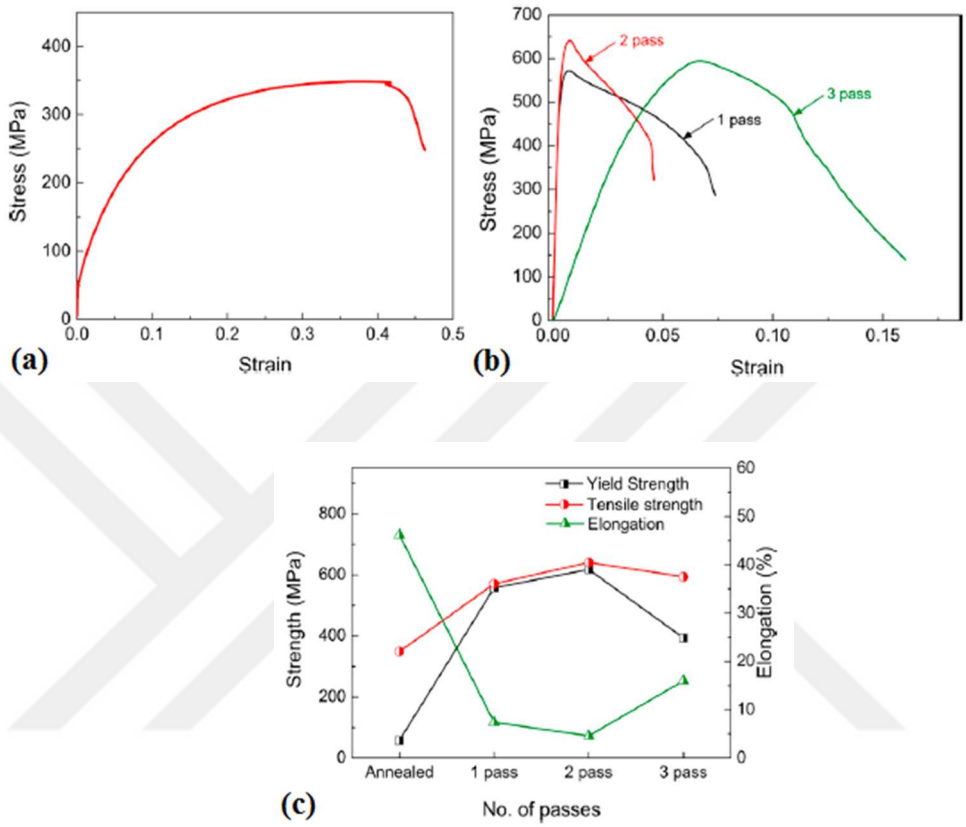

Figure 1.6.3: Engineering stress-strain curves of (a) annealed Nickel specimens and (b) CGPed Nickel specimens. (c) Tensile properties of nickel samples with number of CGP pass [93].

Mechanical behaviour of nickel sheets after CGP were investigated by Kumar and Raghu [93]. They have conducted three passes to annealed nickel sheets at room temperature and obtained the engineering stress-strain graphs as summarized in Fig 1.6.3. The significant improvement in strength was due to work hardening behaviour of metals. This improvement was continued with increasing strain since the slip motion was obstructed because of dislocation interactions with other dislocations and barriers [97]. Strain hardening behaviour of nickel is stronger than metals like aluminium as it has larger slip systems and lower stacking fault energy. The phenomenal increase observed

in strength is attributed to grain refinement and increase in dislocation density [93]. After the first and second passes, ductility is decreased but it significantly increased after the last pass. At high strains, dislocation annihilation can cause the regain of strain hardening ability which increases the ductility [98]. Elastic moduli of severe plastically deformed samples are different since grain boundary regions are volumetrically increased during processing [99]. Elastic modulus of the material was decreased after the third pass because non-equilibrium grain boundaries are rearranged to relatively equilibrium boundaries together with stress relaxation [100]. This is also demonstrated by the increase of the ductility after third pass.

1.7. Previous studies on Ti-15V-3Cr-3Sn-3Al and other BCC materials

The beta titanium alloys has been an alternative to the alpha-beta titanium alloys as they offer many advantages such as deep hardening potential, improved heat treatability and inherent ductility ascribable to their BCC lattice structure [101-103]. Particularly at higher strength levels, fracture toughness of beta titanium alloys is comparatively superior.

The first commercial beta titanium alloy, Ti-13V-11Cr-3Al was developed in the 1950's [104]. Among subsequent alloys, Ti-15.5Mo-6Zr-4.5Sn (Beta III), Ti-3Al-8V-6Cr-4Mo-4Zr, Ti-10V-2Fe-3Al and Ti-15V-3Al-3Sn-3Cr are the most outstanding ones [105]. Grade Ti-15V-3Al-3Sn-3Cr alloy is quite formable and has favorable bending properties at room temperature. It can be heat-treated and strip-rolled. This alloy was firstly manufactured for airframes. The other application fields contain tubing and tankage components, aerospace fasteners, flat-rolled products, foils, plates, castings and forgings [106].

The mechanical properties and microstructure of CGP processed beta titanium have not been investigated so far. However, CGP of very low carbon steel, which is another BCC structured material, has been studied by Khodabakhshi et Kazeminezhad [107]. In their research, it was stated that the coarse-grained structure of the metal was refined to an ultrafine grain range. Yield strength variation with increasing strain amount was plotted as seen in Fig 1.7.1.a. Moreover, dislocation density of the samples was measured and found to be effectively increased after the process (Fig 1.7.1.b). Electrical resistivity of the samples was also improved up to about 100% (Fig 1.7.1.c).

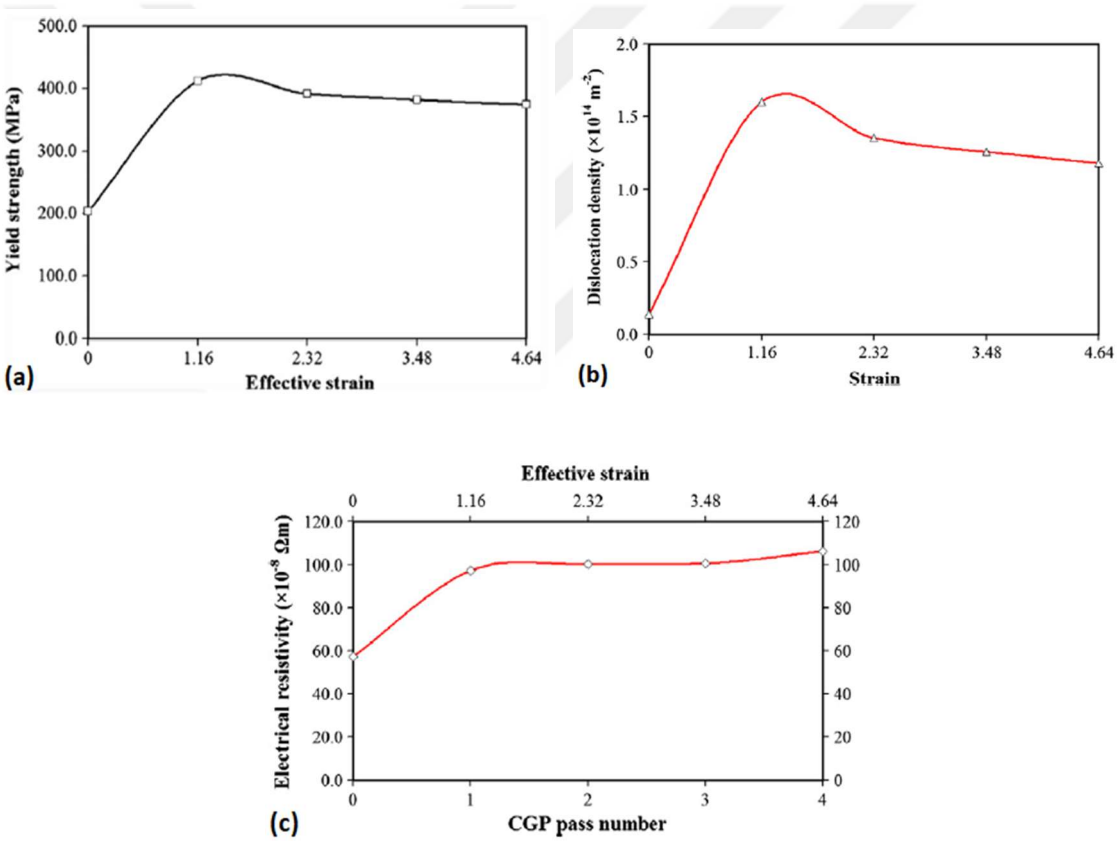

Figure 1.7.1: (a) Variation of yield strength with effective strain, (b) dislocation density change with increasing strain, (c) electrical resistivity of the sample before and after CGP passes [107].

1.8. Previous studies on Commercially Pure Zinc and other HCP materials

Commercially pure zinc was chosen to analyze the influence of CGP on microstructure and mechanical behavior of an HCP material. When unalloyed, the strength and hardness of zinc is higher than that of tin or lead, but not as high as aluminium or copper. In this study, it has been shown that enhancement of its mechanical properties is possible through a severe plastic deformation technique, which has not exist in literature. However, studies on another HCP material, magnesium alloy AZ31 may give an insight about the behavior of zinc [15, 109].

Sunil at al. [15] accomplished a fine grain size of 7 μm for AZ31 magnesium alloy from a grain size of 55 μm via groove pressing passes. They have investigated the effect of this refinement on some properties necessary for implant production. The processed samples have demonstrated improved corrosion resistance and increased hydrophilicity. Cell response to the samples was also promising. According to these findings, they have concluded that groove pressing may be a potential method to control degradation of magnesium alloys and to improve bioactivity for implant implementations.

Table 1.8.1: Test conditions [109]

Specimen	Forming Temperatures	Route
I	1^{st} cycle at 250°C -> 2^{nd} cycle at 200°C ->3^{rd} cycle at 150°C ->4^{th} cycle at 150°C	A
II	1^{st} cycle at 250°C ->2^{st} cycle at 200°C ->3^{st} cycle at 150°C	B
III	Constant temperature at 250°C	A

Another research has been done by Fong et al. [109] on the formability improvement of AZ31 alloy by groove pressing. Two different routes were selected with decreasing and constant temperatures as indicated in Table 1.8.1. In this study, specimen is rotated 90° about the normal direction between each cycle in Route A while there is no rotation in Route B. The crack was determined after the 3rd cycle in Route B while no crack was observed for specimen I which underwent Route A under the same temperature conditions. At a constant temperature of 250°C, five cycles were completed without fracture for the specimen III. Microstructural evolution was examined for all the cycles and a plot was formed for the Specimen I as seen in Figure1.8.1. Hardness increase was about 47% and average grain size reduction was about 86% for this specimen. Therefore, it was concluded that the alternate rotation is effective to prevent fracture by decreasing the repetitive tensile stresses in the same region of the material.

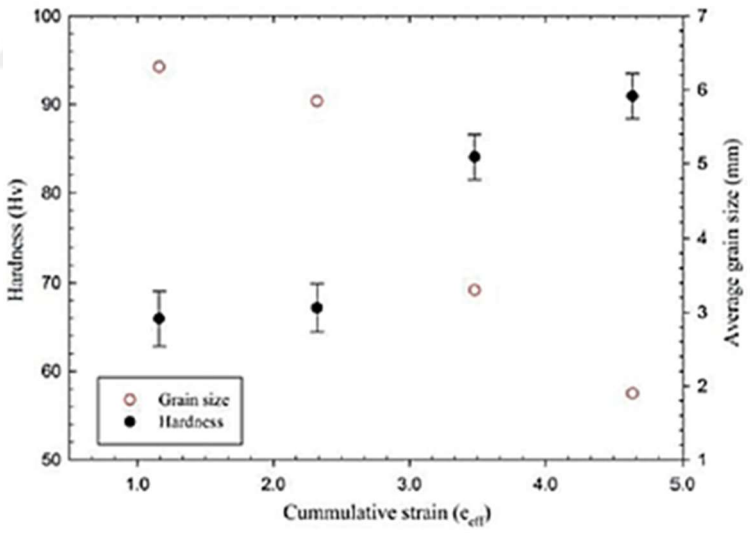

Figure 1.8.1: Average hardness and grain size of Specimen I against the theoretical total cumulative strain [109]

1.9. Statement of Objectives

The objectives of this study can be stated as follows:

1. Implementing CGP routes on different materials, which have not been studied yet, to enhance the mechanical properties with refined microstructures at room temperature.
2. Analyzing microstructures observed during CGP by altering the applied route.
3. Measuring the mechanical properties of samples before and after the application of CGP routes to demonstrate any difference.
4. Correlating the mechanical behavior with the altered microstructures.
5. Demonstrating the mechanical twinning mechanism activation in commercially pure zinc.
6. Comparing the influences of CGP routes for different crystal structures.

CHAPTER II

EXPERIMENTAL METHODS

Three materials with different crystal structures were analyzed in this thesis. Hot rolled 304 stainless steel sheet of thickness 1 mm in annealed condition with a composition of 18.19% Cr, 8.14% Ni, 1.53% Mn, 0.018% C in weight and Fe balance was selected as an FCC material. As-received material was almost isotropic according to the tensile test results. Ti-15V-3Cr-3Sn-3Al and commercially pure zinc, both having 0.5 mm thickness were utilized as BCC and HCP structured metals. Anisotropy was observed for commercially pure zinc after initial tests while titanium alloy was determined as nearly isotropic.

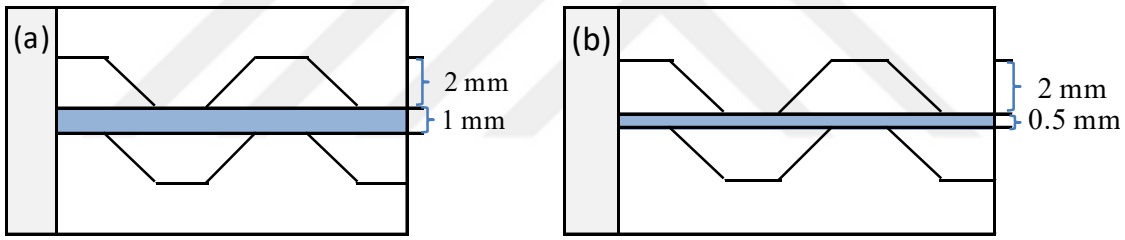

Figure 2.1: Schematic view of (a) AISI 304 and (b) Ti-15V-3Cr-3Sn-3Al/ commercially pure zinc between CGP dies

At ambient temperature, they were processed under a hydrolic press having a maximum capacity of 200 tonnes. For titanium alloy and austenitic steel, the amount of press was set to around 35 and 75 tonnes respectively, while it was 10-12 tonnes for commercially pure zinc. Pressing and flattening operations were performed at a 1 mm/sec rate. Length and width of each metal sample were 104 mm corresponding with the dimensions of die, and they were coated with a thin layer of lubricant before being placed.

Five routes are described and demonstrated schematically in this work (Figure 2.2). If the created groove edges on the sample at the initial pass are parallel to the groove edges of the die, this pass is defined as a pass along TD. Therefore, all the passes of the route A are along TD since the sample is not rotated around the normal direction between the passes. For route B, rotation is 90 degrees following each pass; while rotation angles for the third and forth passes are respectively -90° and 180° for route C. The fourth route includes a rotation sequence of 90°, 180° and 90°; whereas the last pass of the last route is 180° again.

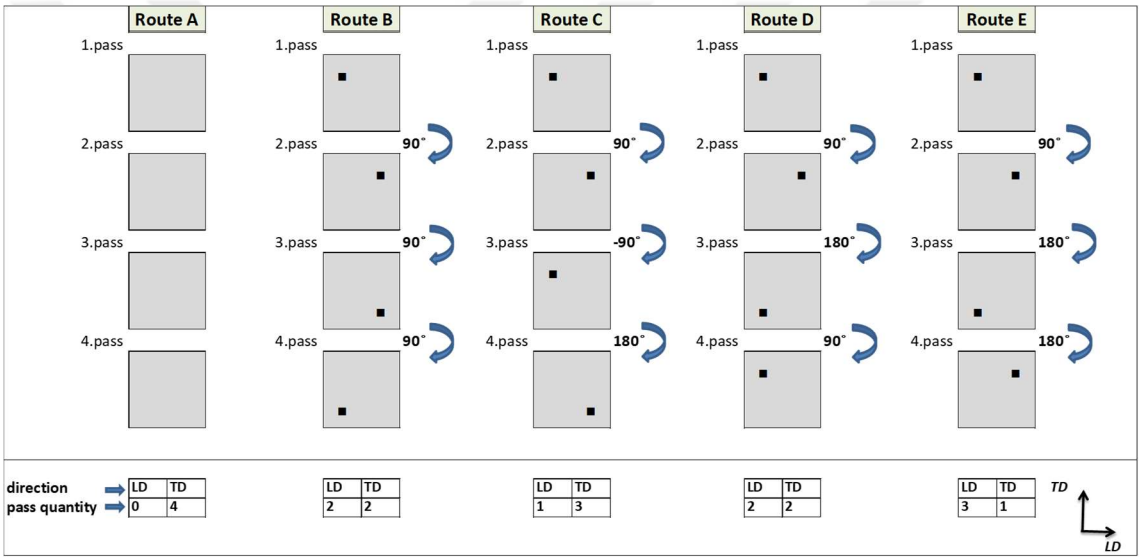

Figure 2.2: Description of CGP Routes

The motivation of this plan is to demonstrate the effects of processing path on the mechanical properties with regard to directionality. In route A, groove edges are consistently in line with the transverse direction of the sample during pressings. Two parallel and two perpendicular passes with respect to groove edges were applied for routes B and D in different orders in order that the sequence effect could be examined according to the outcomes of these two routes. Besides the only perpendicular pass to the groove edges for route C, one parallel pass is conducted for the last route enabling the effect of

pass quantity of different directions to be analyzed. Under each route, pass numbers in both LD and TD are shown in Figure 2.2.

The pressings was conducted as full stroke at the beginning of the study, but it was observed that the samples were mostly fractured during the second pass. This failure was in the second pressing of the second pass for stainless steel and titanium alloys while it was seen in the first pressing of the second pass for zinc samples (Fig 2.3). In order to eliminate the fracture, some solutions like altering the process heat or the amount of stroke could be suggested. In this study, stroke amount was adjusted to 50% to complete all the passes since heating would lead to dissipating energy.

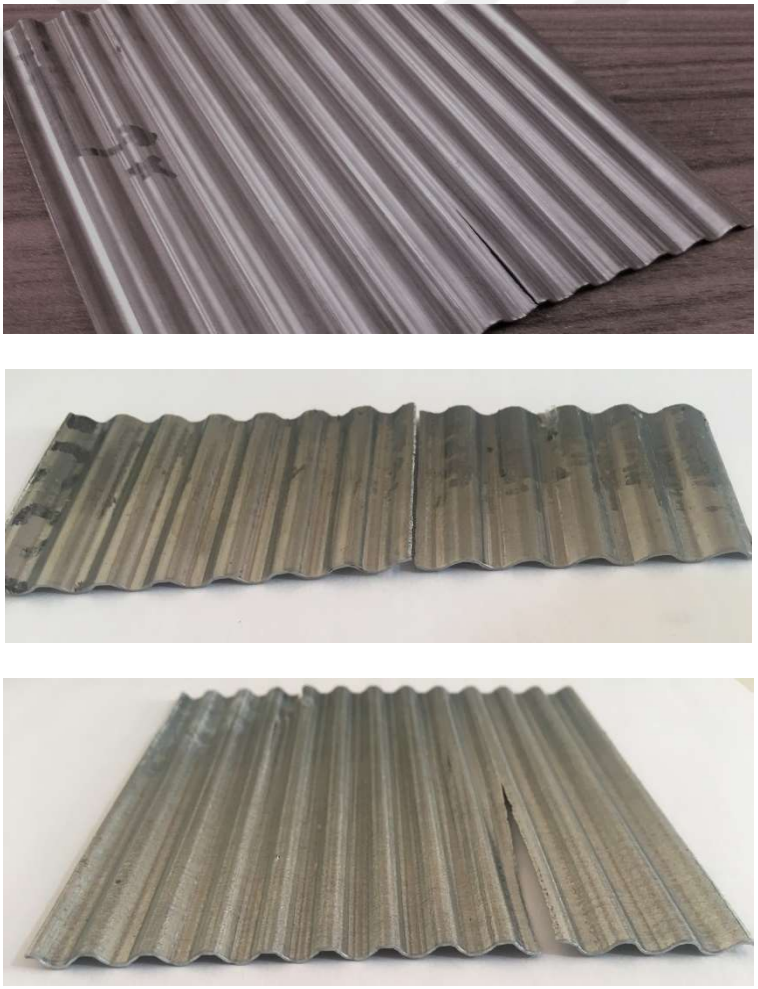

Figure 2.3: Fractures observed in (a) AISI 304, (b) Ti-15V-3Cr-3Sn-3Al and (c) commercially pure zinc

As mentioned in the first chapter of this work, the effective strain imposed on the material after the first pass is 1.16 for the full stroke pressing, and after any pressing of the second pass, it becomes 1.74 [57, 58]. In the light of this calculation, it can be understood that the materials in this study were fractured at a strain rate between 1.16 and 1.74. If these two values are considered to be the limits for the total strain of a route composed of four passes, the boundaries of optimum strain value for a pass will be between 0.14 and 0.22. The greatest strain value lying in this interval was determined to be 0.21 corresponding to a shear angle of 20° after the initial tests [59]. Hence, the optimum shear angle for these three materials was selected as 20° (Fig 2.4) to complete all the routes, and the amount of pressing strokes were adjusted considering this angle. CGPed metals have been characterized using several methods including numerical analysis, optical microscopy, mechanical experiments and hardness tests.

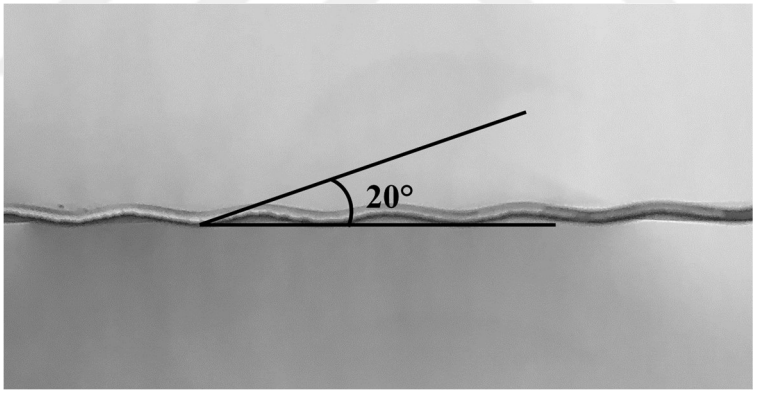

Figure 2.4: Shear angle of a sample after pressing

Numerical analysis for accumulated strain and pressing force during a CGP pass was performed via Marc Mentat utilizing rectangular elements. Even though both plane strain and 3-D conditions present very similar results [110], plane strain analysis was implemented because of its efficiency. Constrained groove pressing dies were assumed to be rigid with a coefficient of friction, 0.1. For AISI 304 stainless steel sample, the maximum force required for accomplishing a single pass reaches 800 kN due to the force-

upper die stroke distance graph (Figure2.5). Distance is defined as zero when the upper die touches the sample as seen in Fig 2.1. It reaches up to one when the upper die descends one milimeters. The simulated value is in line with analytical calculations based on the following bending equation [59, 111]:

$$F_{max} = nk\frac{\sigma_u L h^2}{t} \quad (7)$$

In this formula, n is the number of groove edges, t is the groove width, h is the sample thickness, L is the length of the sample, σ_u is the ultimate tensile strength of the sample and k is a constant determined for AISI 304 based on the die [108]. When all the parameters are put into the equation for a steel sample, the maximum force becomes approximately 780 kN. Similar verifications can be done for the other two materials.

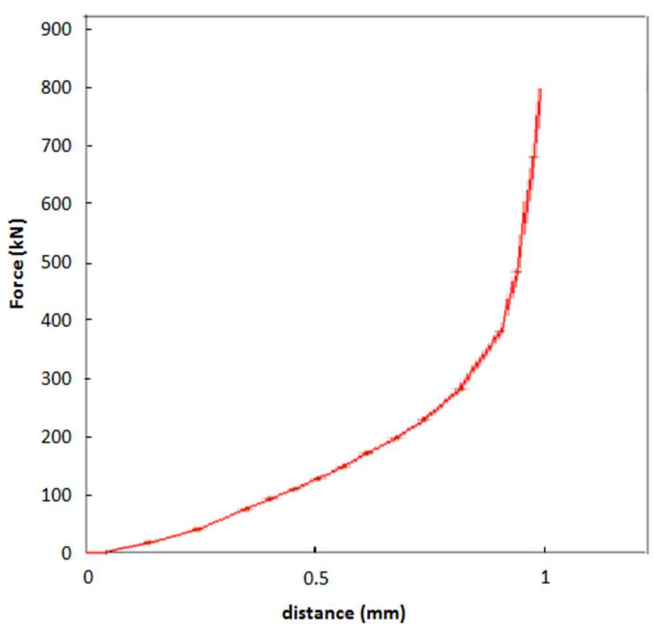

Figure 2.5: Simulated force-displacement curve for a CGP pass of stainless steel samples

The simulation for the effective strain per press is demonstrated in Figure2.6. This strain analysis has been performed for AISI 304 stainless steel sample, which is valid for the other samples as well. Accordingly, the sheared regions accumulate a strain around 0.2 as seen in Figure 2.6, which is consistent with the analytical calculations. Assuming

this strain is the same for all the pressings and flattenings, the aggregate strain comes about 1.6.

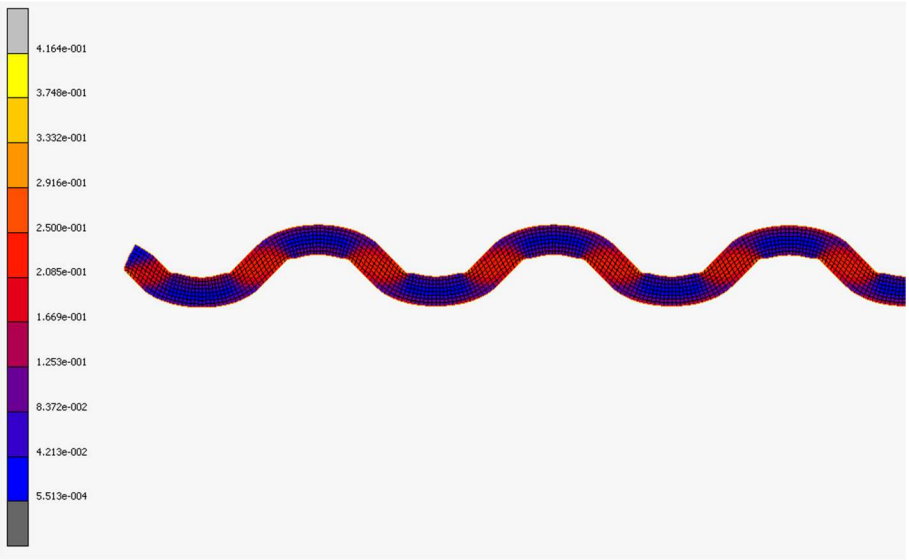

Figure 2.6: Corresponding strain distribution in the processed sheet

For microstructural examinations, specimens of SS304, Ti-15V-3Cr-3Sn-3Al and commercially pure copper sectioned from different locations of the CGPed sheets were mounted, ground, polished, and etched. Sectioning was accomplished with an Ecocut Electronica electro discharge machine using a water based lubricant. Then, the specimens were mounted in epoxy-cure solution to be handled practically. Abrasive removal of material from the surface was done with silicon carbide grinding papers of 600, 800, 1000 and 1200 grit, sequentially. Finally, specimens were polished using 1 μm and 0,25 μm alumina suspension on a special cloth. Electrolytic etching was performed for AISI 304 using a solution containing 10g oxalic acid powder in 100 ml distilled water at 6 V and 0,3 A for three minutes. Kroll's reagent (2 ml HF + 5 ml HNO_3 in 100 ml distilled water) was applied for 1,5 minutes to etch Ti-15V-3Cr-3Sn-3Al alloy. Etching of commercially pure copper was performed in a 5% HCl solution for 14 minutes.

Mechanical behavior of the samples was investigated by means of an Instron 8872 servo-hydrolic test frame with a digital 8800MT controller system. Monotonic tension tests were performed for the tension samples having a dog-bone shape. These samples had a gage section of 1 mm x 2.96 mm x 15 mm for austenitic steel and 0.5 mm x 2.96 mm x 15 mm for beta titanium and zinc.

For all the research materials, the orientation of the tension specimens were both along longitudinal and transverse directions of the processed samples. All the samples were tested at a strain rate of 10^{-3} s^{-1} at ambient temperature. Some of the experiments were repeated on three specimens in order to check repeatability and errors stemming from shape effects.

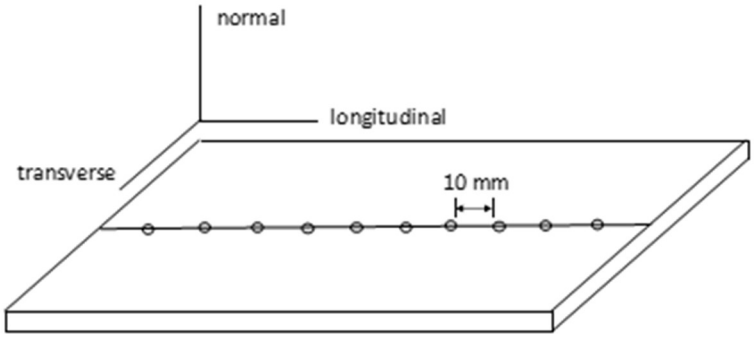

Figure 2.8: Micro-hardness measurement locations along the central line of the sample

Hardness tests were conducted by using FM 300e digital microhardness test machine to verify mechanical strength of the samples. In microhardness testing, a diamond indenter with a specific geometry is forced into the samples, and the indented areas are determined by measuring the diagonals of the indentation.

For Vickers microhardness testing, the indenter is a pyramidal diamond with face angles of 136°. The Vickers hardness number (Hv) is calculated by dividing the applied load by the indented area on the surface of the sample [112].

As seen in Figure2.8, measurements were obtained after each pass along the longitudinal direction at 10 mm intervals on the central line to investigate the homogeneity of the CGP process. Nine or ten hardness values were recorded per pass under 1 kgf load with a holding time of 10 s.

Erichsen tests has also been conducted to explore the formability. One sample from the as-received material, and another sample after the last pass of route E has been cut in the form of square. Clamping force on the samples was specified as 10 kN, and test speed was set to 10 mm/min. Experimental methods are schematically summarized in Figure 2.9.

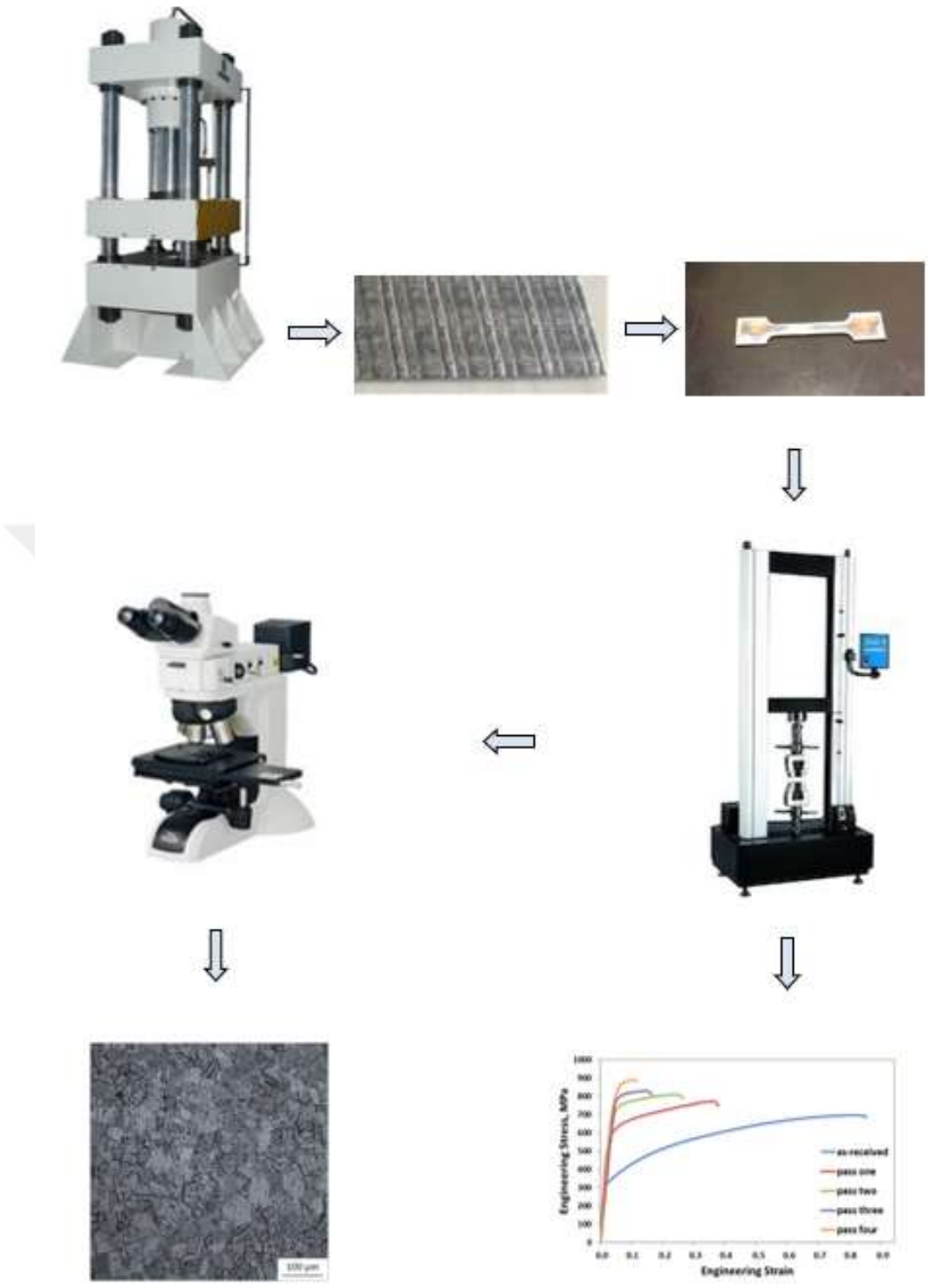

Figure 2.9: Summary of experimental techniques in this research

CHAPTER III

RESULTS & DISCUSSIONS ON AISI 304

Microstructural investigations will be explained together with mechanical behavior results for AISI 304 stainless steel in this section.

3.1 Microstructural Evolution

Annealing twins are present in the microstructure of the as-received material as seen in Figure 3.1.1(a). On the basis of the measurements taken from this optical microscopical image, average grain size was calculated as 40 μm. After the initial pass, grain refinement was recorded to be an average of 30 μm. Considering the level of refinement, significant difference was not observed among the processing routes after 4 passes leading to an average grain size in the range of 20-25 μm.

Visual examination after the CGP deformation indicates that an activation of mechanical twinning has occurred. Figs. 3.1.1(b) via 3.1.1(g) demonstrates the microstructural evolution briefly. Images of the intermediary passes are not displayed in this figure, but their data have been used to analyze the grain refinement rate. The analysis shows that:

1. The rate of grain refinement slows down, when the imposed strain during CGP is increased, as noted in other SPD methods [113-116].

2. As compared to other SPD techniques, the effectiveness of CGP is lower in grain refinement, since it imposes a simple deformation field where slip is cancelled out by reverse slip during flat pressing [60].

3. Strain path is not very effective in influencing the grain size for AISI 304 stainless steel.

4. Macroscopic fracture was not recorded in any route because of the adjusted pressing stroke amount.

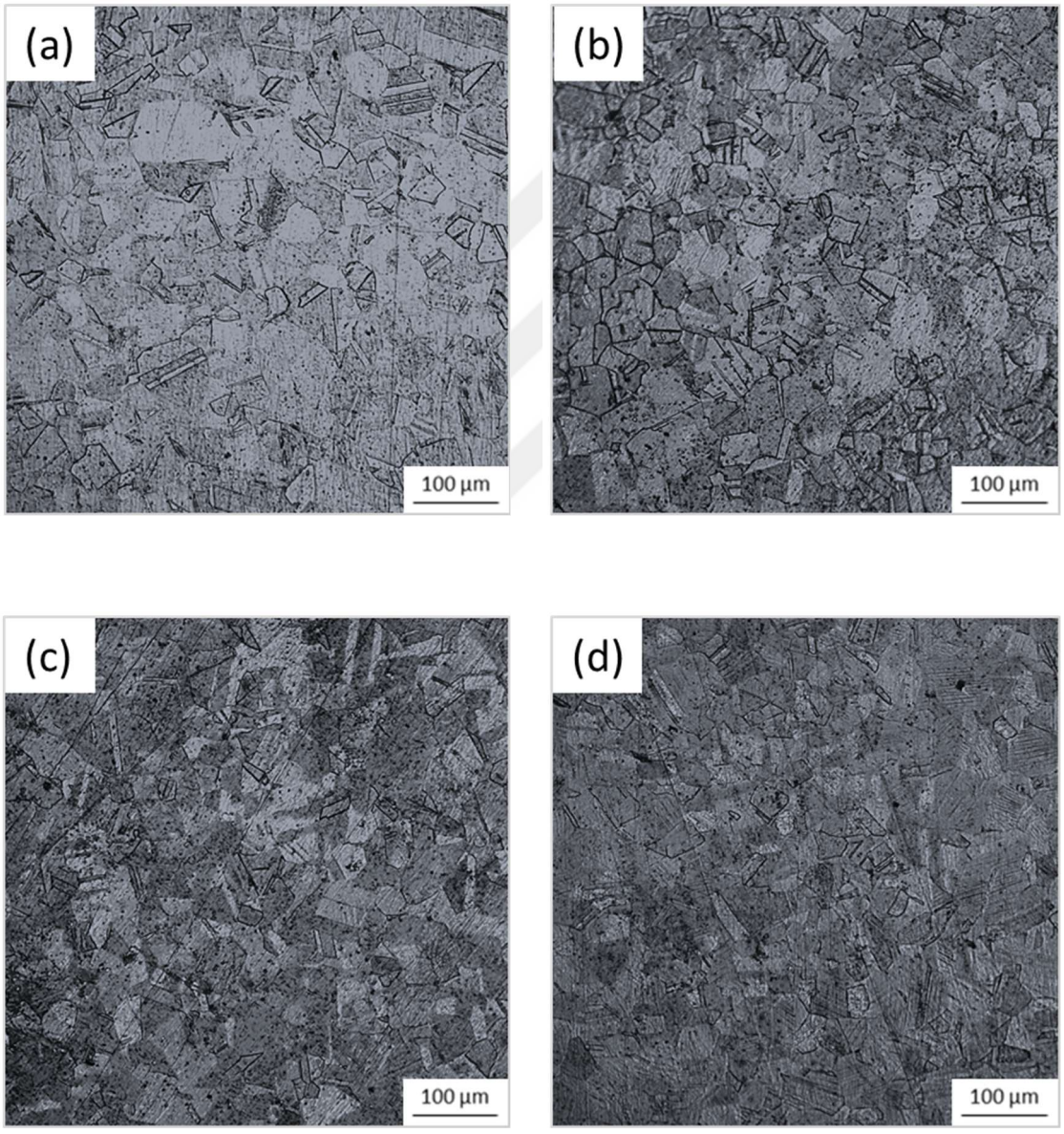

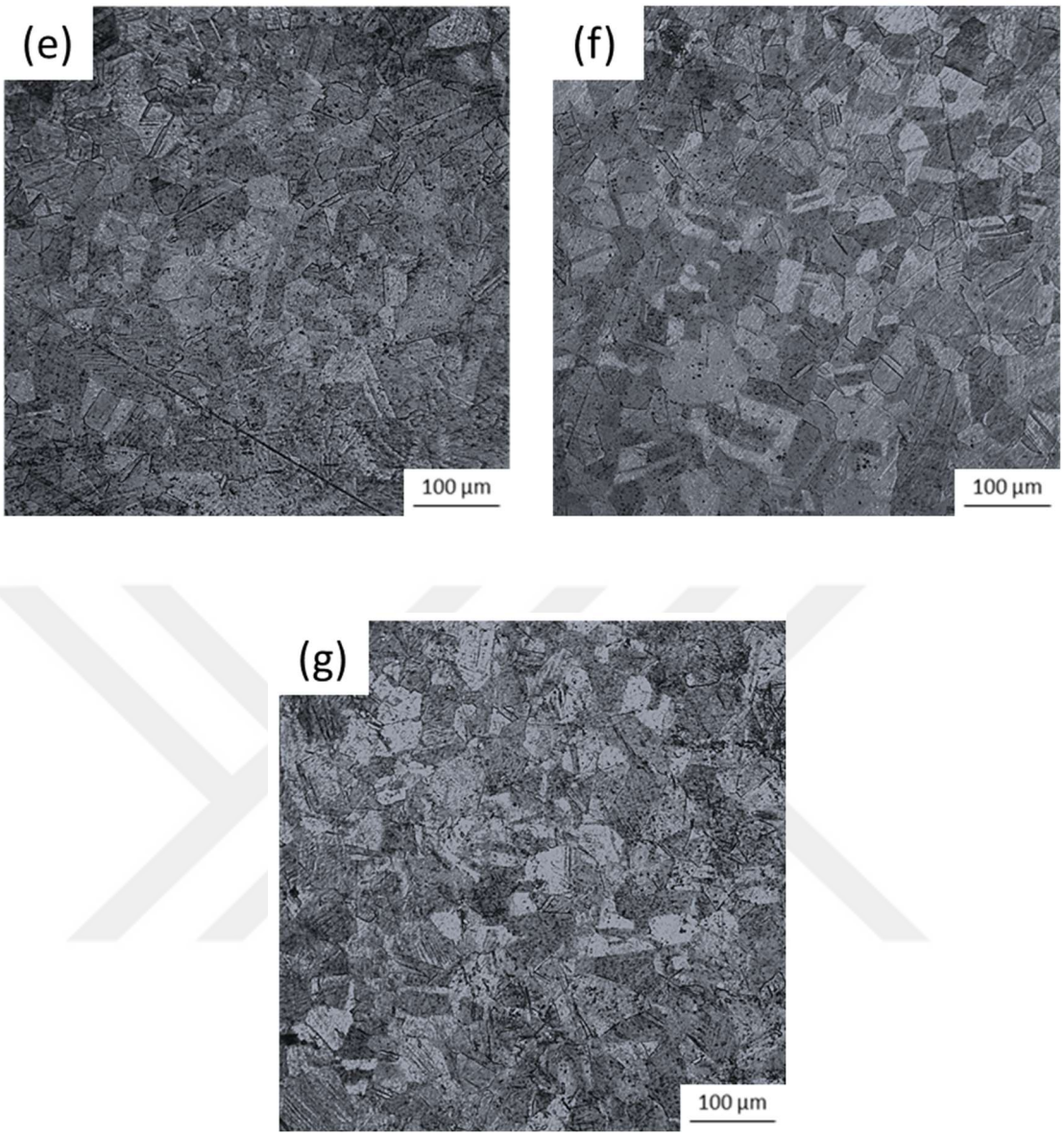

Figure 3.1.1: Grain structure of AISI 304 stainless steel: (a) annealed; (b) after 1 pass; (c) after 4 pass of the route A; (d) after 4 pass of the route B; (e) after 4 pass of the route C; (f) after 4 pass of the route D; (g) after 4 pass of the route E

3.2 Mechanical Behavior

The stress-strain response of AISI 304 stainless steel along both longitudinal and transverse directions is presented in Figure3.2.1. Strength improvement is prevalent for almost all passes after CGP deformation. Yield strength values increased more than two times for all routes, whereas ductility values decreased noticeably.

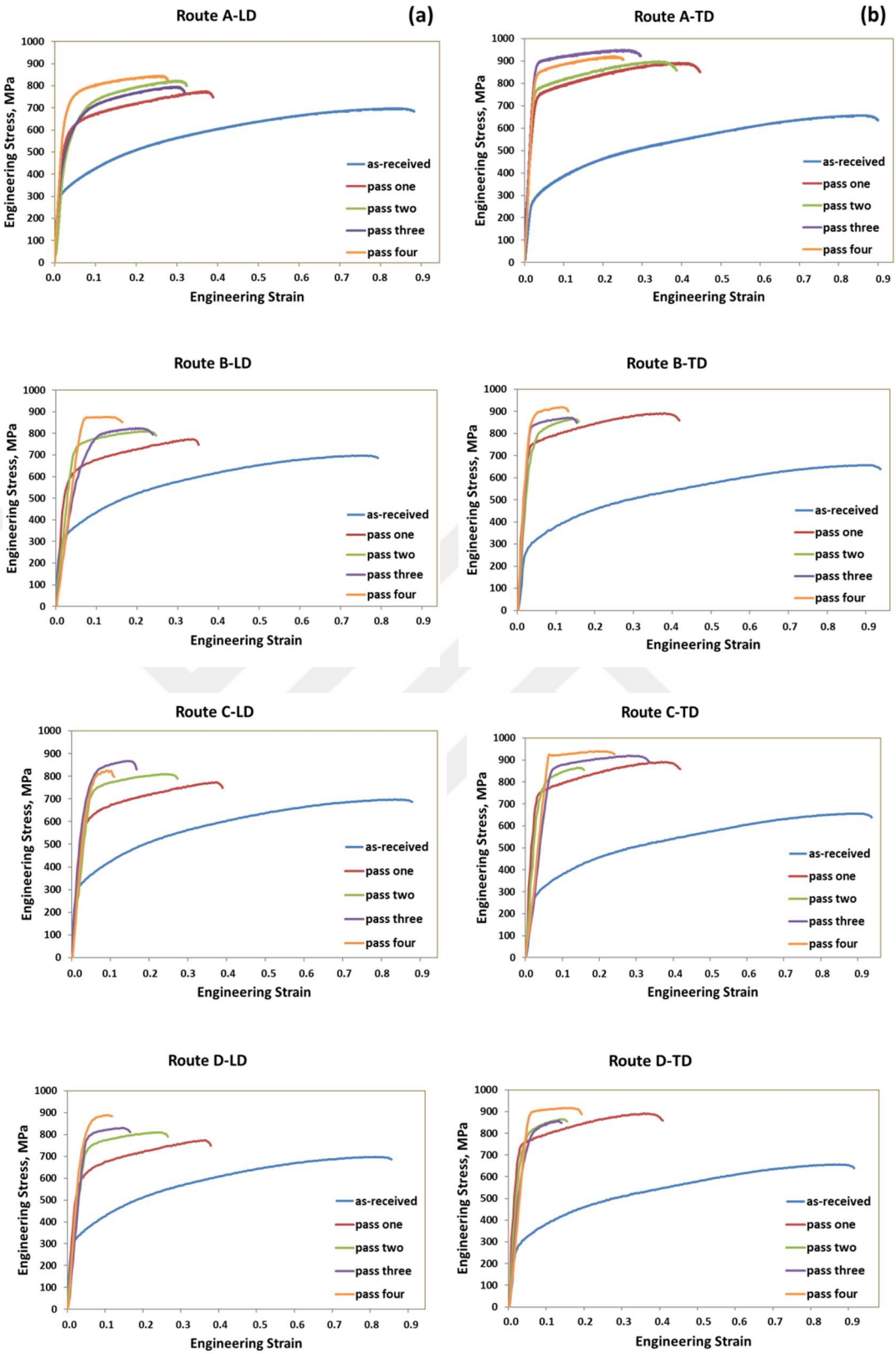
Route A-LD
(a)
Route A-TD
(b)
Route B-LD
Route B-TD
Route C-LD
Route C-TD
Route D-LD
Route D-TD
Engineering Stress, MPa
Engineering Strain
as-received
pass one
pass two
pass three
pass four

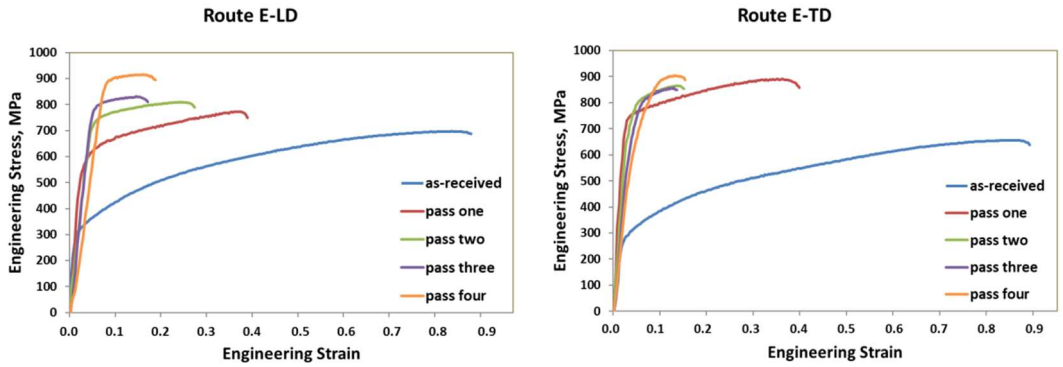

Figure 3.2.1: Stress-strain curves of stainless steel samples along (a) longitudinal direction and (b) transverse direction

The best strength improvement is nearly 32%, and occurs in LD for route E compared to 41% in TD belonging to route C. This result may stem from the fact that route C has three passes in which the groove edges are parallel to TD, and for route E they are perpendicular to TD. Route A has yielded the highest ductility in both directions after the final pass. The ductility values decreased from around 60% to 25% for route A while they ranged between 10% and 20% for the other routes.

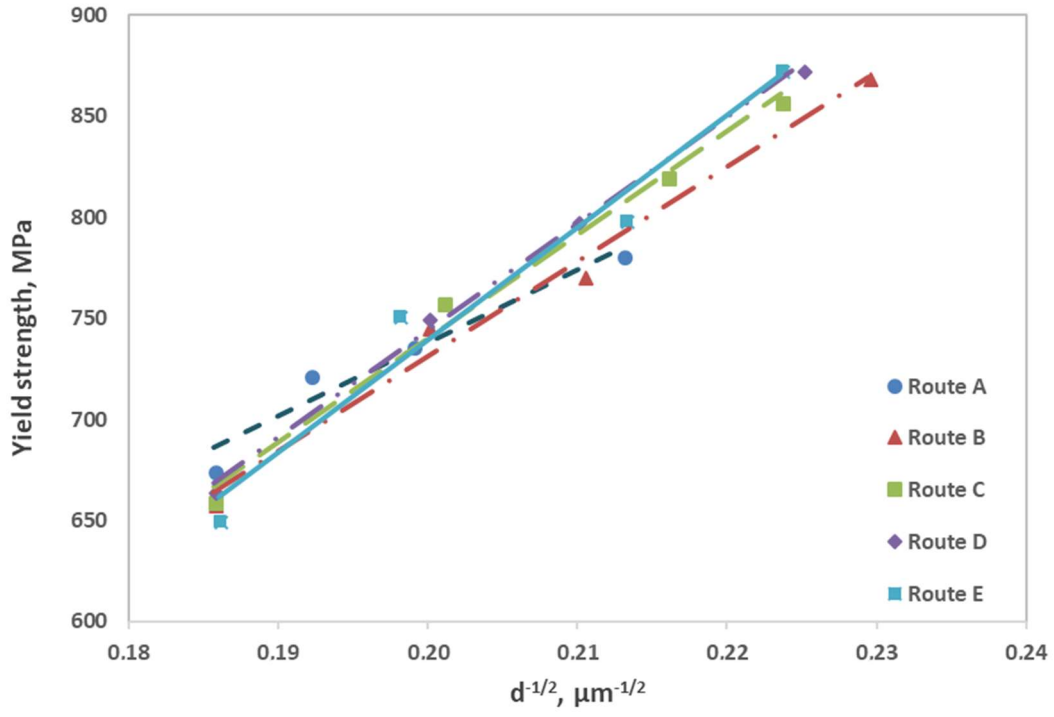

Figure 3.2.2: Hall-Petch relationship for all the routes of AISI 304

The relationship between grain size and yield strength can be verified using the Hall-Petch equation [117, 118]. According to the graphs in Figure 3.2.2, the average Hall-Petch constant (k) is calculated to be nearly 4600 MPa.$m^{1/2}$, which is greater than that is in the previous papers [119, 120]. The dislocation density created due to plastic deformation along with the existence of mechanical twins mainly contributes to this discrepancy. In addition, as the grain refinement rate is relatively low for CGP method, applicability of Hall-Petch is limited for the materials in this study.

Mechanical behavior of the samples strained along two in-plane perpendicular directions revealed the existence of flow anisotropy with varying degree depending on the route and pass number. Strain path-stimulated texture can be cited as the source of anisotropy, since morphology and grain size do not display substantial variation with route [121]. Tensile strength after the whole process along TD is greater than that along LD on all routes but E. There are three passes in which the groove edges are parallel to LD of the sheet for this route. Therefore, number of passes along a specific direction plays an important role on the directional strength.

Strength anisotropy of route A is quite high when compared to the other routes as demonstrated in Figure 3.2.1. Rotation between the passes reduces anisotropy due to a more uniform distribution of the bending and stretching regions, where SPD takes place and the greatest tendency for micro-cracking is expected [60]. From this standpoint, route B is promising in terms of isotropy due to successive rotations between passes. Similar mechanical behavior of routes B and D indicates that pass order has almost no effect on anisotropy. On the contrary, a higher rate of anisotropy is observed for routes C and E. Thus, a processing schedule containing equal number of passes along different directions can be followed to provide isotropic properties.

Strain hardening and grain refinement yield more strengthening during the first passes as compared with the subsequent passes. A reduction is recorded for some routes during the following passes, as a result of the mechanisms of micro-cracking and flow softening which is related to dislocation annihilation at higher dislocation densities through dynamic recovery mechanisms [60, 98, 122]. On the other hand, no decrease in hardness was observed after each pass despite the increase between the passes was smaller after the initial pass. Therefore, it can be inferred that micro-cracking is more effective than flow softening in the reduction of strength [59]. The fact that strength does not show a monotonic change with increasing pass number in routes A and C points to the more likely occurance of micro-cracks in these routes. Elastic moduli of CGPed samples are also decreased for many conditions as seen in Figure 3.2.1, since grain boundary regions are volumetrically increased during processing and non-equilibrium grain boundaries are rearranged to relatively equilibrium boundaries together with stress relaxation [99, 100]. This is also demonstrated by the increase of the ductility after some consequent passes.

Influence of processing route on the mechanical properties was explored via hardness experiments, too. Property variation along the central line of the samples was revealed particularly. Moreover, inhomogeneity factors were calculated for a quantitative expression of the distribution using the following expression [123, 124]:

$$\text{I. F.} = \frac{\sqrt{(\sum_{i=1}^{n}(H_i-\bar{H})^2)/(n-1)}}{\bar{H}} \times 100 \qquad (8)$$

where n is the total number of measurements, $\bar{H}$ is the average hardness, and H_i is the magnitude of each hardness measurement.

The highest improvement in hardness has been recorded for the first pass with a rate of 60% over the as-received condition. Irrespective of the route, the average hardness improvement was over two-folds after the fourth pass (Figure 3.2.3.a-e).

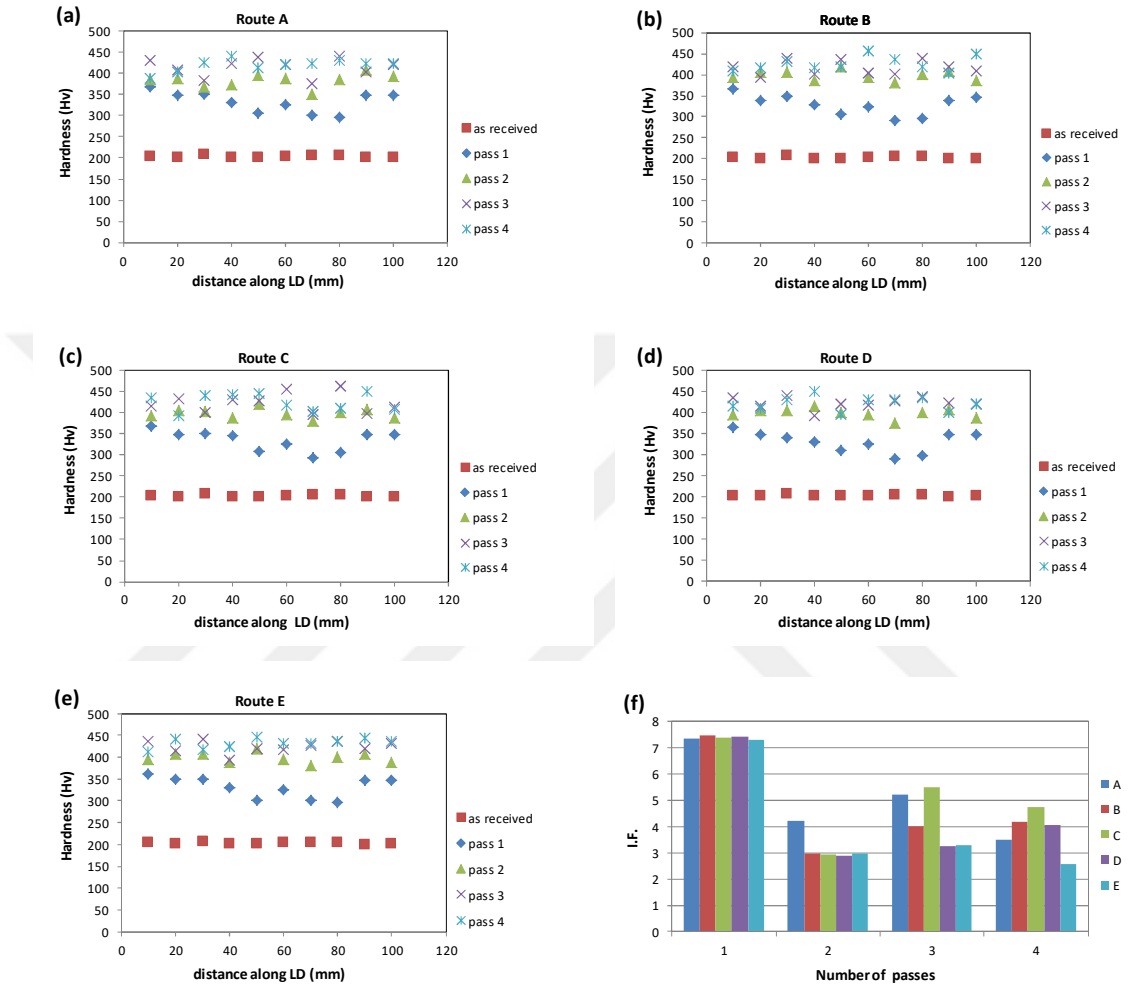

Figure 3.2.3: (a), (b), (c), (d) and (e) Hardness profiles of the CGPed stainless steel samples of all the routes along the longitudinal distances, (f) The inhomogeneity factor for all the routes versus pass numbers

Inhomogeneity factors for the first passes are more or less the same as seen in Figure 3.2.3(f), which is predictable as these passes are identical for all routes. A similar result is anticipated for the second passes of all the routes except route A, which has no rotation between passes. It can be interpreted that pass order has almost no effect on

homogeneity along a specific direction by considering the small inhomogeneity difference between routes B and D having different pass sequences. The greatest difference of uniformity is between routes C and E as expected. First two passes are the same for these routes, but regarding the groove edge orientation, the last two passes of route C are along TD while they are in LD for route E. This results in a higher non-uniformity along LD for route C, and a more uniform deformation for route E [60, 111]. In addition, unlike other routes, regional bending for all the passes along LD is prevalent for route A. As a consequence, route A should have the greatest inhomogeneity. However, alternating deformation field, in which dislocation generation rate changes over multiple pressing cycles, inhibits this drawback [60]. Strength and ductility profiles of the routes are summarized in Figure 3.2.4.

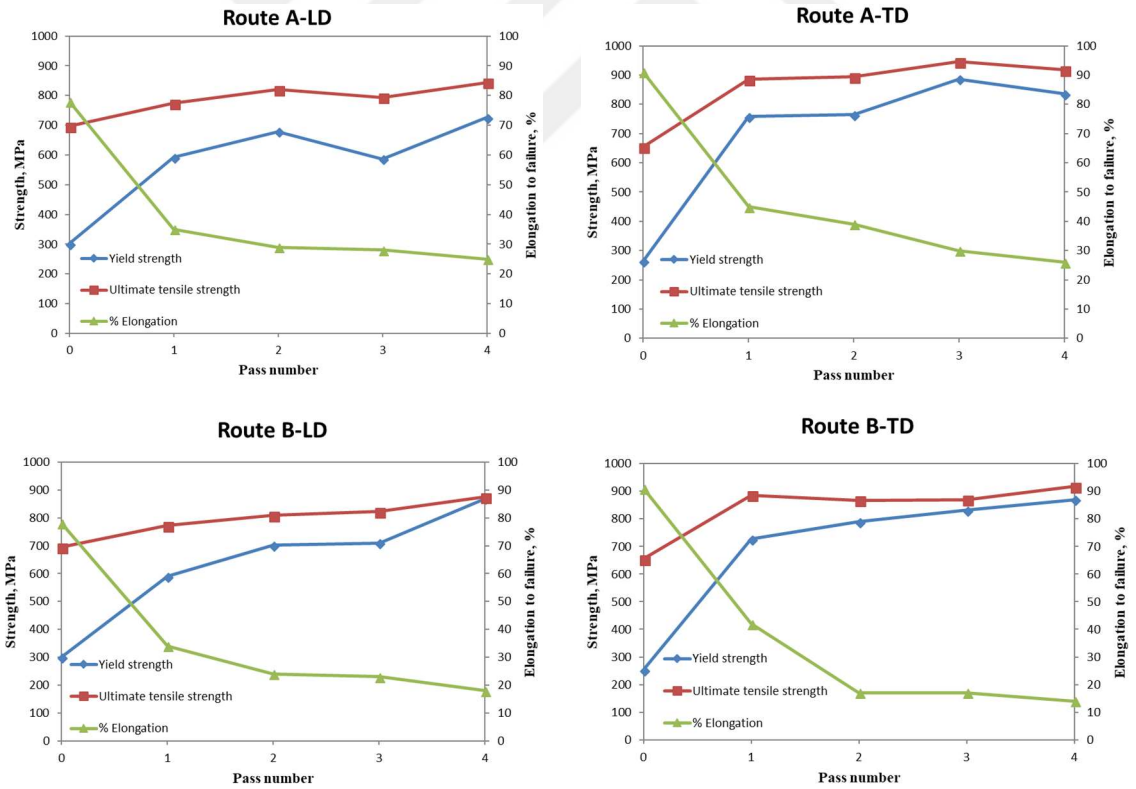

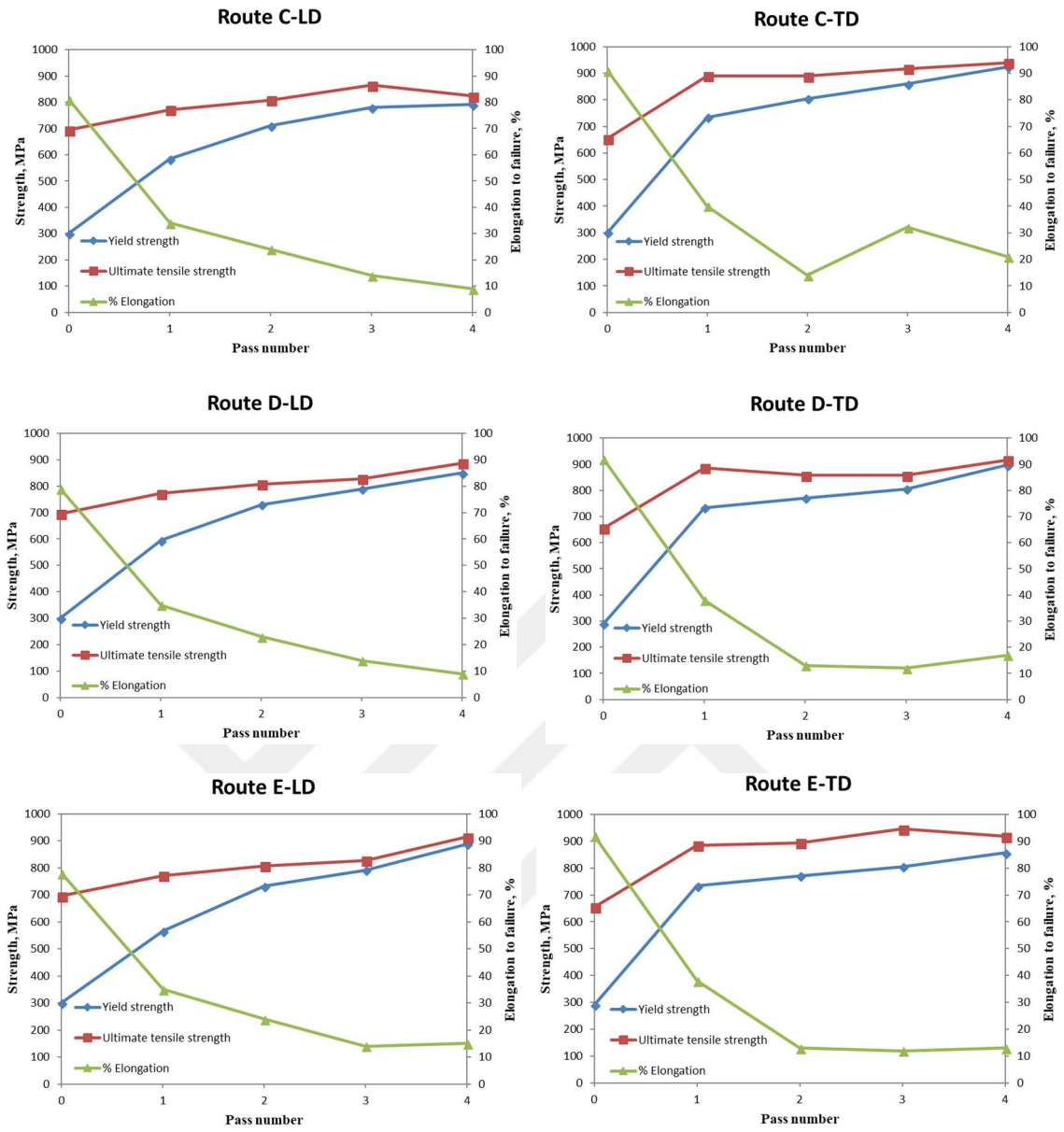

Figure 3.2.4: Strength and ductility profiles with respect to pass number along (a) longitudinal direction and (b) transverse direction

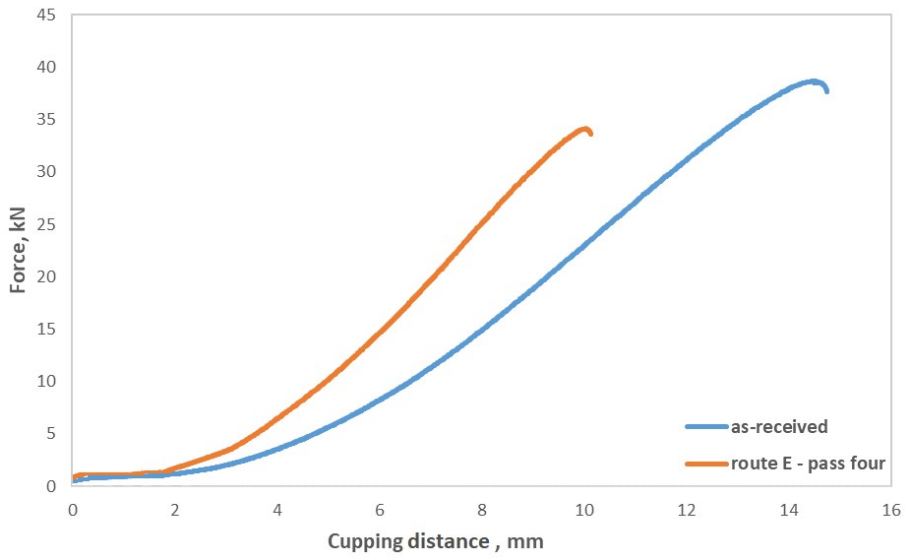

Figure 3.2.5: Force-cupping curves of steel samples: (a) as-received, (b) after fourth pass of route E

Erichsen test has been conducted to explore the formability of the material. One sample from the as-received material, and another sample after the last pass of route E has been cut in the form of square. Force-cupping diagrams are shown in Figure 3.2.5. Cupping force corresponding to the same cupping distance is higher for the CGPed sample indicating that the thinning will be smaller when formed [57, 78-83]. Despite the reduction of ductility due to CGP, it has also a good cupping distance.

In Figure 3.2.6, the shape of the samples after erichsen test are shown. The one on the left belongs to the as-received sample while the one on the right is the final form of the sample after fourth pass of route E. The fracture of the as-received sample is catastrophic as compared to the CGPed sample. In the processed sample, some regions might have been weakened due to microcracks and thinning of these regions was more probable.

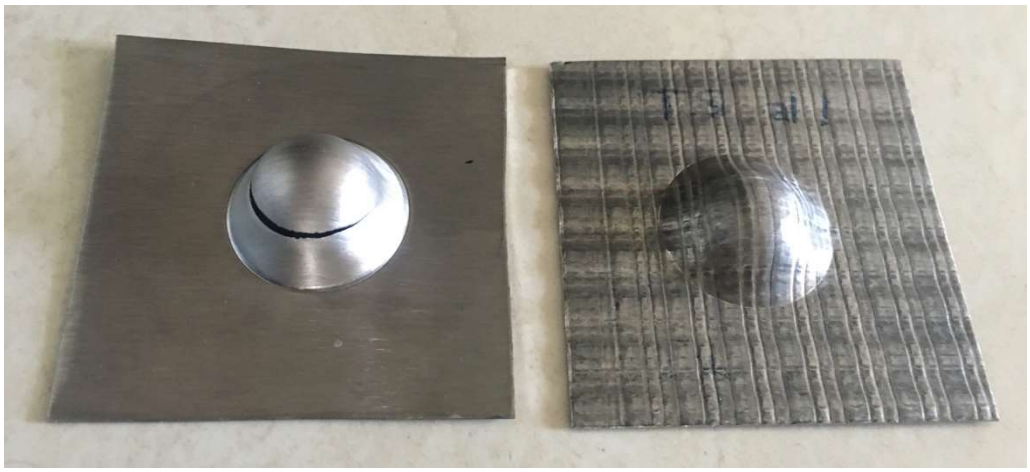

Figure 3.2.6: Samples formed after erichsen tests

Three tensile test specimens from different regions of the last routes of processed three AISI 304 stainless steel samples were tested to check the repeatability. The best conditions were selected for these tests, and the resulting graphs are presented in Figure 3.2.7. Ultimate tensile strength values are slightly different for route B in TD, but the only difference is fracture strain when all the repetability samples are considered. This result is expectable, since the fracture is in the non-uniform deformation region.

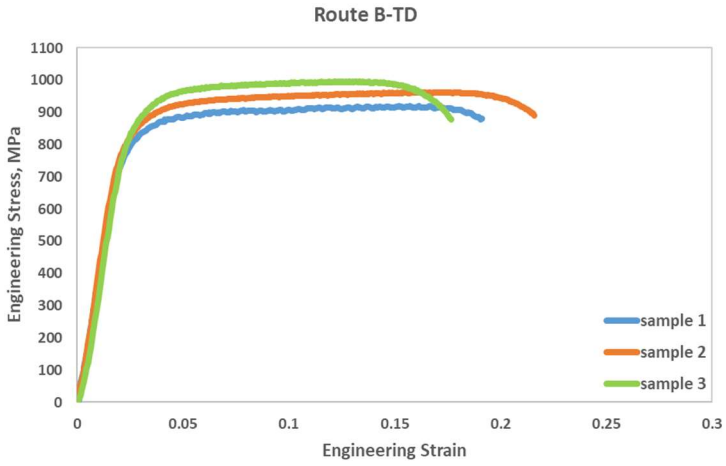

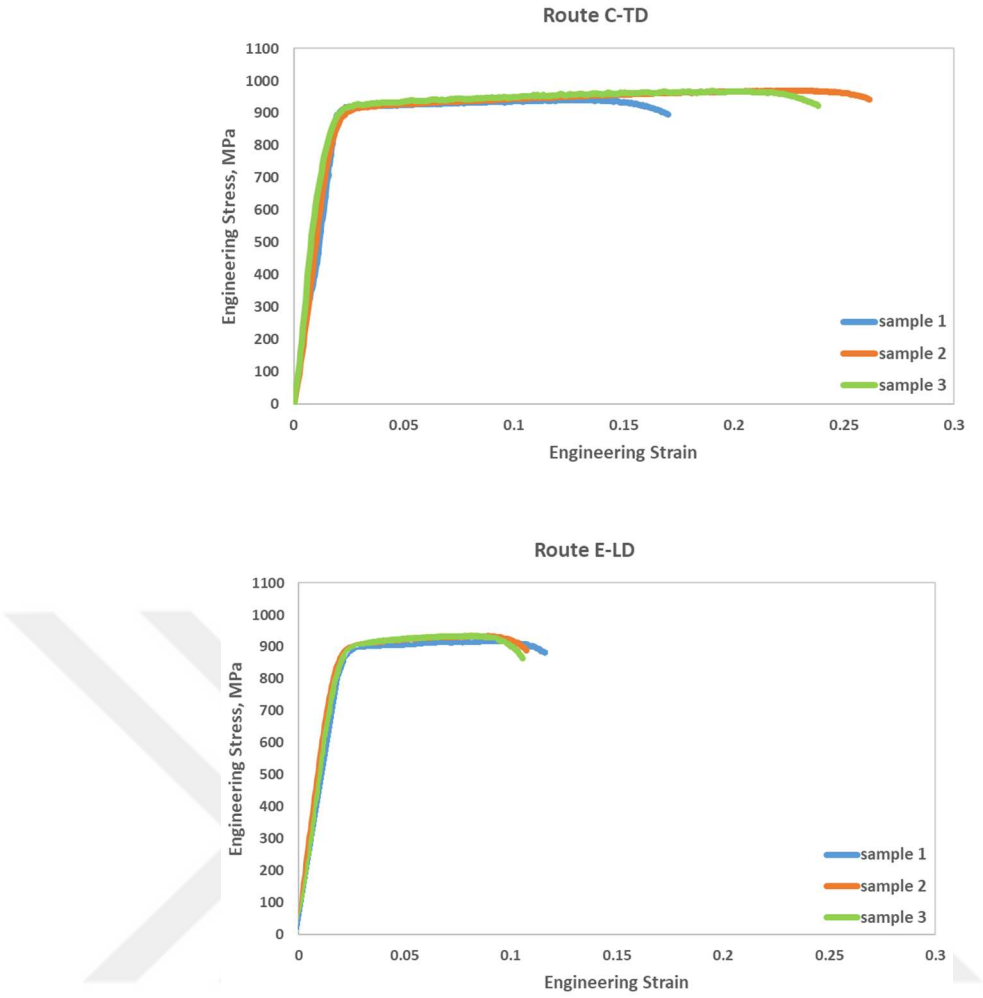

Figure 3.2.7: Repeatability test results of AISI 304 stainless steel samples from (a) route B along TD, (b) route C along TD, (c) route E along LD

CHAPTER IV

RESULTS & DISCUSSIONS ON Ti-15V-3Cr-3Sn-3Al

Microstructural properties and mechanical behavior results for Ti-15V-3Cr-3Sn-3Al will be demonstrated in this section.

4.1. Microstructural Evolution

Mean grain size of the as-received beta titanium alloy was measured as 107 microns via optical microscopy. A considerable refinement was not recorded as seen in Fig 4.1.1. Average grain sizes, which are in the range of 90-95 μm, are similar after the initial and final passes.

Any mechanical twin was not observed after deformation processes. Figs. 4.1.1(b) via 4.1.1(g) depict the microstructures briefly. They show that:

1. The rate of grain refinement decreases with the increase in imposed strain during CGP as indicated in other SPD methods [113-116]

2. Grain refinement effectiveness of CGP is lower relative to other SPD techniques, as it imposes a simple deformation field where slip during groove pressing is cancelled out by reverse slip during straightening [60].

3. Strain path is not very influential for beta-Ti in influencing the grain size after processing.

4. Due to the adjusted pressing stroke amount, no crack was observed in routes.

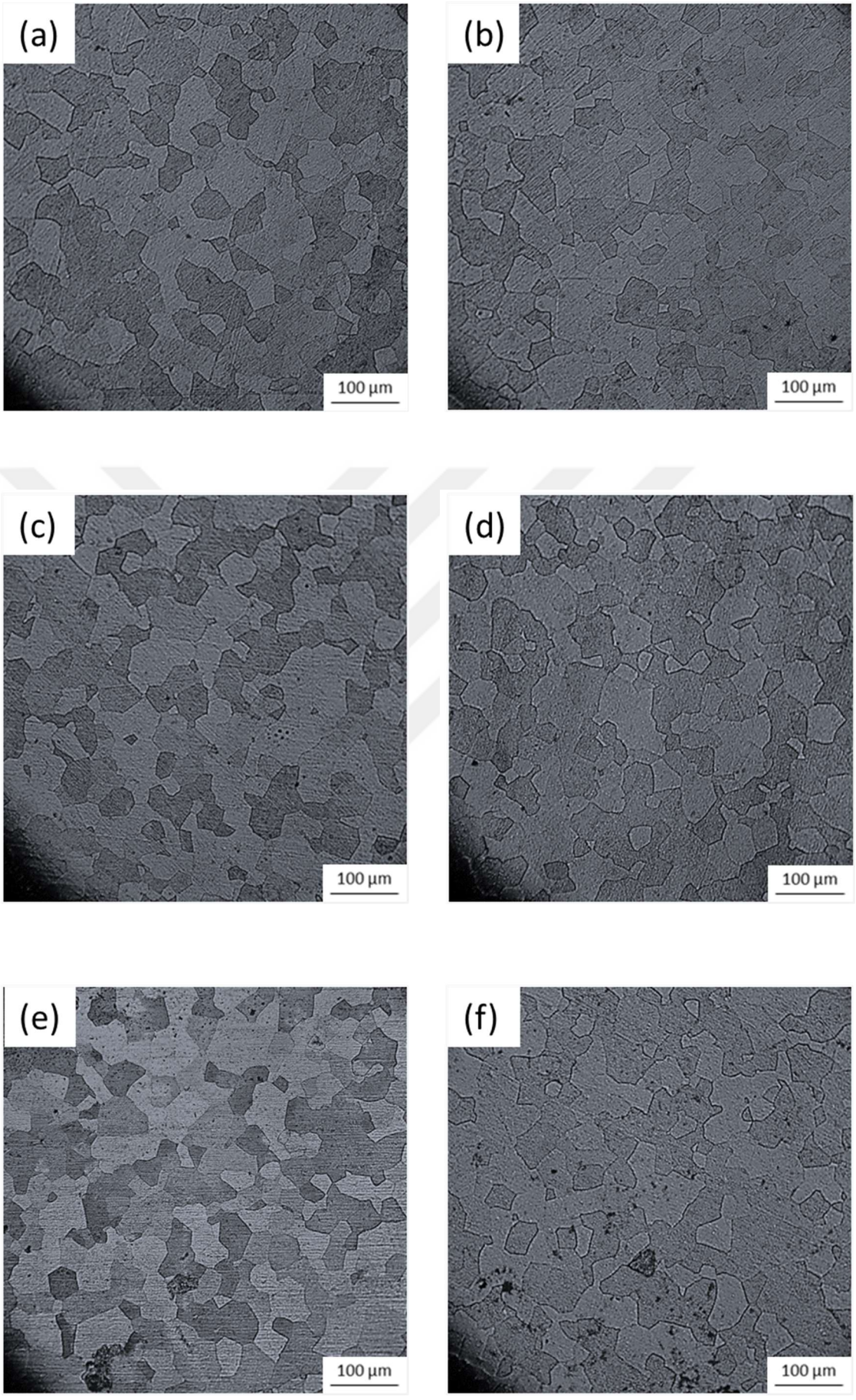
(a)
100 µm
(b)
100 µm
(c)
100 µm
(d)
100 µm
(e)
100 µm
(f)
100 µm

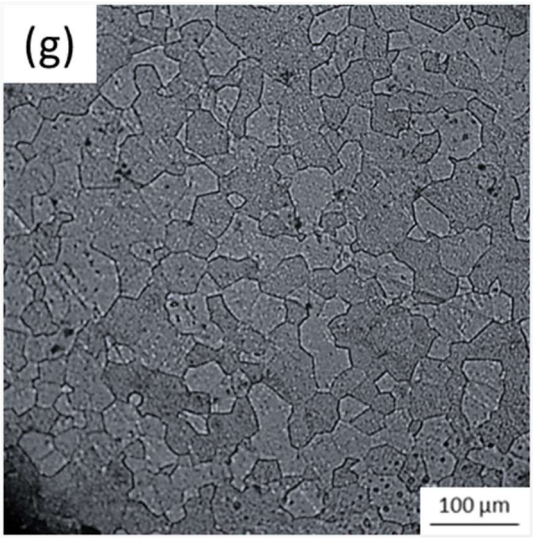

Figure 4.1.1: Grain structure of β-Ti: (a) annealed; (b) after 1 pass; (c) after 4 pass of the route A; (d) after 4 pass of the route B; (e) after 4 pass of the route C; (f) after 4 pass of the route D; (g) after 4 pass of the route E

4.2. Mechanical Behavior

The tensile curves of Ti-15V-3Cr-3Sn-3Al along both longitudinal and transverse directions are demonstrated in Figure 4.2.1. Ultimate tensile strength of the samples increased significantly after the initial pass, and almost stabilized for most of the conditions afterwards. Ductility values decreased a little while yield strength values fluctuated throughout the deformation process.

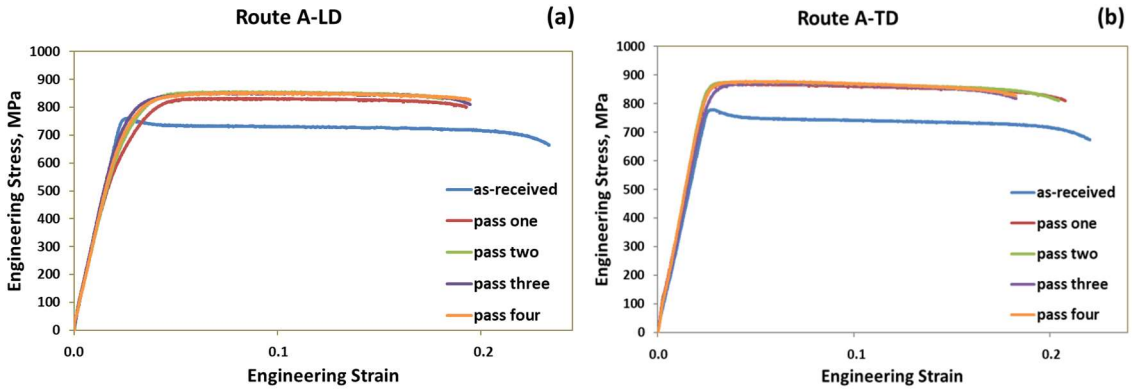

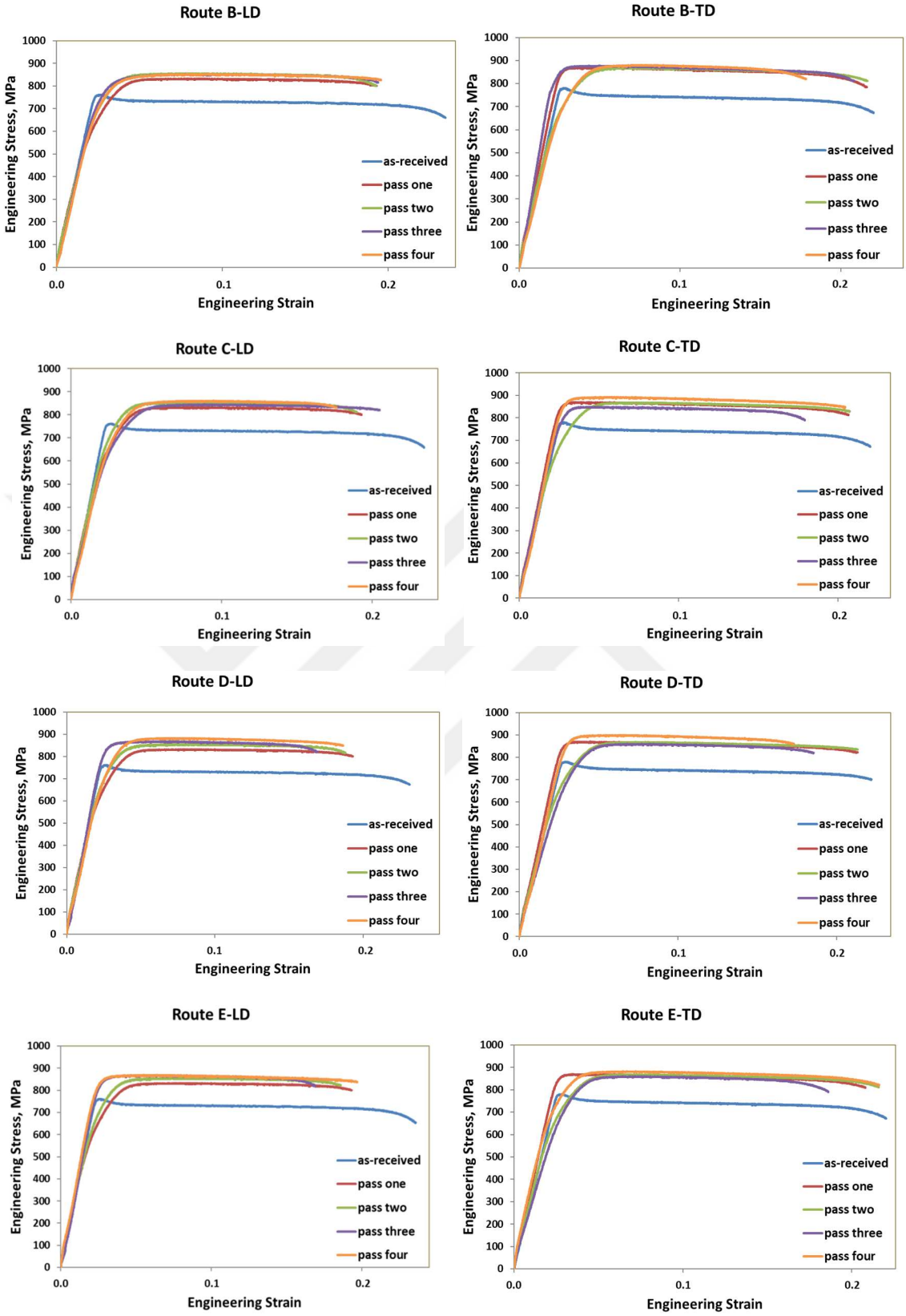

Figure 4.2.1: Stress-strain curves of β-Ti samples along (a) longitudinal direction and (b) transverse direction

The highest strength improvement is about 16%, occurring in LD for route D and E while it is nearly 15% in TD belonging to route C and D. Route A and B have the best ductility value, which is around %20 along LD after the last pass. Route E has a ductility value of %19, which is the best one in TD. Unlike the other two metals in this study, as-received β-Ti shows a bump after yield point. The reason for this behavior is that more stress is required for a material to start plastic deformation provided the dislocation density is low [125]. This bump is eliminated while the yield strength of the as-received material decreases with the increasing dislocations during deformation. Tensile strength after the whole deformation along TD is slightly higher than that along LD on all routes. For all the routes, the number of passes in which transverse direction of the sample is parallel to the groove edges is higher or equal to the number of passes in which it is perpendicular to the groove edges except route E. Specifically, number of passes along a specific direction plays a minor role on the directional strength.

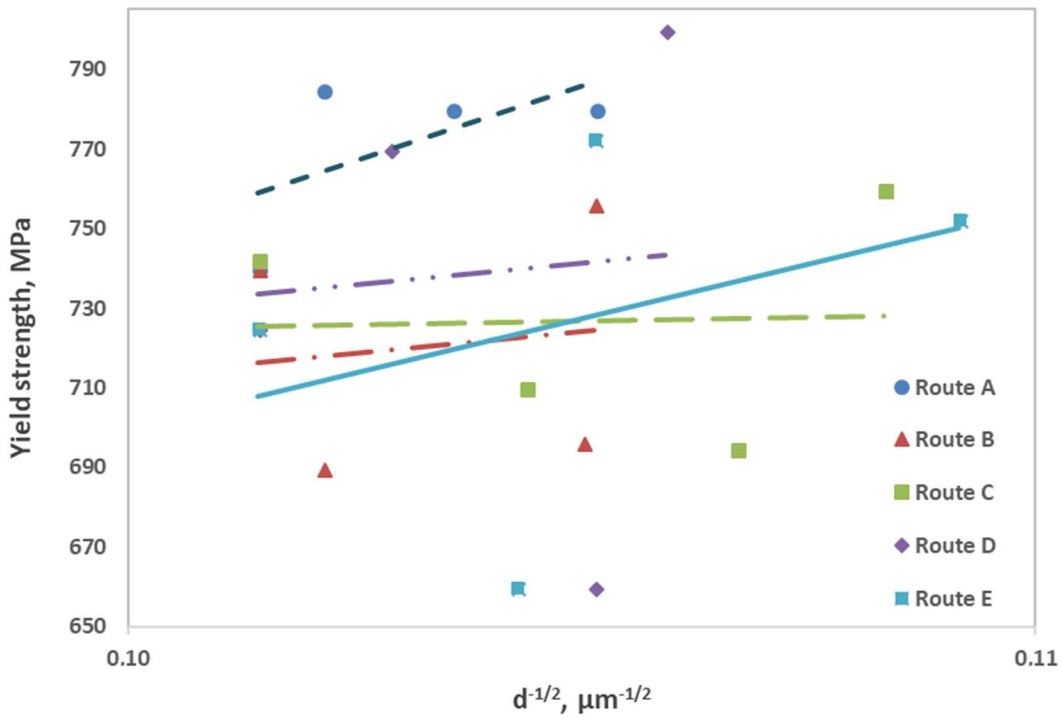

Figure 4.2.2: Hall-Petch relationship for all the routes of beta Ti

The correlation between grain size and yield strength can be checked using the Hall-Petch equation [117, 118]. Due to the graphs in Figure 4.2.2, the constant (k) is calculated to be nearly 5068 MPa.$m^{1/2}$. The dislocation density created due to plastic deformation mainly contributes to this relatively high k value [126]. The points are distributed more irregularly in this graph as compared to others, since the yield strength values of this material were more irregular.

Strength anisotropy of routes are quite low as demonstrated in Figure 4.2.1. Similar behavior of routes B and D implies a minor influence of pass order upon anisotropy. Moreover, a similar degree of anisotropy is observed for routes C and E. As a result, a processing schedule containing a sequence of passes with the same or varying directions make almost no difference on isotropic properties of β-Ti having BCC lattice structure.

Strain hardening and grain refinement generally cause more strengthening during the initial passes. A decrease is seen for some routes during the following passes, due to micro-cracking and flow softening, which is in connection with dislocation annihilation at higher dislocation densities by means of dynamic recovery mechanisms [60, 98, 122]. Furthermore, a decrease in hardness was also observed for some passes although the variation of hardness values between the passes was smaller after the first pass. It can be deduced that micro-cracking is less effective than flow softening in the reduction of strength [59]. As seen in Figure 4.2.1, elastic moduli of some CGPed samples are decreased. The reason for the decrease is that grain boundary locations are volumetrically rise during processing and non-equilibrium grain boundaries are rearranged to relatively equilibrium boundaries together with stress relaxation [99, 100]. The increase of the ductility after some consequent passes also demonstrates this.

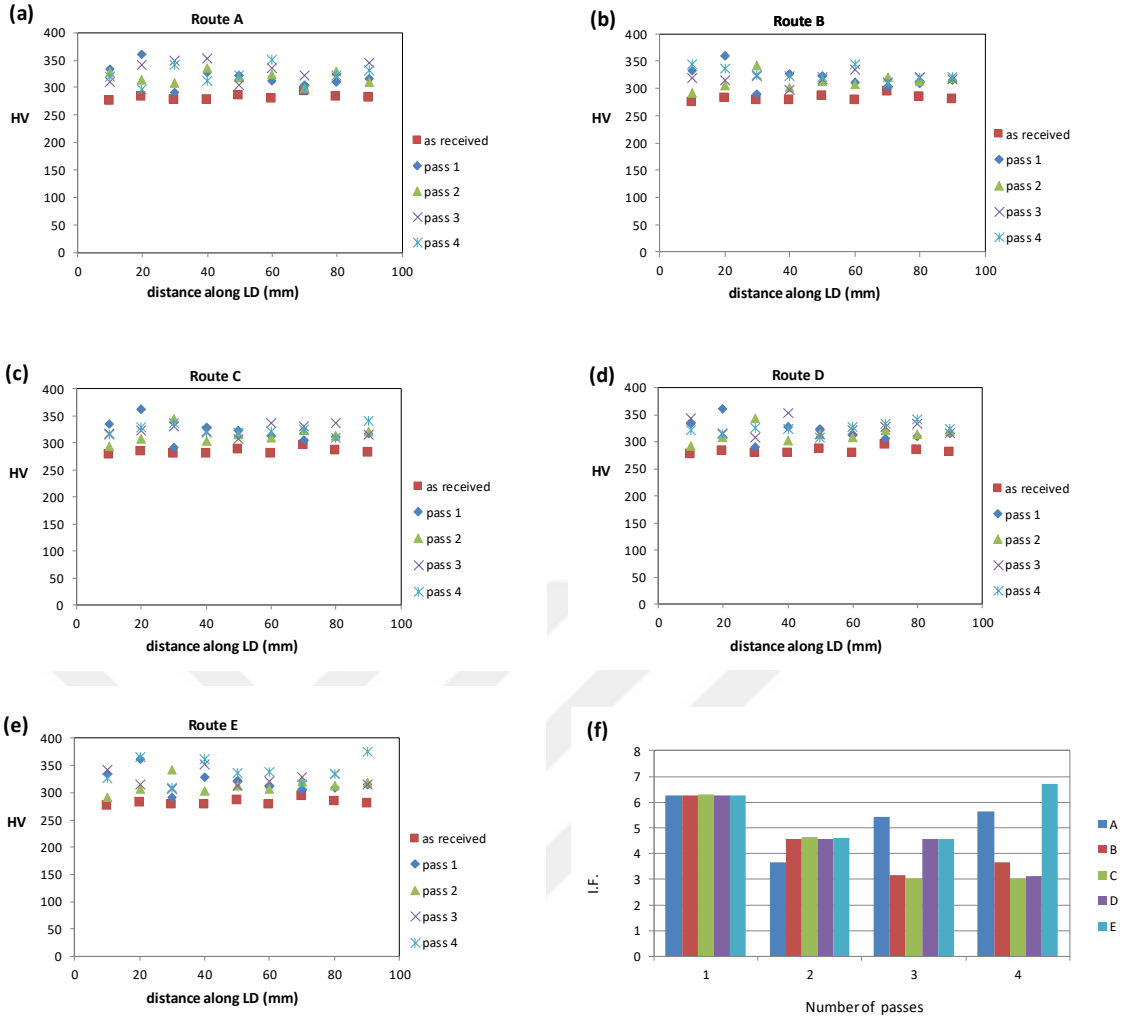

Figure 4.2.3: (a), (b), (c), (d) and (e) Hardness profiles of the CGPed β-Ti samples of all the routes along the longitudinal distances, (f) The inhomogeneity factor for all the routes versus pass numbers

Influence of the routes on the mechanical properties was also investigated through hardness tests. Hardness measurements showed the property variation in the central line of the samples. Inhomogeneity factors were also calculated for all routes according to the formula shown in the previous sections [123, 124].

The highest hardness increase is achieved for the first pass with a rate of 14% over the as-received condition. The hardness improvement was about 20% after the fourth passes (Figure 4.2.3.a-e).

As demonstrated in Figure 4.2.3f, inhomogeneity factors for the first passes are very similar, because these are identical for all routes. A similar data is expected for the second passes of all the routes except A which is not rotated between passes. Inhomogeneity difference is small between routes B and D having different pass orders, implying that pass order has a small influence on homogeneity. The maximum homogeneity difference after the whole process is between routes C and E. First two passes are identical for these routes, but the last two passes of route C are along TD considering the groove edge orientation whereas they are in LD for route E. Unlike stainless steel and zinc samples, this induces a higher uniformity along LD for route C and a more non-uniform deformation for route E for titanium. This difference might stem from the different crystal structures of these materials. Strength and ductility profiles of the routes are summarized in Figure 4.2.4.

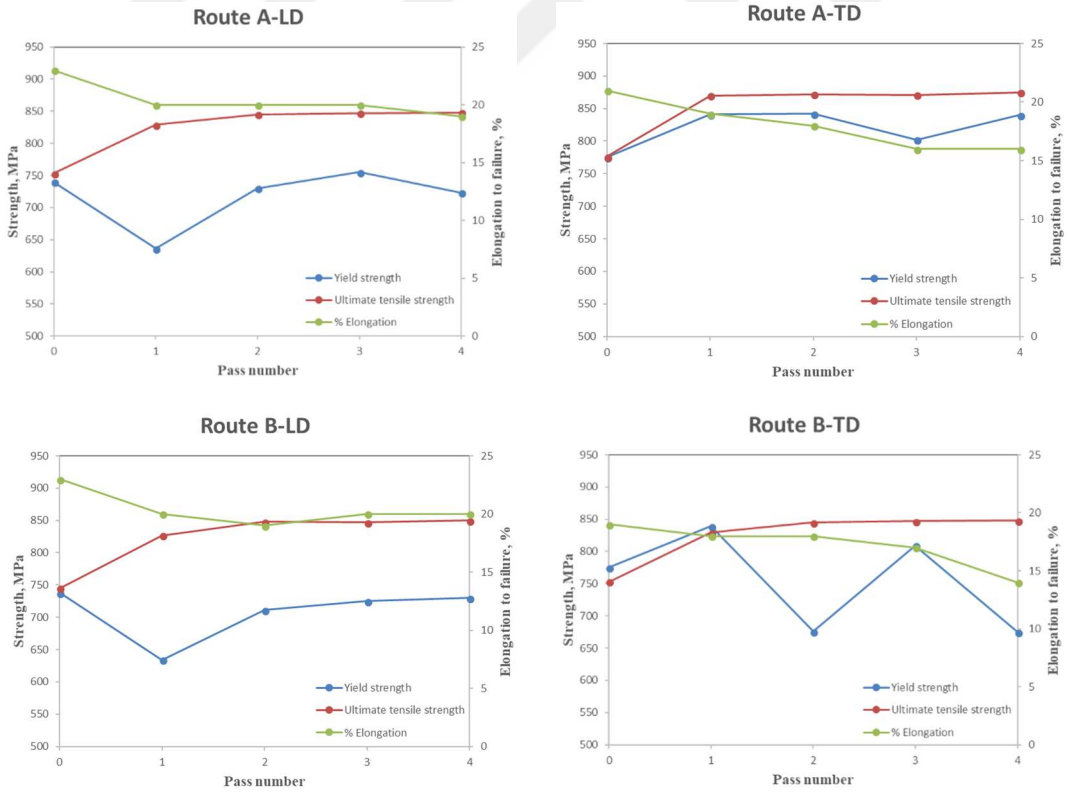

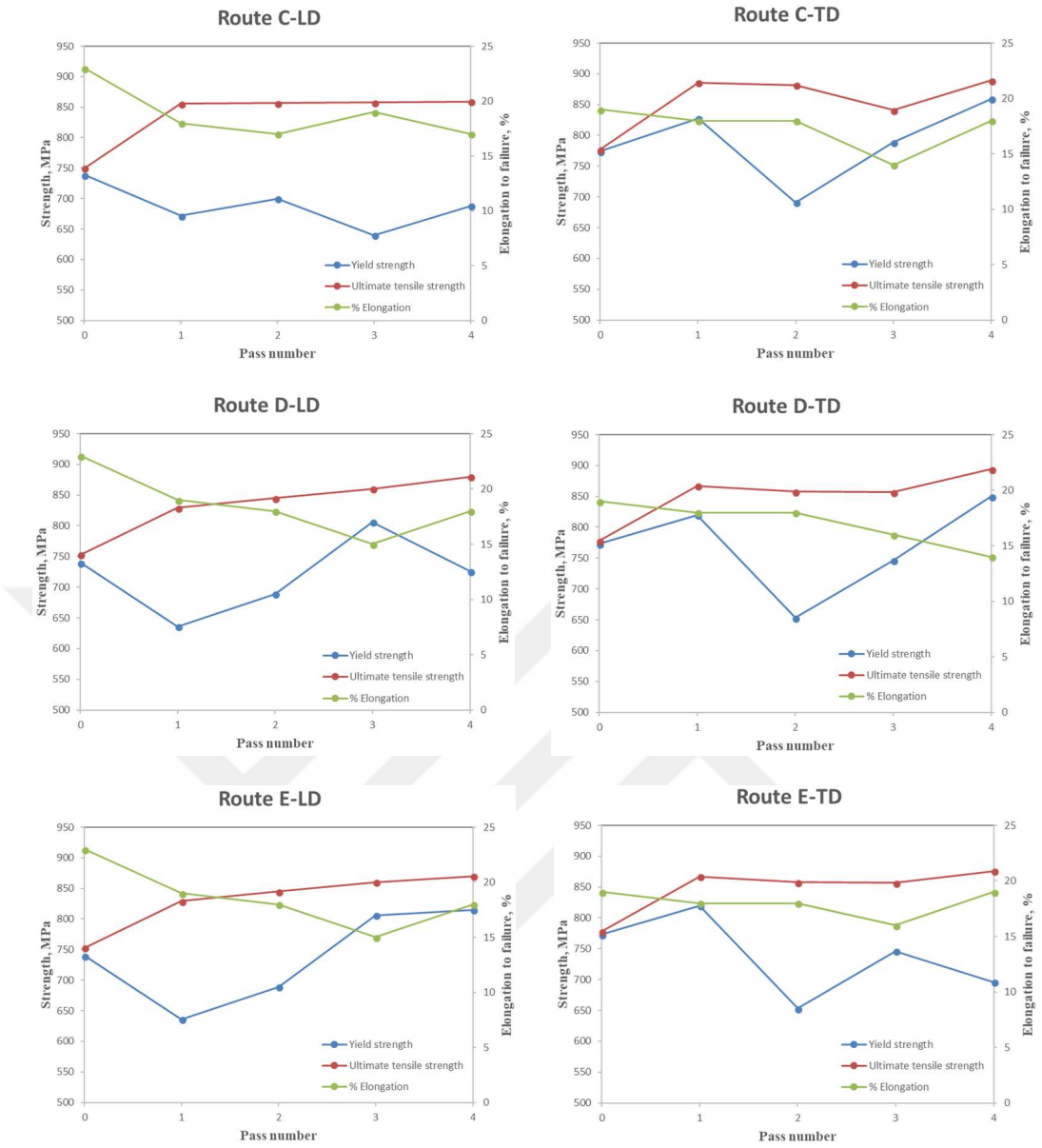

Figure 4.2.4: Strength and ductility profiles of β-Ti samples with increasing passes

Erichsen tests have also been applied on two β-Ti samples having square shape. One sample was selected from the as-received material and another sample after the last pass of route E. Force-cupping diagrams are as shown in Figure 4.2.5. These graphs are very close to each other since the ductility and strength values are not very different for these two conditions.

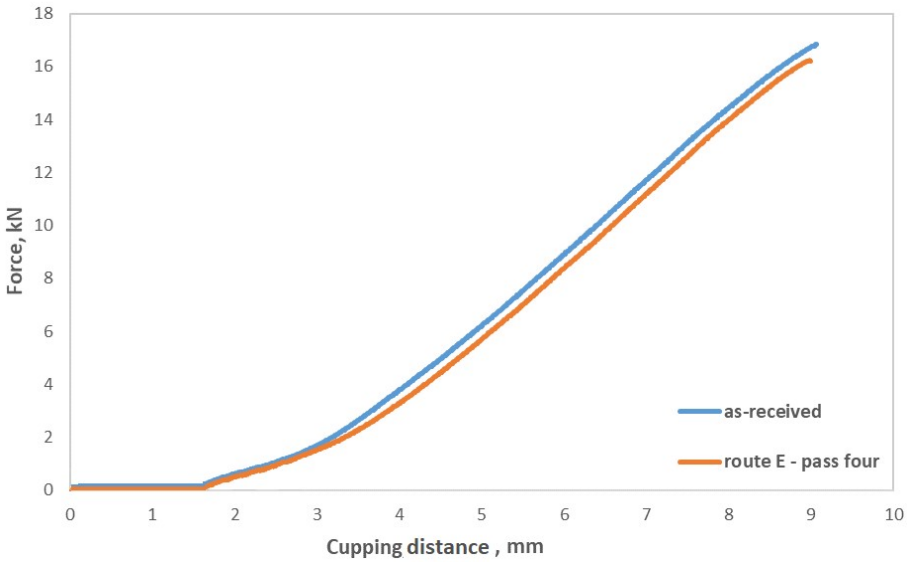

Figure 4.2.5: Force-cupping curves of β-Ti samples: (a) as-received, (b) after fourth pass of route E

In Figure 4.2.6, the shape of the samples after erichsen test are seen. The one on the left belongs to the as-received sample while the one on the right is the final form of the sample after fourth pass of route E. Both fracture profiles are very similar as can be anticipated from their force-cupping curves.

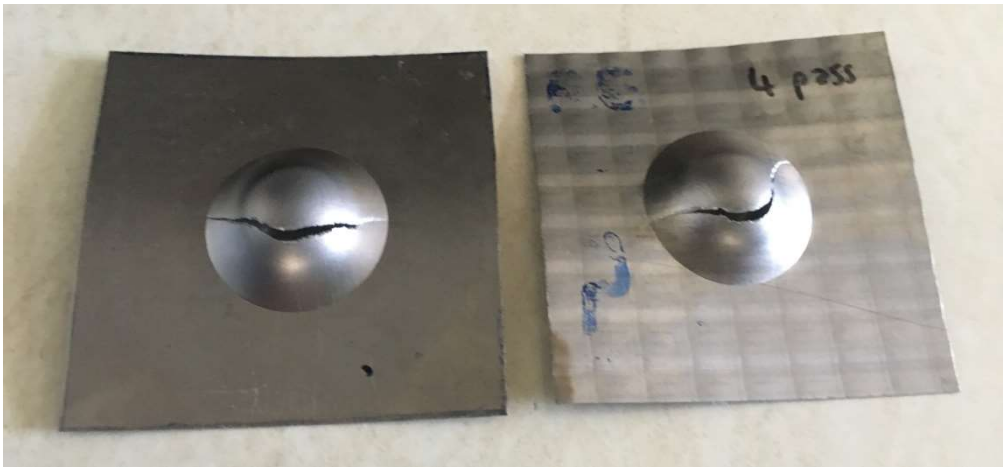

Figure 4.2.6: Samples formed after erichsen tests

Three tensile test specimens from different regions of the three β-Ti samples were tested to check the repeatability after the final passes. The best conditions were selected

for these tests and the resulting graphs are presented in Figure 4.2.7. The graphs of the samples belonging to three different routes are almost the same in itself.

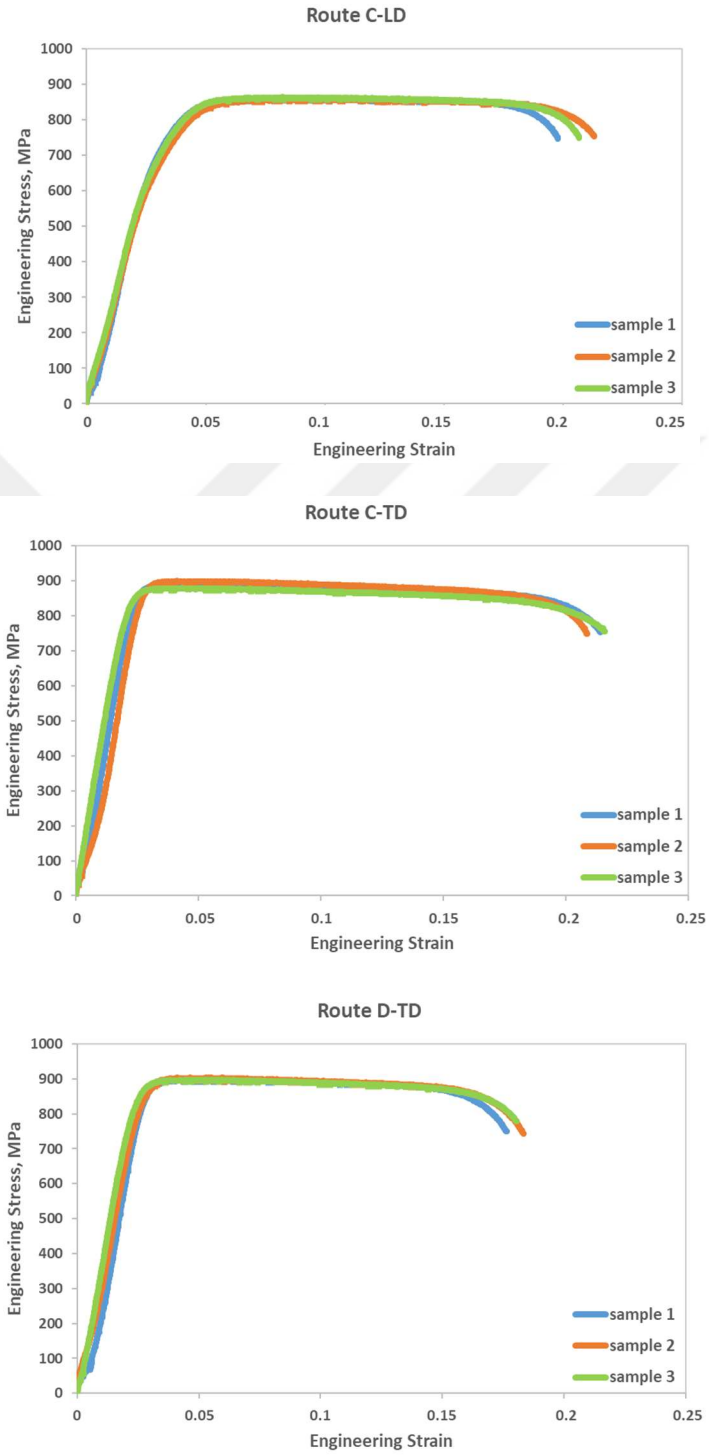

Figure 4.2.7: Repeatability test results of β-Ti samples from (a) route B along TD, (b) route C along TD, (c) route E along LD

CHAPTER V

RESULTS & DISCUSSIONS ON Commercially Pure Zinc

Microstructural observations and mechanical behavior results for commercially pure zinc will be discussed in this chapter.

5.1. Microstructural Evolution

According to the data taken from the microscopical image shown in Figure 5.1.1, average grain size of as-received pure zinc is approximately 117 μm. Grain size becomes 77 microns after the first pass. When the deformation process is considered as a whole, the final grain sizes of the routes A, B, C, D and E were recorded as 62, 74, 64, 68 and 71, respectively.

After the deformation processes, mechanical twinning activation has taken place. Figs. 5.1.1(b) via 5.1.1(g) show the microstructural evolution. They show that:

1. The rate of grain refinement decelerates with the increase in imposed strain during CGP as occured in other SPD methods [113-116].

2. Strain path is effective for pure zinc in dictating the grain size after processing. The best grain refinement ratio is around 47% belonging to route A and the lowest refinement is observed for route B, which is approximately 37%. Refinement rate of routes A and C are close to each other, while it is similar for routes B and D. Therefore, pass order has nearly no effect on grain size but pass number on a specific direction has.

3. The highest amount of twinning was observed in Route C. Twins are thinner for the routes A, C and D compared to the other routes after the

final pass. They are also rather thick and few in number after the first pass. Moreover, intensity of twins is relatively low for route E. Based on these observations, it can be inferred that there is a strong relationship between grain refinement and intensity and thickness of twins.

4. The twin size is restricted by the size of the grains, and in refined structures, shorter twins are observed [65].

5. Macroscopic fracture was not recorded in any route, under favour of the adjusted pressing stroke distance.

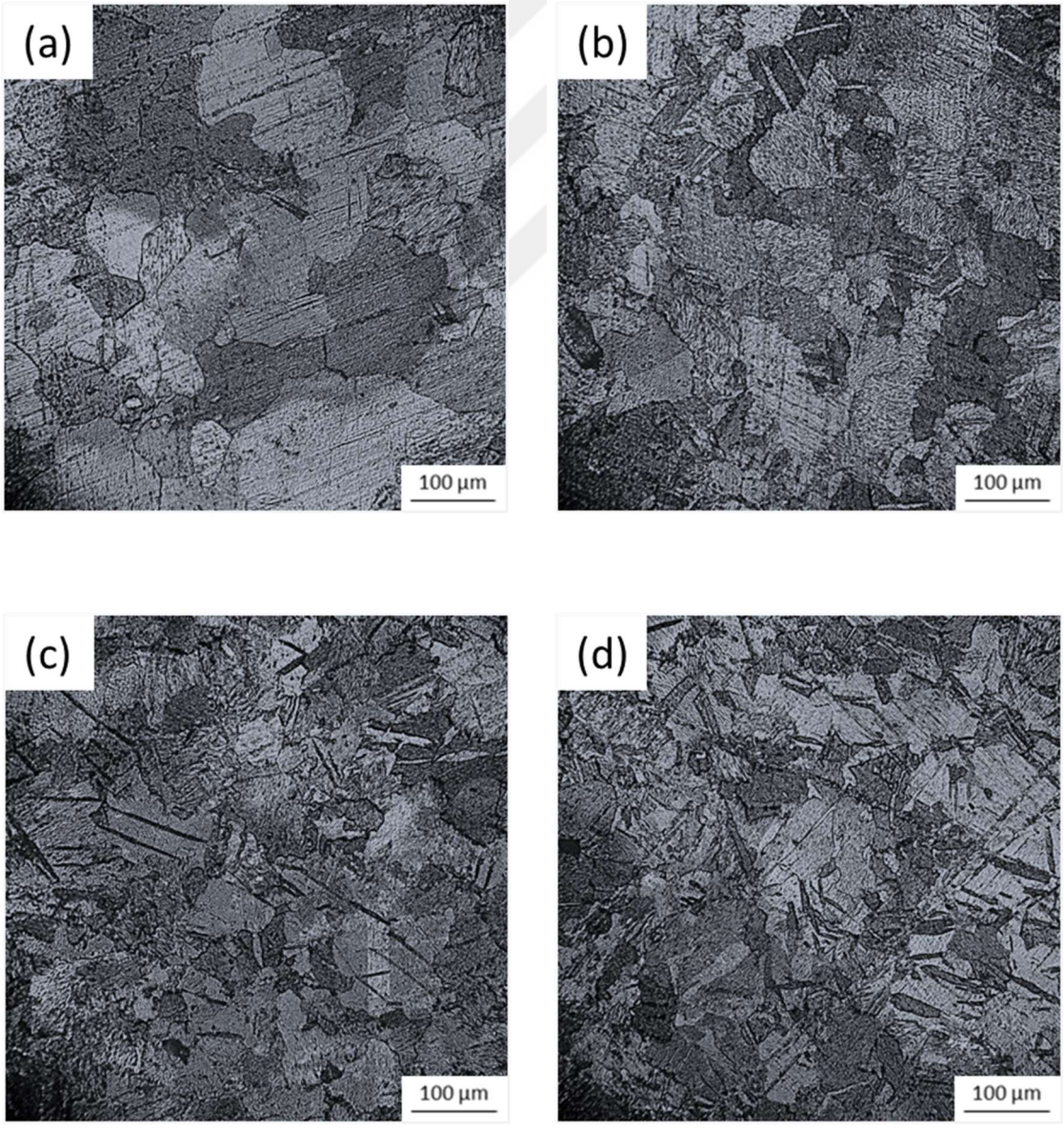

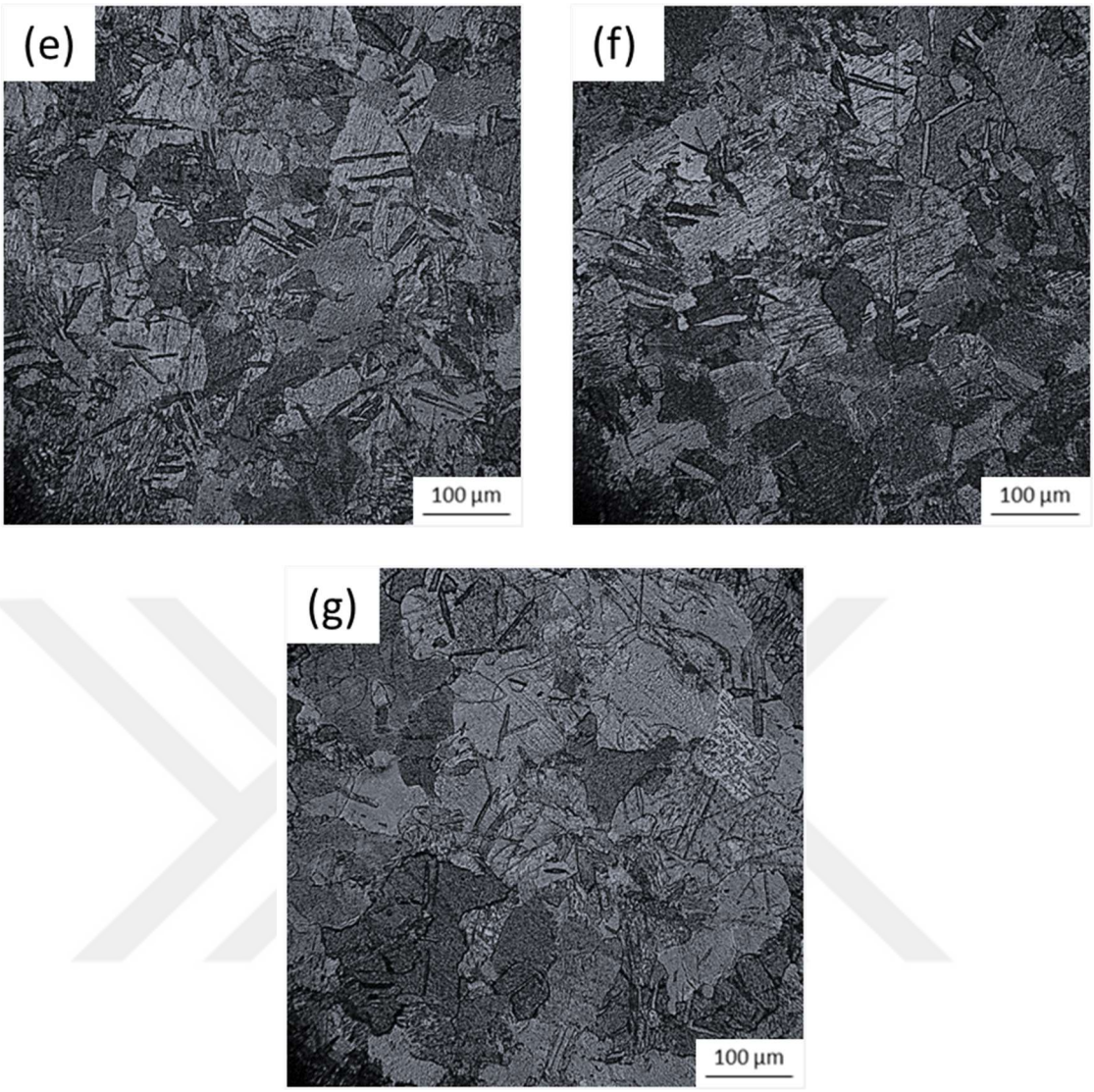

Figure 5.1.1: Grain structure of the commercially pure zinc: (a) annealed; (b) after 1 pass; (c) after 4 pass of the route A; (d) after 4 pass of the route B; (e) after 4 pass of the route C; (f) after 4 pass of the route D; (g) after 4 pass of the route E

5.2. Mechanical Behavior

In Figure 5.2.1, the stress-strain graphs of commercially pure zinc along both directions are represented. Strength is mostly improved for routes during the deformation processes. Yield strength values mostly increased for all routes, whereas ductility values mostly decreased.

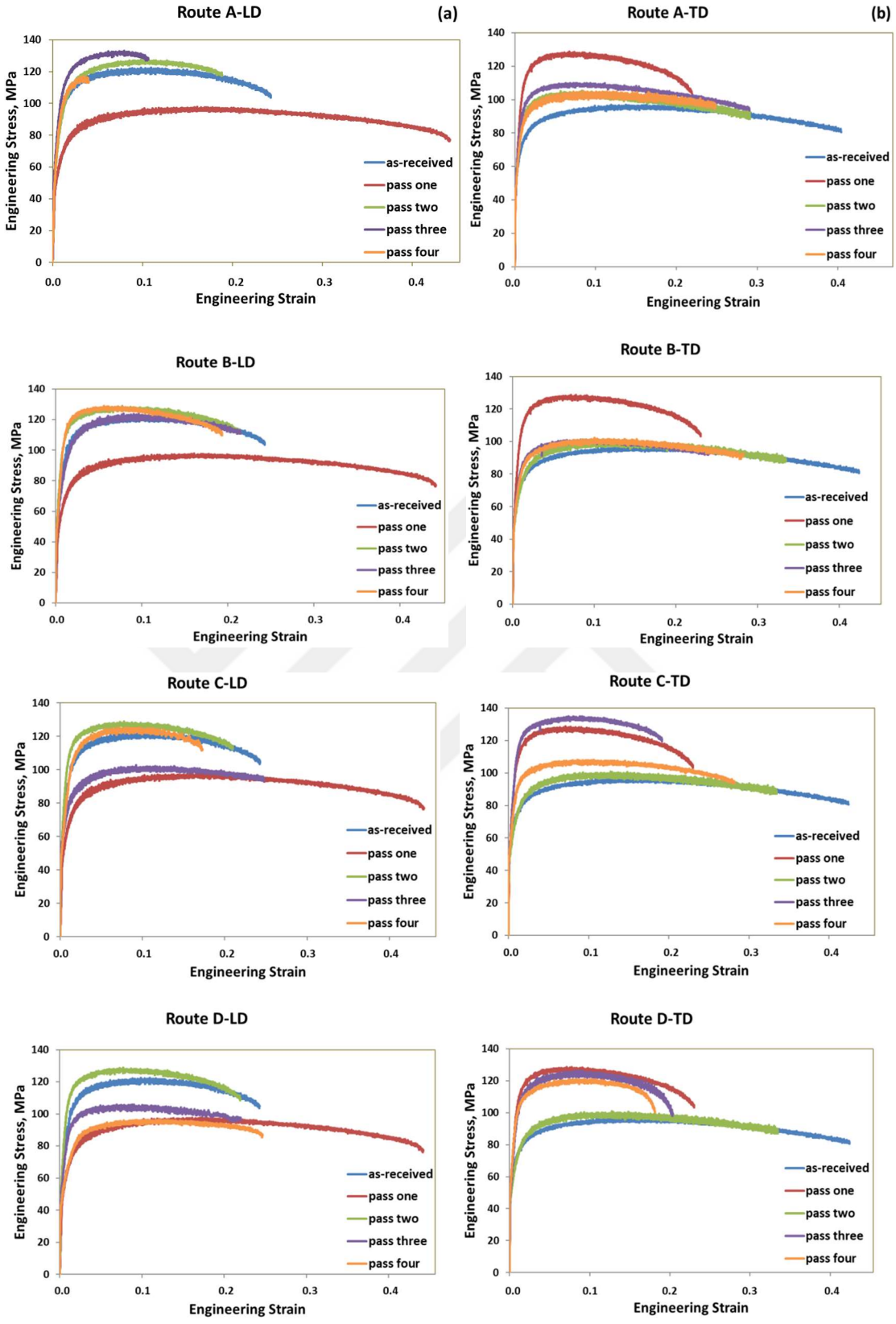
Route A-LD
(a)
Route A-TD
(b)
Route B-LD
Route B-TD
Route C-LD
Route C-TD
Route D-LD
Route D-TD
Engineering Stress, MPa
Engineering Strain
as-received
pass one
pass two
pass three
pass four

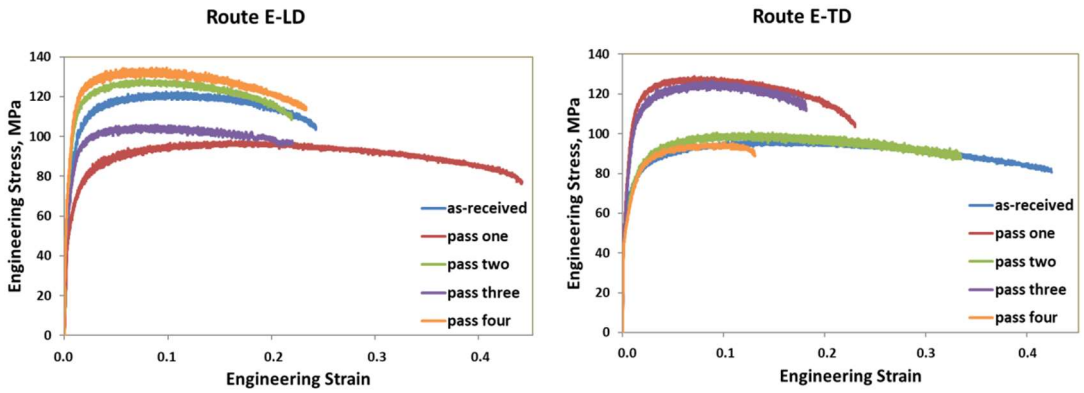

Figure 5.2.1: Stress-strain curves of commercially pure zinc samples along (a) longitudinal direction and (b) transverse direction

The best strength improvement is nearly 8%, and occurs in LD for route E compared to 28% in TD belonging to route D. As repeatedly mentioned in the previous parts, route E has three passes in which the groove edges are perpendicular to TD, and for route D, number of perpendicular and parallel passes are equal. Along LD, route D has yielded the highest ductility, which is nearly 24%, but along TD routes B and C have a ductility of about 27%, which is the highest after the whole process. Tensile and yield strengths along LD is greater than that along TD on all routes except D after CGP operation.

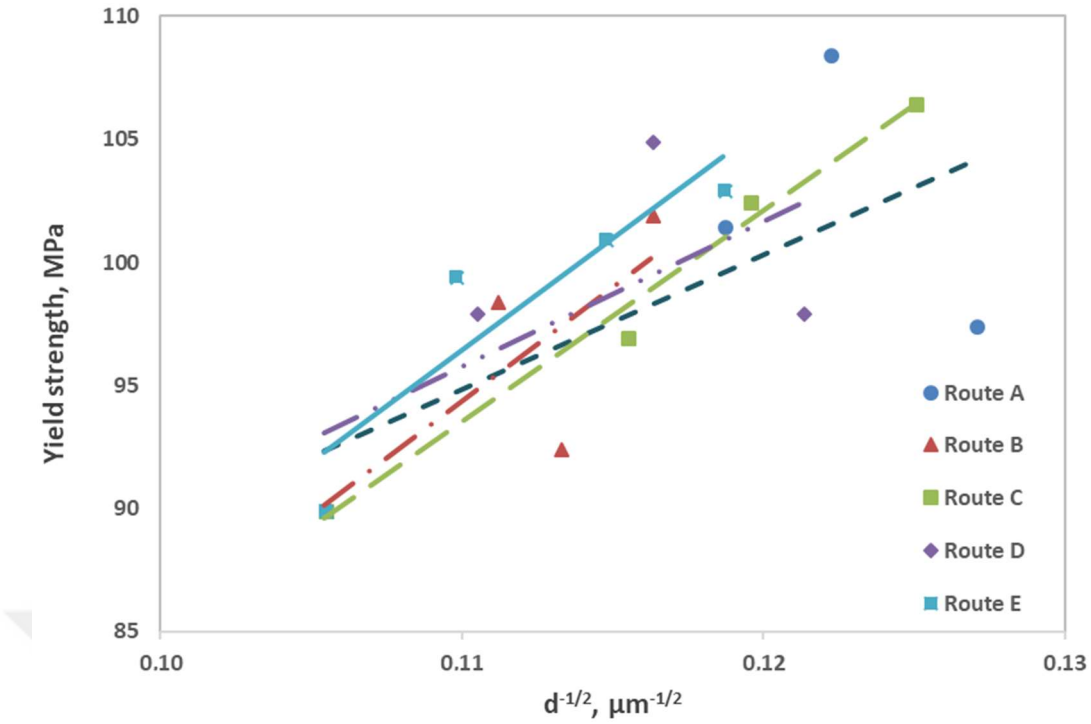

Figure 5.2.2: Hall-Petch relationship for all the routes of commercially pure Zn

Grain refinement and yield strength relationship of pure Zn can be verified through the Hall-Petch formula [117, 118]. The average Hall-Petch constant (k) is calculated as about 764 MPa.m$^{1/2}$ based on the lines in Figure 5.2.2. The existence of mechanical twins is the main reason of this high value.

As seen from the Figure 5.2.1, as-received material was rather anisotropic. In addition, mechanical behavior of the samples strained along two perpendicular directions on the same plane revealed the existence of flow anisotropy with varying degree depending on the route and pass number. After the first CGP passes, a decrease in strength and an increase in ductility is observed along LD in an unexpected way. Strain hardening and grain refinement yield more strengthening along TD during the first passes compared to the subsequent passes. Also, twinning causes strengthening and high work hardening since it behaves like the grain boundaries which hinders growing twins and slip [65]. A decrease in strength is recorded for many following passes, because of the mechanisms

of micro-cracking and flow softening which is related to dislocation annihilation at higher dislocation densities through dynamic recovery mechanisms [60, 98, 122]. These are the reasons also for the ductility increase observed along LD in the initial pass. Furthermore, elastic moduli of some CGPed pure zinc samples are reduced as seen in Figure 5.2.1. The reason of this behavior is that grain boundary locations are volumetrically rise during deformation and non-equilibrium grain boundaries are rearranged to comparatively equilibrium boundaries together with stress relaxation [99, 100].

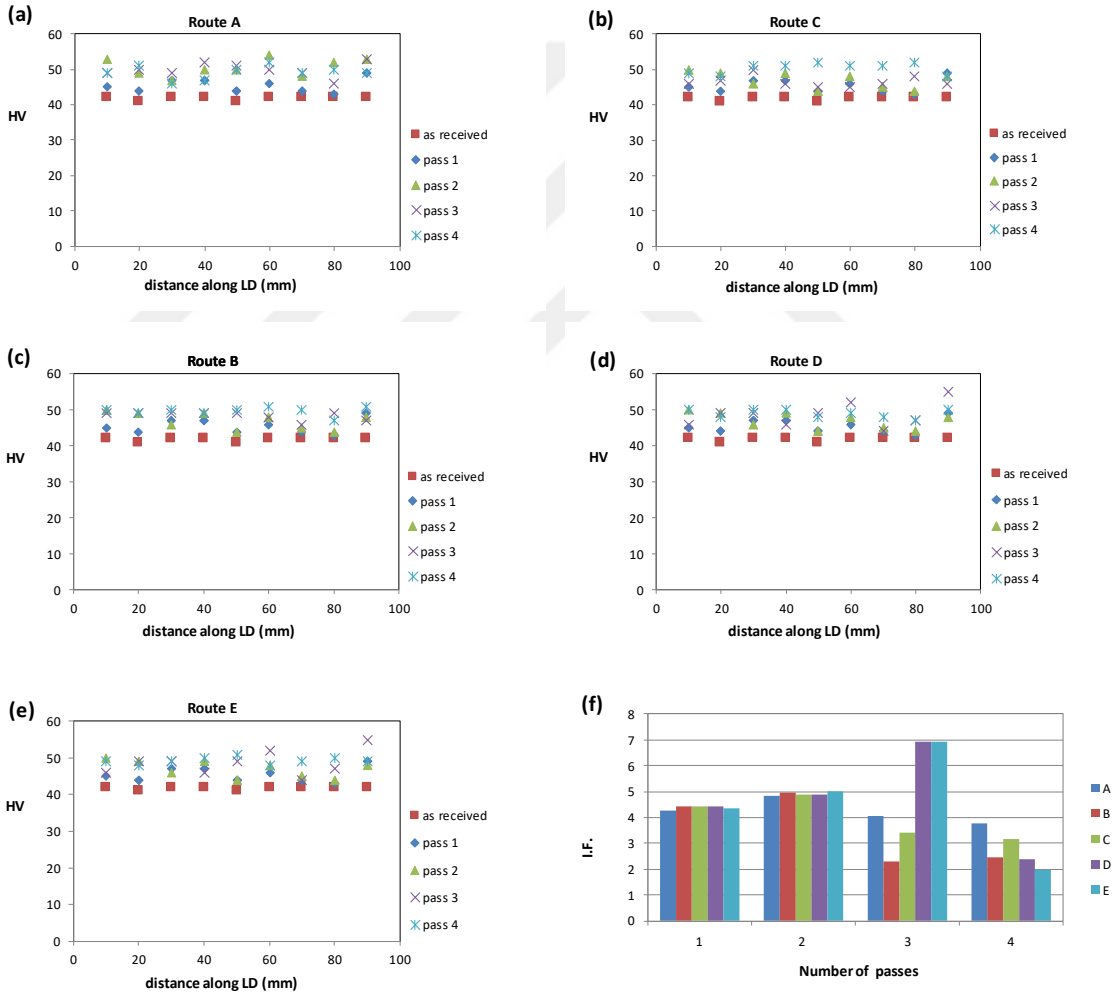

Figure 5.2.3: (a), (b), (c), (d) and (e) Hardness profiles of the CGPed pure zinc samples of all the routes along the longitudinal distances, (f) The inhomogeneity factor for all the routes versus pass numbers

Strength of the samples was also investigated through vickers hardness tests. The measurements was taken from the central line of the samples and inhomogeneity factors were calculated according to the equation explained in the previous sections [123, 124].

The highest hardness increase is achieved for the first pass with a rate of 9% over the as-received condition. The average hardness improvement was about 19% after the fourth passes (Figure 5.2.3.a-e).

As demonstrated in Figure 5.2.3(f), inhomogeneity factors for the first passes which are identical are almost the same. A similar data is measured for the second passes of the routes except A which is not rotated between passes. Inhomogeneity variation is small between routes B and D possessing different pass orders. As a result, pass order has a little impact on homogeneity of hardness in a particular direction. The maximum homogeneity difference after the whole process is between routes A and E. Sample transverse direction is parallel to the groove edges for all the passes for route A, whereas three of them are perpendicular to the groove edges for route E. This result is similar to that of stainless steel samples. The difference might stem from the different crystal structures, which have different slip systems, of these two materials. Strength and ductility profiles of the routes are summarized in Figure 5.2.4.

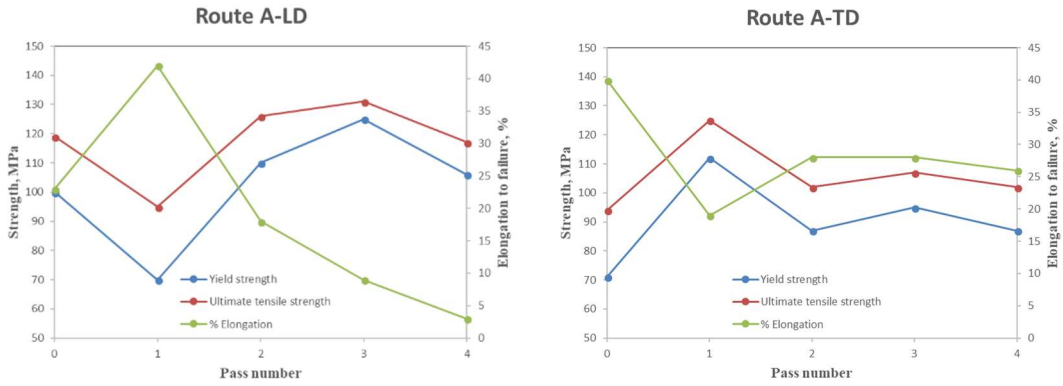

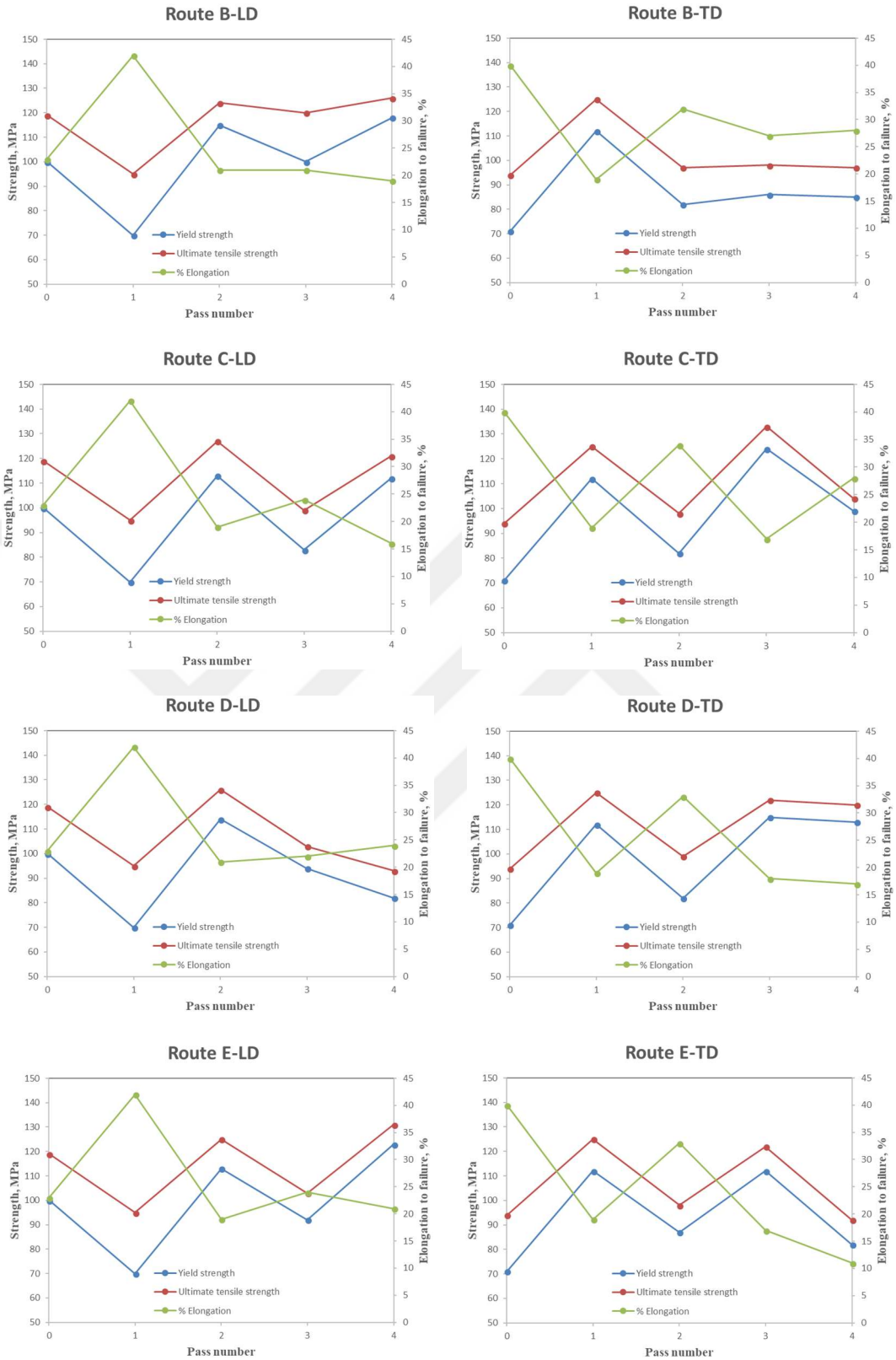

Figure 5.2.4: Strength and ductility profiles of commercially pure zinc samples with increasing passes

Erichsen test has been achieved to find out the formability of the material. One sample from the as-received material and another sample after the last pass of route E has been cut in the form of square. Force-cupping diagrams are as seen in Figure 5.2.5. Cupping distance of the sample has been diminished a few millimeters after CGP deformation. This means that the processed material shows lower formability.

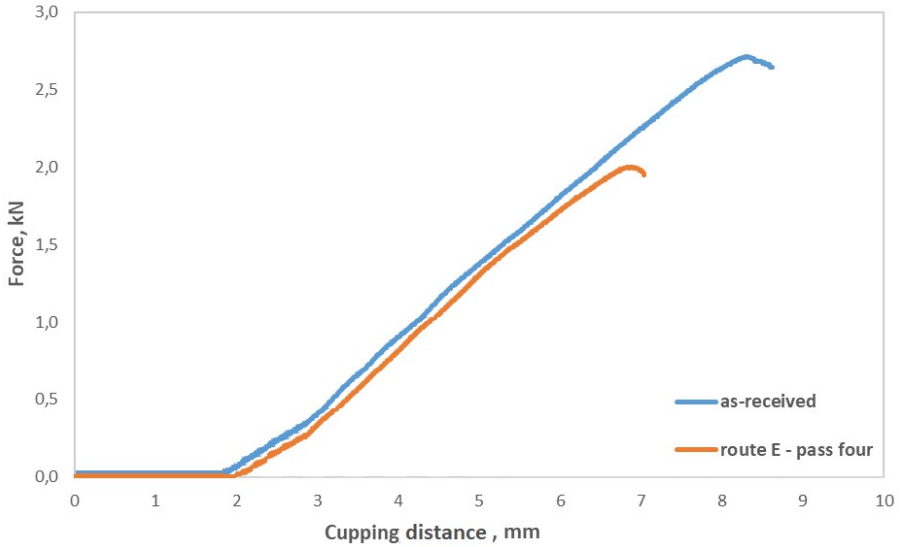

Figure 5.2.5: Force-cupping curves of commercially pure zinc samples: (a) as-received, (b) after fourth pass of route E

In Figure 5.2.6, the shape of the samples after erichsen test are shown. The one on the left belongs to the as-received sample while the one on the right is the final form of the sample after fourth pass of route E. Both the fracture of the as-received and CGPed samples are non-catastrophic since the non-uniform strain hardening region is relatively greater for this material.

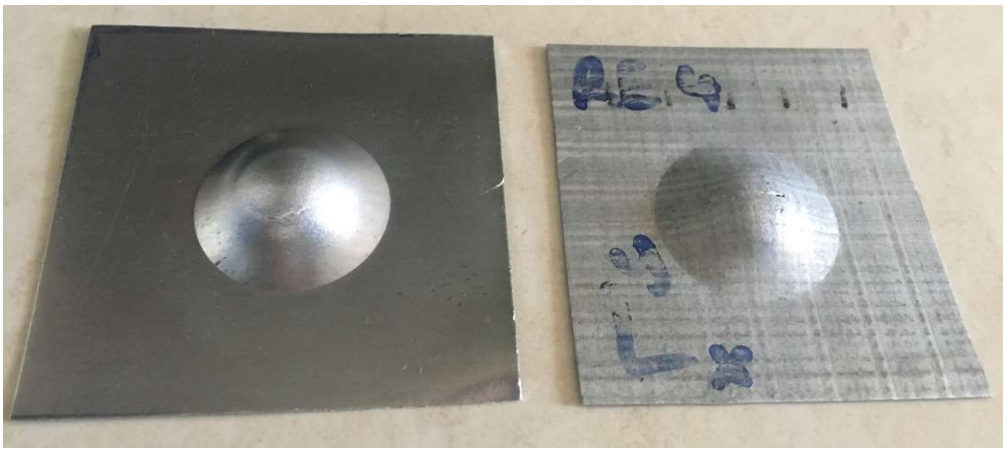

Figure 5.2.6: Samples formed after erichsen tests

Three tensile specimens from different regions of the CGPed zinc samples were tested to check the repeatability. The best conditions were chosen for the tests and the resulting curves are displayed in Figure 5.2.7. The only significant difference is fracture strain among all the repetability test data, which is acceptable because the fracture is in the non-uniform deformation region.

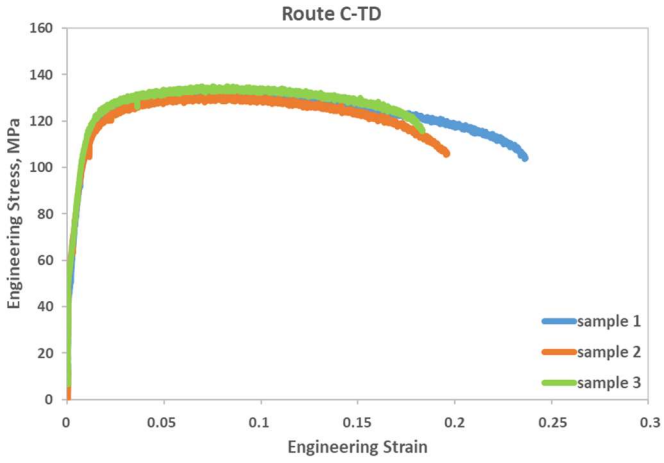

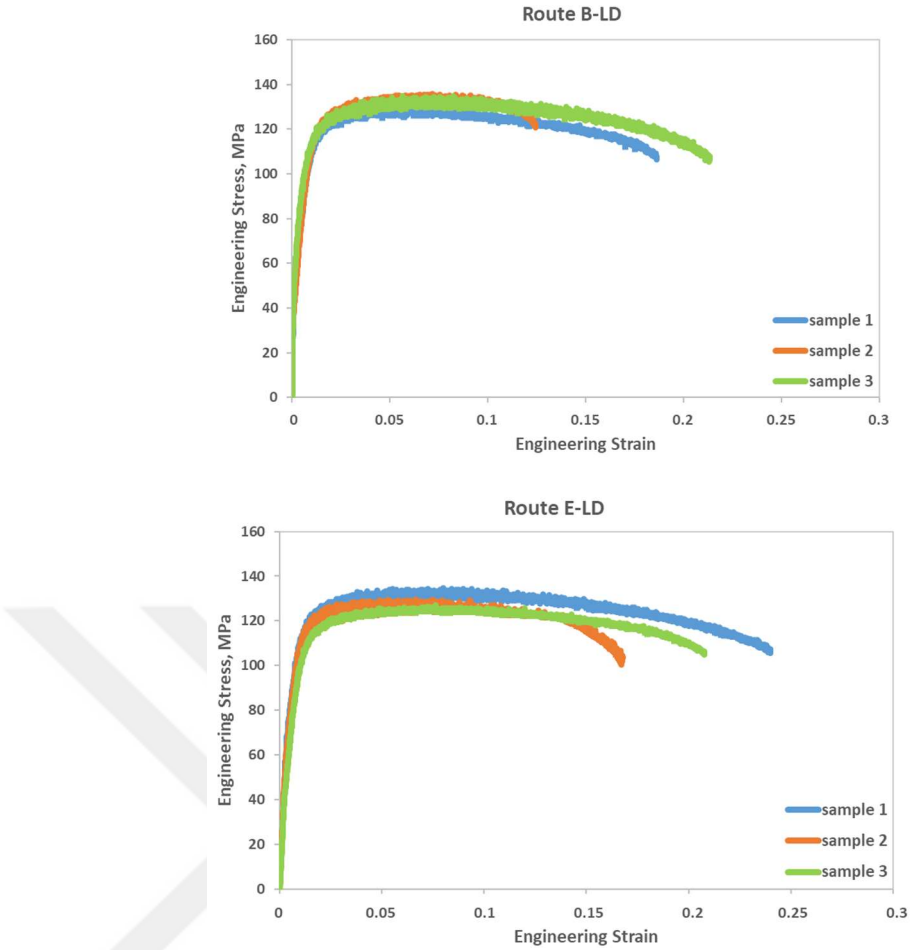

Figure 5.2.7: Repeatability test results of commercially pure zinc samples from (a) route B along TD, (b) route C along TD, (c) route E along LD

CHAPTER VI

CONCLUSIONS

Constrained Groove Pressing (CGP) routes has been demonstrated to be applicable for difficult-to-work alloys. Mechanical strengths are generally improved with some losses in ductility. The results along with the comparisons are presented below.

AISI 304

AISI 304 with FCC crystal structure was processed by five distinctly specified CGP routes at ambient temperature. The effects of routes on microstructure along with mechanical behavior revealed that:

1. The rate of grain refinement decreases with the increase in imposed strain during CGP of AISI 304. Strain path is not very effective in influencing the grain size and the rate of grain refinement is relatively low due to the simple deformation field in which slip is cancelled out by reverse slip during flat pressing.
2. Yield strength values increased more than two times for all routes, while ductility values decreased from around 60% to a range between 10% and 25%.
3. The best strength improvement is nearly 32% in LD belonging to route E compared to 41% occuring in TD for route C.
4. Strength anisotropy of route A with no rotations between passes is quite high, when compared to the other routes. Therefore, rotation between the passes reduces anisotropy because of a more uniform distribution of the bending and stretching regions, where CGP takes place and the highest propensity for micro-cracking is expected.

Ti-15V-3Cr-3Sn-3Al

CGP processing of Ti-15V-3Cr-3Sn-3Al, namely β-Ti, was performed at ambient temperature. The influences of CGP routes on microstructure and mechanical behavior were examined. The results are as following:

1. Grain refinement effectiveness of CGP on β-Ti is comparatively low and strain path is not very influential in influencing the grain size after processing.
2. Ultimate tensile strength of the samples is improved considerably after the initial pass, and almost stabilized for most of the conditions afterwards. Ductility values decreased a little while yield strength values fluctuated throughout the deformation process.
3. The highest strength improvement is about 16%, occurring in LD for route D and E while it is nearly 15% in TD belonging to route C and D. Moreover, strength anisotropy of routes are quite low for β-Ti.
4. As-received β-Ti shows a bump after yield point. This bump is eliminated while the yield strength of the as-received material decreases with the increasing dislocations during deformation.

Commercially Pure Zinc

CGP routes are successively applied to commercially pure zinc samples at ambient temperature. Some important effects on microstructure and mechanical behavior are analyzed and presented as follows:

1. The rate of grain refinement decelerates with the increase in imposed strain during deformation. Strain path is effective in dictating the grain size for pure zinc. The best grain refinement ratio is around 47% belonging to route A and the lowest refinement is observed for route B, which is approximately 37%.

2. After CGP, mechanical twinning activation has taken place. Twins are thinner for the routes A, C and D compared to the other routes after the final pass. They are also rather thick and few in number after the first pass. Moreover, intensity of twins is relatively low for route E.
3. Strength improvement is mostly improved for routes during the deformation processes. Yield strength values mostly increased for all routes, whereas ductility values mostly decreased. The best strength improvement is nearly 8%, and occurs in LD for route E compared to 28% in TD belonging to route D.
4. After the first CGP passes, a decrease in strength and an increase in ductility is observed along LD in an unexpected way. The reasons for this behavior can be considered as the mechanisms of micro-cracking and flow softening which is related to dislocation annihilation at higher dislocation densities through dynamic recovery mechanisms.
5. As-received material was rather anisotropic. In addition, mechanical behavior of the samples strained along two perpendicular directions on the same plane revealed the existence of flow anisotropy with varying degree depending on the route and pass number.
6. The twin size is limited by the size of the grains. Long twins are present for the initial passes, while relatively shorter twins are observed for the subsequent passes with the increasing rate of grain refinement.

Table 6.1: CGP comparison table of three materials

COMPARISON CHART			
Properties	Materials		
	AISI 304	Ti-15V-3Cr-3Sn-3Al	commercially pure zinc
1.The route with maximum grain refinement rate	RB 52,5 %	RE 16 %	RA 47 %
2. Strain Path Effect on grain size	low	low	high
3. Twinning activation	yes	no	yes
4. Macroscopic fracture	no	no	no
5. Max Strength Improvement (LD)	RE 32 %	RD 16 %	RE 8 %
6. Max Strength Improvement (TD)	RC 41 %	RC, RD 15 %	RD 28 %
7. Hall-Petch constant (k) (MPa.m^1/2)	4600	5068	764
8. Strength anisotropy	high	low	high
9. Max hardness improvement	RE 112 %	RE 20 %	RC 20 %
10. Min hardness inhomogeneity factor	RE - 2,5	RC - 3	RE - 2

BIBLIOGRAPHY

[1] Valiev RZ, Langdon TG, Principles of equal-channel angular pressing as a processing tool for grain refinement. Prog Mater Sci 2006;51:881-981

[2] Wei Q, Jiao T, Mathaudhu SN, Ma E, Hartwig KT, Ramesh KT. Microstructure and mechanical properties of tantalum after equal channel angular extrusion (ECAE). Mater Sci Eng A 2003;358:266-72

[3] Tham YW, Fu MW, Hng HH, Yong MS, Lim KB. Bulk nanostructured processing of aluminum alloy. J Mater Process Technol 2007;192:575-81

[4] Sanders PG, Eastman JA, Weertman JR. Pore distribution in nanocrystalline metals by small-angle neutron scattering. Acta Mater 1998;46:4195-4202

[5] Korznikov AV, Ivanisenko YV, Laptionok DV, Safarov IM, Pilyugin VP, Valiev RZ. Influence of severe plastic deformation on structure and phase composition of carbon steel. Nanostruct Mater 1994;4:159-67

[6] Cziraki A, Gerocs I, Toth-Kadar E, Bakonyi I. TEM and XRD study of the microstructure of nanocrystalline Ni and Cu prepared by severe plastic deformation and electrodeposition. Nanostruct Mater 1995;6:547-50

[7] Salishchev G, Zaripova R, Galeev R, Valiakhmetov O. Nanocrystalline structure formation during severe plastic deformation in metals and their deformation behavior. Nanostruct Mater 1995;6:913-6

[8] Hosseini E, Kazeminezhad M, Mani A, Rafizadeh E. On the evolution of flow stress during constrained groove pressing of pure copper sheet. Comput Mater Sci 2009;45:855-9

[9] Furukawa M, Horita Z, Nemoto M, Langdon TG. The use of severe plastic deformation for microstructural control. Mater Sci Eng A 2002;324:82-9

[10] Horita Z, Furukawa M, Nemoto M, Barnes AJ, Langdon TG. Superplastic forming at high strain rates after severe plastic deformation. Acta Mater 2000;48:3633-40

[11] Wang YM, Ma E. Strain hardening, strain rate sensitivity, and ductility of nanostructured metals. Mater Sci Eng A 2004;375:46-52

[12] Park K-T, Shin DH. Microstructural interpretation of negligible strain hardening behavior of submicrometer-grained low-carbon steel during tensile deformation. Metall Mater Trans A 2002;33:705-7

[13] Zhang Z, Zhou F, Lavernia EJ. On the analysis of grain size in bulk nanocrystalline materials via x-ray diffraction. Metall Mater Trans A 2003;34:1349-1355

[14] Wang Z, Liang P, Guan Y, Liu Y, Jiang L. Experimental investigation of pure aluminum sheets processed by constrained groove process. Indian Journal of Engineering & Materials Sciences 2014;21:121-127

[15] Sunil BR, Kumar AA, Kumar TSS, Chakkingal U. Role of biomineralization on the degradation of fine grained AZ31 magnesium alloy processed by groove pressing. Mater Sci Eng C 2013;33:1607-1615

[16] Zhilyaev AP, Langdon TG. Using high-pressure torsion for metal processing: fundamentals and applications. Prog Mater Sci 2008;53:893-979

[17] Valiev RZ. Nanostructuring of metals by severe plastic deformation for advanced properties. Nat Mater 2004;3:511-6

[18] Horita Z, Furukawa M, Nemoto M, Langdon TG. Development of fine grained structures using severe plastic deformation. Mater Sci Tech 2000;16(11-12):1239-1245

[19] Yapici GG, Karaman I, Luo ZP, Rack H. Microstructure and mechanical properties of severely deformed powder processed Ti-6Al-4V using equal channel angular extrusion. Scr Mater 2003;49:1021-1027

[20] Yapici GG, Karaman I, Luo ZP. Mechanical twinning and texture evolution in severely deformed Ti-6Al-4V at high temperatures. Acta Mater 2006;54:3755-3771

[21] Horita Z, Fujinami T, Nemoto M, Langdon TG. Equal-channel angular pressing of commercial aluminum alloys: grain refinement, thermal stability and tensile properties. Metall Mater Trans A 2000;31:691-701

[22] Oh SJ, Kang SB. Analysis of the billet deformation during equal channel angular pressing. Mater Sci Eng A 2003;343:107-15

[23] Zhu YT, Lowe TC. Observations and issues on mechanisms of grain refinement during ECAP process. Mater Sci Eng A 2000;291:46-53

[24] Zhilyaev AP, Nurislamova GV, Kim B-K, Baro MD, Szpunar JA, Langdon TG. Experimental parameters influencing grain refinement and microstructural evolution during high-pressure torsion. Acta Mater 2003;51:753-65

[25] Zhilyaev AP, Lee S, Nurislamova GV, Valiev RZ, Langdon TG. Microhardness and microstructural evolution in pure nickel during high-pressure torsion. Scr Mater 2001;44:2753-8

[26] Vorhauer A, Pippan R. On the homogeneity of deformation by high pressure torsion. Scr Mater 2004;51:921-5

[27] Sakai G, Horita Z, Langdon TG. Grain refinement and superplasticity in an aluminum alloy processed by high-pressure torsion. Mater Sci Eng A 2005;393:344-51

[28] Xu C, Horita Z, Langdon TG. The evolution of homogeneity in processing by high-pressure torsion. Acta Mater 2007;55:203-12

[29] Zhilyaev AP, Oh-Ishi K, Langdon TG, McNelley TR. Microstructural evolution in commercial purity aluminum during high-pressure torsion. Mater Sci Eng A 2005;410:277-80

[30] Kawasaki M, Alhajeri SN, Xu C, Langdon TG. The development of hardness homogeneity in pure aluminum and aluminum alloy disks processed by high-pressure torsion. Mater Sci Eng A 2011;529:345-51

[31] Nakamura K, Neishi K, Kaneko K, Nakagaki M, Horita Z. Development of severe torsion straining process for rapid continuous grain refinement. Mater Trans 2004;45:3338-42

[32] Miyahara Y, Emi N, Neishi K, Nakamura K, Kaneko K, Nakagaki M, et al. Microstructures and mechanical properties of Mg alloy after severe torsion straining process. Mater Sci Forum 2006;503:949-54 [Trans Tech Publ]

[33] Neishi K, Higashino A, Miyahara Y, Nakamura K, Kaneko K, Nakagaki M, et al. Grain refinement of commercial Al-Mg alloy using severe torsion straining process. Mater Sci Forum 2006;503:955-60 [Trans Tech Publ]

[34] Kawasaki Y, Neishi K, Miyahara Y, Nakamura K, Kaneko K, Nakagaki M, et al. Application of severe torsion straining process for grain refinement of steel. Mater Sci Forum 2006;503:943-8 [Trans Tech Publ]

[35] Sato YS, Kurihara Y, Park SHC, Kokawa H, Tsuji N. Friction stir welding of ultrafine grained Al alloy 1100 produced by accumulative roll-bonding. Scr Mater 2004;50:57-60

[36] Lee SH, Saito Y, Tsuji N, Utsonomiya H, Sakai T. Role of shear strain in ultragrain refinement by accumulative roll-bonding (ARB) process. Scr Mater 2002;46:281-5

[37] Park K-T, Kwon H-J, Kim W-J, Kim Y-S. Microstructural characteristics and thermal stability of ultrafine grained 6061 Al alloy fabricated by accumulative roll bonding process. Mater Sci Eng A 2001;316:145-52

[38] Lee SH, Saito Y, Sakai T, Utsonomiya H. Microstructures and mechanical properties of 6061 aluminum alloy processed by accumulative roll-bonding. Mater Sci Eng A 2002;325:228-35

[39] Kwan C,Wang Z, Kang S-B. Mechanical behavior and microstructural evolution upon annealing of the accumulative roll-bonding (ARB) processed Al alloy 1100. Mater Sci Eng A 2008;480:148-59

[40] Tsuji N, Saito Y, Lee S, Minamino Y. ARB (Accumulative Roll-Bonding) and other new techniques to produce bulk ultrafine grained materials. Adv Eng Mater 2003;5:338-44

[41] Balakrishna C, Teodora S, Nedkova, Raghavan Srinivasan. A comparison of the properties of SPD-processed AA-6061 by equal-channel angular pressing, multi-axial compressions/forgings and accumulative roll bonding. Mater Sci Eng A 2005;410-411:394-397

[42] Desrayaud C, Ringeval S, Girard S, Driver JH. A novel high straining process for bulk materials- The development of a multipass forging system by compression along three axes. J Mater Process Tech 2006; 172: 152

[43] Richert M, Stüwe HP, Zehetbauer MJ, Richert J, Pippan R, Motz C, Schafler E. Work hardening and microstructure of AlMg5 after severe plastic deformation by cyclic extrusion and compression. Mater Sci Eng A 2003;355(1-2):180

[44] Yeh JW, Yuan SY, Peng CH. Microstructures and tensile properties of an A1-12 wt pct Si alloy produced by reciprocating extrusion. Metall Mater Trans A 1999;30: 2503-2512

[45] Lu WL, Wang Y, Hai JT. The effects of sandglass extrusion on material microstructures and properties. Mater Sci Forum 2003;426-432:2831

[46] Richert M, Liu Q, Hansen N. Microstructural evolution over a large strain range in aluminium deformed by cyclic-extrusion-compression. Mater Sci Eng A 1999;260:275-83

[47] Huang JY, Zhu YT, Jiang H, Lowe TC. Microstructures and dislocation configurations in nanostructured Cu processed by repetitive corrugation and straightening. Acta Mater 2001;49:1497-505

[48] Huang J, Zhu YT, Alexander DJ, Liao X, Lowe TC, Asaro RJ. Development of repetitive corrugation and straightening. Mater Sci Eng A 2004;371:35-9

[49] Zhu YT, Lowe TC, Jiang H, Huang J. Method for producing ultrafine-grained materials using repetitive corrugation and straightening; 2001.

[50] Pandey SC, Joseph MA, Pradeep MS, Raghavendra K, Ranganath VR, Venkateswarlu K. A theoretical and experimental evaluation of repetitive corrugation and straightening: application to Al-Cu and Al-Cu-Sc alloys. Mater Sci Eng A 2012;534:282-7.

[51] Beygelzimer Y, Varyukhin V, Synkov S, Orlov D. Useful properties of twist extrusion. Mater Sci Eng A 2009;503:14-7.

[52] Orlov D, Beygelzimer Y, Synkov S, Varyukhin V, Horita Z. Evolution of microstructure and hardness in pure Al by twist extrusion. Mater Sci Forum 2008;49:2-6.

[53] Berta M, Orlov D, Prangnell PB. Grain refinement response during twist extrusion of an Al-0.13% Mg alloy. Int J Mater Res 2007;98(3):200.

[54] Lee J, Park J. Numerical and experimental investigations of constrained groove pressing and rolling for grain refinement. J Mater Process Technol 2002;130-131:208-13.

[55] Shin DH, Park JJ, Kim YS, Park KT. Constrained groove pressing and its application to grain refinement of aluminum. Mater Sci Eng A 2002;328:98-103.

[56] Gupta AK, Maddukuri TS, Singh SK. Constrained groove pressing for sheet metal processing. Prog Mater Sci 2016;84:403-462

[57] Niranjan GG, Chakkingal U. Deep drawability of commercial purity aluminum sheets processed by groove pressing. J Mater Process Technol 2010;210:1511-6

[58] Shirdel A, Khajeh A, Moshksar MM. Experimental and finite element investigation of semi-constrained groove pressing process. Mater Des 2010;31:946-50

[59] Wang Z-S, Guan Y-J, Wang G-C, Zhong C-K. Influences of die structure on constrained groove pressing of commercially pure Ni sheets. J Mater Process Technol 2015;215:205-218

[60] Peng K, Zhang Y, Shaw LL, Qian K-W. Microstructure dependence of a Cu-38Zn alloy on processing conditions of constrained groove pressing. Acta Mater 2009;57:5543-5553

[61] Khodabakhshi F, Abbaszadeh M, Eskandari H, Mohebpour SR. Application of CGP-cross route process for microstructure refinement and mechanical properties improvement in steel sheets. J Manuf Process 2013;15:533-541

[62] Havner KS. Plastic deformation of crystalline solids. Cambridge Univ Press 1992:67-84

[63] Hosford WF. The mechanics of crystals and textured polycrystals. Oxford Univ Press 1993:29-50

[64] www.corrosionpedia.com

[65] Yapici GG. Severe plastic deformation of difficult-to-work alloys. Texas A&M Univ 2004:10-21

[66] www.eng.famu.fsu.edu

[67] Reid CN. Deformation geometry for materials scientists. Pergamon Press 1973:103-126

[68] Courtney TH. Mechanical behavior of materials. McGraw-Hill 2000:141-159

[69] J.W. Christian, S. Mahajan. Deformation twinning. Prog Mater Sci 1995;39

[70] Reed-Hill RE, Abbaschian R. Physical metallurgy principles. PWS Publishing Company 1991:541-546

[71] Cahn RW. Plastic deformation of alpha-uranium; twinning and slip. Acta Metal 1953;1:49-52

[72] Gray III GT. Deformation twinning in Al-4.8 wt% Mg. Acta Metal 1988;36:1745-1754

[73] Park J-J, Park N-J. Influence of orthogonal shear on texture and R value in aluminum sheet. J Mater Process Technol 2005;169:299-307

[74] Singh AK, Schwarzer RA. Development of cold rolling texture in the binary Ti-0.4 Mn alloy. Met Mater Process 2006;18:351

[75] Singh AK, Schwarzer RA. Evolution of texture during thermomechanical processing of titanium and its alloys. Trans Ind Inst Met 2008;61:371-87.

[76] Tucker GEG. Texture and earing in deep drawing of aluminium. Acta Metall 1961;9:275-286

[77] Lankford WT, Snyder SC, Bausher JA. New criteria for predicting the press performance of deep drawing sheets. Trans. ASM 42 1950:1197-1205

[78] Saito Y, Utsonomiya H, Suzuki H, Sakai T. Improvement in the r-value of aluminum strip by a continuous shear deformation process. Scripta Mater 2000;42:1139-1144

[79] Sakai T, Hamada S, Saito Y. Improvement of the r-value in 5052 aluminum alloy sheets having through-thickness shear texture by 2-pass single-roll drive unidirectional shear rolling. Scripta Mater 2001;44:2569-2573

[80] Lee JC, Seok HK, Han JH, Chung YH. Controlling the textures of the metal strips via the continuous confined strip shearing (C2S2) process. Mater Res Bull 2001;36:997-1004

[81] Utsunomia H, Ueno T, Sakai T. Improvement in the r-value of aluminum sheets by differential-friction rolling. Scripta Mater 2007;57:1109-1112

[82] Lee JK, Lee DN. Texture control and grain refinement of AA1050 Al alloy sheets by asymmetric rolling. Int J Mech Sci 2008;50:869-887

[83] Han JH, Suh JY, Jee KK, Lee JC. Evaluation of formability and planar anisotropy based on textures in aluminum alloys processed by a shear deformation process. Mater Sci Eng A 2008;447:107-120

[84] Milad M, Zreiba N, Elhalouani F, Baradai C. The effect of cold work on structure and properties of AISI 304 stainless steel. J Mater Process Technol 2008;203:80-85

[85] Kahatak HS, Raj B. Corrosion of Austenitic Stainless Steels. Narosa Publishing House, Delhi 2002:2

[86] Beddoes J, Parr JG. Introduction to Stainless Steels. ASM International, Materials Park, Ohio 1999:122

[87] Marshall P.Austenitic Stainless Steels: Microstructure and Mechanical Properties. Elsevier Applied Science, London 1984:19

[88] Tavares SSM, Gunderov D, Stolyarov V, Neto JM. Phase transformation induced by severe plastic deformation in the AISI 304L stainless steel. Mater Sci Eng A 2003;358:32-36

[89] Etienne A, Radiguet B, Genevois C, Le Breton J-M, Valiev R, Pareige P. Thermal stability of ultra-fine grained austenitic stainless steels. Mater Sci Eng A 2010;527:5805-5810

[90] Qu S, Huang CX, Gao YL, Yang G, Wu SD, Zang QS, Zhang ZF. Tensile and compressive properties of AISI 304L stainless steel subjected to equal channel angular pressing. Mater Sci Eng A 2008; 475:207-216

[91] Krishnaiah A, Chakkingal U, Venugopal P. Applicability of the groove pressing technique for grain refinement in commercial purity copper. Mater Sci Eng A 2005;410-411:337-340

[92] Morattab S, Ranjbar K, Reihanian M. On the mechanical properties and microstructure of commercially pure Al fabricated by semi-constrained groove pressing. Mater Sci Eng A 2011;528:6912-6918

[93] Kumar SSS, Raghu T. Mechanical behaviour and microstructural evolution of constrained groove pressed nickel sheets. J Mater Process Technol 2013;213:214-220

[94] Kawasaki M, Langdon TG. The significance of strain reversals during processing by high-pressure torsion. Mater Sci Eng A 2008;498:341-348

[95] Orlov D, Todaka Y, Umemoto M, Tsuji N. Role of strain reversal in grain refinement by severe plastic deformation. Mater Sci Eng A 2009;499:427-433

[96] Reihanian M, Ebrahimi R, Tsuji N, Moshksar MM. Analysis of the mechanical properties and deformation behavior of nanostructured commercially pure Al processed by equal channel angular pressing (ECAP). Mater Sci Eng A 2008;473:189-194

[97] Dieter GE, Bacon DJ. Mechanical Metallurgy. McGraw-Hill, New York 1986

[98] Kumar SSS, Raghu T. Tensile behaviour and strain hardening characteristics of constrained groove pressed nickel sheets. Mater & Design 2011;32:4650-4657

[99] Valiev RZ, Islamgaliev RK, Alexandrov IV. Bulk nanostructured materials from severe plastic deformation. Prog in Mater Sci 2000;45:103-189

[100] Akhmadeev NA, Kobelev NP, Mulyukov RR, Soifer YM, Valiev RZ. The effect of heat treatment on the elastic and dissipative properties of copper with the submicrocrystalline structure. Acta Metall et Mater 1993;41:1041-1046

[101] Duncan RM, Minion CDT. The role of depth hardenability in the selection of high strength alloys for aircraft applications. The Sci Tech & Appl of Ti 1970:945-957

[102] Wood RA, Ogden HR. The all-beta titanium alloy (Ti-13V-2Cr-3Al). Battelle Memorial Institute 1959

[103] Wood RA. Beta titanium alloys. MCIC, Battelle Colombus Laboratories, Colombus 1972

[104] Boyer RR, Rosenberg HW. Beta titanium alloys in the 1980's. TMS-AIME Publications, Warrendale, PA 1984.

[105] Froes FH, Bomberger HB. The beta titanium alloys. Phys Metall Mater Overview 1985;37:28-37

[106] www.azom.com

[107] Khodabakhshi F, Kazeminezhad M. The effect of constrained groove pressing on grain size, dislocation density and electrical resistivity of low carbon steel. Mater Des 2011;32:3280-3286

[108] Kalpakjian, S., Schmid, S.R., 2008. Manufacturing processes for engineering materials. 5. Edition in SI units. Pearson: Prentice Hall.

[109] Fong KS, Tan MJ, Chua BW, Atsushi D. Enabling wider use of magnesium alloys for lightweight applications by improving the formability by groove pressing. Procedia 2015;26:449-454

[110] Sajadi A, Ebrahimi M, Djavanroodi F. Experimental and numerical investigation of Al properties fabricated by CGP process. Mater Sci Eng A 2012; 552:97-103

[111] Peng K, Su L, Shaw LL, Qian K-W. Grain refinement and crack prevention in constrained groove pressing of two-phase Cu-Zn alloys. Scripta Mater 2007; 56: 987-990

[112] Chandler H. Hardness Testing, ASM International, Materials Park, Ohio 1999:66

[113] Huang Y, Prangnell PB. The effect of cryogenic temperature and change in deformation mode on the limiting grain size in a severely deformed dilute aluminium alloy. Acta Mater 2008; 56:1619-1632

[114] Hebesberger T, Stüwe HP, Vorhauer A, Wetscher F, Pippan R. Structure of Cu deformed by high pressure torsion. Acta Mater 2005; 53:393-402

[115] Jazaeri H, Humphreys FJ. The transition from discontinuous to continuous recrystallization in some aluminium alloys: I- the deformed state. Acta Mater 2004; 52:3239-3250

[116] Bowen JR, Prangnell PB, Humphreys FJ. Microstructural evolution during formation of ultrafine grain structures by severe deformation. Mater Sci Technol 2000; 16:1246-1250

[117] Mintz B. Importance of k_y (Hall-Petch slope) in determining strength of steels. Metals Technol 1984; 11:265-272

[118] Bergstrom Y, Hallen H. Hall-Petch relationships of iron and steel. Metal Sci 1983; 17:341-347

[119] Karavaeva MV, Abramova MM, Enikeev NA, Raab GI, Valiev RZ. Superior strength of austenitic steel produced by combined processing, including equal-channel angular pressing and rolling. Metals 2016; 6:310

[120] Huang CX, Yang G, Gao YL, Wu SD, Zhang ZF. Influence of processing temperature on the microstructures and tensile properties of 304L stainless steel by ECAP. Mater Sci Eng A 2008; 485:643-650

[121] Yapici GG, Karaman I, Maier HJ. Mechanical flow anisotropy in severely deformed pure titanium. Mater Sci Eng A 2006; 434:294-302

[122] Hosseini E, Kazeminezhad M. Nanostructure and mechanical properties of 0-7 strained aluminum by CGP: XRD, TEM and tensile test. Mater Sci and Eng A 2009; 526:219-224

[123] Borhani M, Djavanroodi F. Rubber pad-constrained groove pressing process: Experimental and Finite element investigation. Mater Sci Eng A 2012; 546:1-7

[124] Khodabakhshi F, Kazeminezhad M, Kokabi AH. Constrained Groove pressing of low carbon steel: Nano-structure and mechanical peoperties. Mater Sci Eng A 2010; 527:4043-4049

[125] Fischer A, Richter H, Shalynin A, Krottenthaler P, Obermeier G, Lambert U, Wahlich R. Upper yield point of large diameter silicon. Microelectronic Eng 2001; 56:117-122

[126] Wu H, Jiang J, Liu H, Sun J, Gu Y, Tang R, Zhao X, Ma A. Fabrication of an ultra-fine grained pure titanium with high strength and good ductility via ECAP plus cold rolling. Metals 2017; 7(12):563

VITA

Zeynel Güler was born in Istanbul, Turkey in 1989. After he attended Kabataş High School, he continued his education in Boğaziçi University, Istanbul. In 2012, he received a B.S. degree from the department of Mechanical Engineering. After graduation, he worked as a design and quality engineer in several jobs like designing and analyzing of elevator and conveyors, quality processes of household appliances etc. He also worked at Vestel Company which has the greatest factory in Europe. After all these experiences, he has turned back to academia as an M.S. student in mechanical engineering in 2015. He has been conducting research on Materials science and engineering as a research assistant since then. Mr. Güler has been admitted to the University of New Mexico in the department of Mechanical Engineering as a Ph.D. student for the Fall 2018 semester.